QUANTUM PHOTONICS IN WAVEGUIDE-INTEGRATED ARCHITECTURES

A Dissertation

by

DEBSUVRA MUKHOPADHYAY

Submitted to the Graduate and Professional School of
Texas A&M University
in partial fulfillment of the requirements for the degree of

DOCTOR OF PHILOSOPHY

Chair of Committee,	Girish S. Agarwal
Committee Members,	M. Suhail Zubairy
	Aleksei M. Zheltikov
	Philip Hemmer
Head of Department,	Grigory Rogachev

August 2022

Major Subject: Physics

ABSTRACT

The prospect of incorporating strong light-matter interaction into the greater cause of optical information processing has become one of the ultimate goals of quantum optics. Currently, one of the most useful resources for the design of quantum photonic devices is waveguide-integrated optics [1]. The most lucrative feature of waveguide-based interfaces is the remarkable controllability over photonic transport properties, a feature that can be conveniently harnessed for the design of purely optical devices. However, this is not the sole aspect that makes these systems so special. Quantum emitters interfacing with a waveguide offers the perfect platform to study the effects of *vacuum-mediated* long-range couplings between *distant* emitters. The tunability of the nature and strength of waveguide-induced couplings is providing useful insights into the wider scope and applicability of these models. This thesis attempts to bring these two different approaches to the theoretical investigation of waveguide-integrated architectures under a common theme, highlighting some of the intriguing outcomes of these treatments deduced in the recent past.

The first half of the thesis is dedicated to the theoretical study of single-photon transport in a waveguide interfacing with a periodic string of atomic-scale dipoles, like qubits or two-level atoms. Radiation fields in a one-dimensional structured environment can strongly modify the spontaneous emission from these dipoles. The ensemble of dipoles can exhibit a variety of interference phenomena, which lends greater control to these setups on photon transport. For identical atoms, these interference effects are systematically studied and connections to the lattice periodicity are established. Other notable features include flat-banded reflection profiles owing to the periodicity and cooperative Dicke-type superradiance. Certain non-Markovian signatures are also studied numerically, as they would be relevant in very-strong-coupling regimes. Going beyond the assumption of identical atoms, we next solve photon transport across an array of non-identical dipoles differing in their transition frequencies. By tailoring our analysis in a setting where the periodicity is an integer or half-integer multiple of the resonant wavelength, we work out the exact condition to generate

transparency by modulating the individual transition frequencies. We demonstrate the specific applicability of this scheme to an even-sized atomic chain. Since there is no control field used, this mechanism is clearly distinct from the standard paradigm of EIT. We also establish analogies with the linear excitation regime of cavity QED, where an identical manipulation of the atomic frequencies can render the system transparent to a weak input field. However, photon transport in a waveguide has one major distinction from cavity-QED setups. Waveguide-integrated devices display diode-like characteristics owing to the non-reciprocity of photon transport. This additional perk in a waveguide setup is a direct consequence of *phase couplings* between quantum emitters mediated by the waveguide, which widens the space of possibilities, offering clear advantages over cavities in various applications. All our theoretical results are deduced in the single-photon regime of waveguide QED, which requires a dedicated quantum mechanical treatment. With the advent of high-quality single-photon quantum sources, whether in the optical or the microwave regime, as well as the possibility of producing enhanced light-matter couplings in superconducting circuitry and quantum-dot-based structures, the laboratory verification of our analytical observations, should be within reach.

The second half of this thesis addresses some acute ramifications of a reservoir-mediated coupling between physical systems. Even in the absence of a driving field, the vacuum modes in a waveguide can introduce coupling and coherence between any two *otherwise non-interacting* systems exchanging energy with the waveguide. The coupling is commonly referred to as *dissipative coupling* as it originates from leakage into a common bath and requires an open-system description. The mean-field dynamics of dissipatively coupled systems can be modeled in terms of an effective *non-Hermitian Hamiltonian*, which can be tailored to exhibit *anti-Parity-Time (PT) symmetry*. This symmetry characterizes a Hamiltonian that flips signs upon the joint action of parity and time-reversal operators and has attracted enormous attention in the last decade. By tapping into the remarkable potential of anti-PT symmetry, we propose two intriguing applications. First, we demonstrate how this can serve as a *sensor* for *weak anharmonicities*. Nonlinearities are of fundamental interest in optics, leading to a myriad of important physical effects, such as

multistability/switching, generation of squeezed and entangled states, electromagnetically induced transparency, and so on. A fine-grained estimation of nonlinearities is, therefore, a prerequisite to the primed control of these effects. We present explicit results in the context of cavity magnonics, illustrating the efficient detection of magnonic anharmonicity ($\sim 0.01 - 10$ nHz) even at a very weak drive power of 1 μW. Since the theoretical analysis guiding our results is absolutely general, the sensing protocol can be applied to a broad class of systems. That said, the prime reason for choosing a magnon-based model is the continued escalation of interest in hybrid magnon-photon interfaces. New interest has also shown up in utilizing these interfaces for the reversible conversion between microwave and optical photons. This pursuit is still in its infancy and achieving appreciable conversion efficiency is still a far cry. We took a significant step in this direction when we proposed the idea of a *dissipatively coupled, anti-PT symmetric* cavity-magnon interface supporting large enhancements in the theoretical efficiency. The enhancement is made possible on account of a dark mode in the system. While the conversion in our model is reversible, the efficiencies in the microwave-to-optical and the optical-to-microwave conversions are found to be unequal. This asymmetry is unique to dissipatively coupled systems and emerges both from the indirect nature of the coupling as also the spatial separation between the cavity and magnetic sample. In light of the recent experimental realizations of dissipative magnon-photon couplings, both the applications proposed above are likely to secure practical implementation in the foreseeable future.

DEDICATION

To my parents.

ACKNOWLEDGEMENTS

This dissertation is a testament to the culmination of an exciting PhD career, riddled with numerous challenges that have helped me grow as a researcher and a person. The wealth of experience gathered through this sojourn simply cannot be summed up in words. Long after I have passed this phase, I could be possibly reminiscing on the true worth of the last five years, having spent my time among some of the best physicists in one of the best institutes of quantum optics. It is then, I suspect, that I would be getting a better perspective of this milestone, a greater sense of satisfaction at having traversed this far.

Let me begin by thanking all the members on my Ph.D. committee, Prof. Girish Agarwal, Prof. M. Suhail Zubairy, Prof. Aleksei M. Zheltikov, and Prof. Phil Hemmer for their useful comments, questions, and advice during my preliminary examination, and their generosity in serving on my committee. I would also like to express my gratitude to the Institute for Quantum Science and Engineering and the Department of Physics and Astronomy, Texas A&M University, for providing such a great atmosphere for physics education and research. The staff at the Physics department has been extremely prompt with any assistance regarding official requirements, including paperwork and technical issues. I remain indebted to them for their services, and especially to Raechel E. Superville and Sherree Kessler for their constant support as the departmental academic advisors.

One of the necessary precursors of intellectual growth is learning to be an independent thinker. This is especially important for a doctoral researcher at the initial stages of their career when they are making the transition from simply learning a subject to conceiving new ideas and applying them to solve new problems. In this regard, I must consider myself lucky to have been supervised by Prof. Girish Agarwal. His supreme command on the whole arena of quantum optics, while at times daunting, has been very inspiring. Gaining access to a tiny speckle of his mind and being guided by his percipient insights has given me a feel of some of the best qualities that define a successful physicist. His seamless devotion into thoughtfully shaping a research project and

arranging the obtained results to the best possible effect has been a wonderful lesson for me as a graduate researcher. Working with him has also taught me some of the crucial psychological aspects of handling research. I am truly obliged to him for having led me out of all my "crisis periods" when my initial ideas had hit dead ends. His admirable ability to forge connections between seemingly disparate or unrelated notions has motivated me to push my boundaries and become a fast learner. When one enters his office, it can be hard to miss a rather well-known quote glued to his office shelf: "If I have seen further, it is by standing on the shoulders of giants." I know, for a fact, that this is an adage I would like to live by. Learning to implement all the key lessons I gathered under his tutelage would be a natural step in that direction. For three consecutive years in my Ph.D. program, I was financially supported by the HEEP fellowship, which was instrumental in expediting my research progress. Prof. Agarwal had constantly thrown his weight behind my eligibility for this fellowship, and I cannot be thankful enough for this support. Finally, I would like to express my gratitude to him for his unyielding commitment in overseeing the drafting of my dissertation. His regular comments and suggestions have remedied many of the initial gaps in the formulation of this thesis.

I am privileged to have had some exceptional teachers both in my undergraduate and Master's programs back in India as well as during my Ph.D. program at Texas A&M University. I believe all of them played a significant role in advancing my understanding of physics. But I would like to reserve special mention for two of these teachers whose courses placed me in a much better position to tackle quantum optics research. Firstly, I would like to thank Prof. M. Sanjay Kumar who first introduced me to the field of quantum optics. I still fondly reminisce about his course on nonlinear and quantum optics during my Master's, which served as the perfect primer for my research. Discussions with him were always a delight. The second teacher I wished to mention is Prof. M. Suhail Zubairy. His illuminating course on quantum optics, replete with theoretical rigor and conceptual insights, was the most enjoyable course I have taken in my Ph.D program. I have thoroughly enjoyed working on the homework problems, some of which were quite laborious but extremely rewarding. The range and the depth of topics covered in the course

are commendably vast. But the way this course is designed makes it especially attractive and easy to learn from. There were also some non-academic aspects to the lectures which lightened up the mood. I remember some of the fun tidbits and personal anecdotes that were shared in the class, all of which contributed to making this course a memorable experience. I thank Prof. Zubairy sincerely for this opportunity.

A key portion of my PhD career, particularly over the last two years, has involved collaborations with my peers, Jayakrishnan M. P. Nair and Jiaxuan Wang, both of whom are fellow graduate students working under Prof. Agarwal. I am thoroughly grateful to both of them for the collaborative opportunities. Particularly, I thank Jayakrishnan for always being there to discuss any ideas, however crudely formulated. We have also given lectures to each other on several occasions, and I have gained a lot from these exchanges.

Last but not the least, I would like to thank my family and my closest friends for their immense support and understanding. It has been anything but easy to work on this Ph.D. cloistered in a far-flung western country a long distance away from my family. The tug of war between pining to visit family and focusing on the completion of the Ph.D. program, particularly in the midst of the Covid-19 pandemic, has been an agonizing mental struggle. Thankfully, the atmosphere at Texas A&M University has been quite congenial, and I was fortunate to come across some wonderful people who made this journey a tad more bearable.

CONTRIBUTORS AND FUNDING SOURCES

Contributors

This work was supported by a dissertation committee consisting of Prof. Girish S. Agarwal (advisor and chair), Prof. M. Suhail Zubairy, and Prof. Aleksei Zheltikov of the Department of Physics and Astronomy, and Prof. Philip Hemmer of the Department of Electrical & Computer Engineering.

Chapters 2-4 in this dissertation are based primarily on independent research undertakings under the supervision of Prof. Agarwal. The analyses and the results presented in Chapters 5-7 are based largely on collaborative research conducted with a student confrère. Contribution of this colleague has been duly acknowledged as a footnote at the beginning of each chapter.

Funding Sources

The graduate program and the research activities carried out from Fall 2018 through the summer of 2021 was financially sponsored by the Herman F. Heep and Minnie Belle Heep Texas A&M University endowed fund. The graduate program outside this timeframe, was supported in part by the Department of Physics and Astronomy, Texas A&M University, through Teaching Assistantship, and in part by the advisor's research grant, through Research Assistantship.

ACRONYMS

1D	One-Dimension(al)
QD	Quantum Dot
PT	Parity-Time
2LA	Two-level atom
VIC	Vacuum Induced Coherence
EP	Exceptional Point

TABLE OF CONTENTS

Page

LIST OF FIGURES

FIGURE Page

LIST OF TABLES

TABLE Page

1. INTRODUCTION

Photon-photon scattering is extremely weak in free space, as the individual photons do not interact with each other. This makes photons exemplary, low-noise carriers of information, both classical and quantum, preserving coherence over long distances. The longevity of their coherence sets them apart from material systems that suffer from appreciable decoherence on account of interactions with their environment. Equally central to the task of efficient information processing is that of information storage, which requires the controlled, reversible mapping of photonic quantum states onto long-lived states of matter, otherwise known as dark states. It is, therefore, imperative to devise robust atom-photon interfaces which endow long-time memory capabilities in optical information networks. The advent of modern nanotechnology has enabled the realization of strong coupling between atoms and photons, which is the cornerstone of quantum optics, lending a wide arsenal of resources for chip-scale all-optical devices and for quantum optical metrology. There has been remarkable progress in cavity quantum electrodynamics (QED) on the expedient engineering of strong and ultrastrong atom-photon couplings as well as photon-photon correlations, which has found very useful applications in superconducting circuitry, for instance. In a high-finesse electromagnetic resonator, strong optical confinement along the transverse dimension allows a single photon to effectively interact multiple times with atoms placed inside the cavity. This can generate strongly enhanced atom-photon coupling in cavities [2, 3]. This explains why quantum optics was, for a long time, concerned primarily with either atoms in free space or atoms interacting with single electromagnetic modes in cavities.

More recently, as a complementary paradigm to cavity QED, waveguide QED has started gaining significant traction in the study and regulation of light-matter interaction, with prospective applications in optical information processing. As opposed to cavity-based architectures, the atoms interact with a continuum of propagating photonic modes, but the confinement to 1D instead of 3D is enough to still achieve a strong coupling. A good quantifier for the coupling strength in these systems is the extinction of a propagating photon by a single emitter coupled to the waveg-

uide. As light scatters off an emitter, it gets attenuated in its original direction of propagation. The attenuation is perfectly encapsulated in the form of the *extinction coefficient* which is defined as $(1 - T)$, where T is the transmission coefficient. Superconducting flux qubits integrated with 1D microwave transmission lines have already achieved more than 99% extinction (see, for instance [4]). Among solid-state candidates, equally promising as efficient quantum emitters are epitaxy-grown QDs. Semiconductor QDs coupled to line defects in photonic crystal waveguides provide another platform to effect really strong atom-photon leading to high extinction coefficients [5]. While the former operates in the microwave regime, the latter employs optical photons. Both these systems describe realizations of a waveguide-QED model. The near-unity extinction coefficients in these configurations is to be contrasted with the very weak extinction by a single emitter experimentally realized in 3D open space, with the coefficient typically lying between $7 - 12\%$ (see Ref. [6] as an example). The major impediment to achieving high extinction is the inadequate overlap between the spatial modes of incident and scattered waves. The multitude of emission directions for an atom in 3D space substantially dampens the interference effect. In waveguide structures, emission can be tightly confined into the guided channel, allowing only two directions of scattering. However, compared to the prodigious success rate of artificial atoms like superconducting qubits and QDs, other waveguide-integrated quantum emitters like cold atoms in an optical lattice, color centers in diamond and solids like SiC, rare-earth defects in glasses and crystals still have a lot of catching up to do.

Experimental interest in waveguide-QED picked up speed when nanofiber-controlled fluorescence from an evanescently coupled Cesium atom was first demonstrated by Kien et al [7]. Ever since then, there has been a concerted endeavor by the photonics community to design cavity-free one-dimensional (1D) systems with no optical confinement along the propagation direction. Ref. [8] provides a comprehensive review on this subject. Photon scattering from a 1D continuum coupled to atomic scatterers has been widely investigated from various perspectives [9–38]. The radiative behavior of multi-emitter configurations is governed by the relative location of the emitters, allowing more efficient control on photon transport and possible adoption as a prototyp-

ical element for quantum information. As quantum emitters, artifical atoms like superconducting qubits and quantum dots have largely led the way in the engineering of strongly integrated atom-waveguide architectures, due to their near-perfect coherence properties. An ensemble of emitters interfacing with a waveguide exhibits a myriad of exotic phenomena such as single-photon super- and sub-radiance [39], nonreciprocal photon transport [40], and asymmetrical Fano lineshapes [39]. Such models serve as the simplest possible theoretical platform to analyse, predict, and leverage the cooperative effects of multiple quantum emitters arranged in a lattice configuration. When the lattice periodicity equals an integer multiple of the wavelength, the cooperative emission from the atomic array retains its Lorentzian profile with a linearly scaling decay rate, as has been demonstrated in [39, 41]. By stimulating interaction between photons, a multi-spin cluster can serve as an optical switch or nearly any possible quantum gate. Possibility of transparency due to single-photon transport across differentially detuned two-level emitters has been theoretically demonstrated, without applying any control field [40]. In view of the engrossing physics of collective effects in waveguide-integrated atomic systems, part of my PhD research was dedicated to the theoretical understanding of these effects in the *single-photon regime* of waveguide QED. Recent experiments have produced highly pure single-photon sources both in the microwave [42] and in the optical [43] regimes, which can be used to probe our model. Chapters 2-4 in this thesis present detailed analyses of this model, identifying, in parallel, some experimentally relevant platforms for its realization.

It is also interesting to shift perspective by viewing the photons in a waveguide continuum as a vacuum reservoir in the absence of any classical fields. When quantum emitters are coupled to the same waveguide, an effective interaction between any two emitters is entailed, which produces long-range inter-emitter entanglement. The interaction strength depends directly on the efficiency of emission into the guided modes. Such an interaction is known as *dissipative coupling*, as the coupling is established via photon leakage. It does not support a Hamiltonian description and surfaces only from a master-equation description of the emitters obtained by eliminating the bath's degrees of freedom. More generally, the interaction mediated by an optical fiber wields flexible

control on both coherent (Hermitian-like) and dissipative couplings, leading to the dual possibilities of level repulsion and level attraction. By tuning the spatial separation between any two emitters, the coherent-part of the inter-emitter coupling can be suppressed and the coupling morphs into a purely dissipative one. Dissipatively coupled systems interfacing purely via a waveguide offer the perfect platform to engineer anti-PT symmetry - a characteristic hallmark of *non-Hermitian effective Hamiltonians*. Anti-PT symmetry is the characteristic of a Hamiltonian which changes sign under the action of time-reversal followed by a parity flip. A close investigation of anti-PT symmetry reveals some standout characteristics in the normal modes of the system, which props it up not only for the study of topological phenomena associated with phase transition but also for sensing utilties [44–49]. It was recently shown by us that anti-PT symmetric couplings can also be used to enhance nonlinear interconversion between microwave and optical fields [50]. If one takes stock of current information technologies, superconducting qubits have emerged as one of the top contenders for quantum information processing and have already found chip-scale implementations as prototypical quantum processors operating at low temperatures in the microwave regime [51, 52]. On the other hand, quantum communication technologies prefer to use optical fibers for transmitting quantum information over long distances, since such fibers can be operated even at room temperatures with low signal losses [53, 54]. Given this state of affairs, a reliable interface for the conversion of microwave to optical frequency and vice versa is paramount to the sustainability of robust, large-scale quantum communication networks.

All theoretical schematics require proper context - an experimental test bed to verify the predicted behavior. In light of the immense topicality of cavity magnonics, we contextualized our theoretical predictions in a hybrid cavity-magnetic setup, by considering a microcavity coupled dissipatively to magnetic excitations in a YIG sphere, a macroscopic ferrimagnetic sample. The quasiparticle representing low-energy spin waves in a magnetic sample is called a *magnon*, which acts as a Bosonic mode in the limit of large spin. Endowed with a very high spin density, YIG is a suitable candidate for studying the associated signatures of magnon-photon couplings and also to implement anti-PT symmetry [48]. Our initial pursuits in the study of anti-PT symmetry have

shown plenty of promise and we believe that this might be the tip of the iceberg. A deeper scrutiny of anti-PT symmetry should guide us closer to unraveling its full potential. Chapters 5-7 in this thesis have been dedicated to the topic of anti-PT symmetry and its specific applications to cavity-magnonic systems. Given the plethora of ongoing experimental activities in cavity magnonics, we believe that our theoretical predictions should allow laboratory implementation.

This thesis is written based on the following published and unpublished research articles, organized in a chronological order,

1. D. Mukhopadhyay and G. S. Agarwal, *Multiple Fano interferences due to waveguide-mediated phase coupling between atoms*, Phys. Rev. A **100**, 013812 (2019).

2. D. Mukhopadhyay and G. S. Agarwal, *Transparency in a chain of disparate quantum emitters strongly coupled to a waveguide*, Phys. Rev. A **101**, 063814 (2020).

3. J.M. P. Nair, D. Mukhopadhyay, and G. S. Agarwal, *Enhanced Sensing of Weak Anharmonicities through Coherences in Dissipatively Coupled Anti-PT Symmetric Systems*, Phys. Rev. Lett. **126**, 180401 (2021).

4. G. S. Agarwal and D. Mukhopadhyay, *Coupling Quantum Antennas to Fibers and Waveguides*, arXiv:2111.03200.

5. D. Mukhopadhyay, A. Akimov, A. Zheltikov, and G. S. Agarwal, *Quantum Optics in Integrated Waveguides and Photonic Crystal Fibres*, edited by G. Moody and V. Sorger in "Roadmap on Integrated Quantum Photonics", J. Phys:Photonics **4** 012501 (2022).

6. D. Mukhopadhyay, J. M. P. Nair, and G. S. Agarwal, *Anti-PT symmetry enhanced interconversion between microwave and optical fields*, Phys. Rev. B **105**, 064405 (2022).

Section 5.4 in Chapter 5 has partially overlapping content with another recent publication (Phys. Rev. B. **105**, 214418 (2022)). Other collaborative research articles, including Phys. Rev. B. **103**, 224401 (2021) and Phys. Rev. Res. **4**, 013131 (2022) have been excluded from this thesis, and find mention only in related contexts.

The thesis is divided into seven main chapters apart from a short chapter on concluding remarks. Chapter 2 introduces the theoretical framework for studying waveguide QED, particularly in the context of single-photon excitation regimes. In chapter 3, we extensively discuss how Fano interference due to photon transport across a chain of identical atoms leads to multiple Fano minima in the reflection profile. In chapter 4, we demonstrate the emergence of transparency in a chain of non-identical atoms embedded on a waveguide, without applying any external control field. Chapter 5 reviews the general characteristics of anti-PT symmetry as well as its optical realizations, with a special focus on cavity magnonics. The next two chapters bring to light two important applications of this symmetry. In particular, chapter 6 delineates a scheme to detect very weak nonlinearities, while chapter 7 highlights the role of anti-PT symmetry in enhancing the interconversion between microwave and optical fields.

2. WAVEGUIDE QED: INSIGHTS FROM SCATTERING THEORY

There exist various theoretical prescriptions customized to the study of photonic transport across a periodic chain of emitters coupled to a waveguide, particularly when the photonic dispersion relation is assumed to be linear. In our research, we have adopted two of the foremost systematic approaches to this end: (i) real-space formalism for analyzing scattering eigenstates in few-photon manifolds, and (ii) master-equation formulation for analyzing both semiclassical and quantum transport of light. The first half of my thesis is dedicated to the first approach, and my analysis would be contextualized within the single-excitation manifold. The second approach acquires more relevance from the point of view of an effective waveguide-mediated coupling between distant emitters, and will be shelved until Chapter 4. Theoretical studies in waveguide QED were inspired primarily by the wealth of experimental progress in waveguide-integrated nanophotonics, particularly with superconducting circuits. One of the earliest theoretical endeavors in this direction was by Shen and Fan in 2005 [9] who had advanced the real-space formalism for the first time. This was subsequently generalized into two-photon and multiphoton excitation regimes. The few-photon regime of waveguide QED is indubitably quantum in nature and therefore, merits customized exploration in its own right. As was shown by the pioneering work of [9], the transmission properties of a photon can be conveniently solved in the real-space representation, yielding tailormade solutions to the traveling fields in different spatial regimes. Of particular interest is a finite-sized atomic array periodically spaced out in a lattice configuration and coupled strongly to the 1D structure. The scenario becomes especially intriguing when the impact of spatial separation L is considered, as the collective emission properties can be drastically different for different ratios of L/λ, where λ is the resonant waveguide mode. However, before the collective radiance due to atomic ensembles can be analyzed and their repercussions properly assessed, it is important to develop the theoretical foundation of the real-space formalism. This is the ultimate objective of the current chapter.

We organize the content of this chapter as follows. In Sec. 2.1, we derive the real-space Hamil-

tonian of a single 2LA coupled to a 1D waveguide, with the atom-photon interaction Hamiltonian subject to the RWA. Sec. 2.2 acts as a link between the real-space formulation and interpretations of the photonic transport properties, with perspectives borrowed from the scattering theory. In Sec. 2.3, we analyze the problem for a single atom, and formally extend this analysis to the case of multiple atoms in 2.4. A short summary of the basic ideas is presented in Sec. 2.5.

2.1 Real-space formulation of the problem

A simple model of a 2LA coupled to the evanescent fields in a waveguide is depicted in Fig. 2.1(a). Several prominent solid-state systems feature this configuration, such as a superconducting quantum bit coupled to a coplanar transmission line, an atom coupled to a toroidal microresonator, and a QD interfacing with surface plasmons. Fig. 2.1(b) exhibits a variant of the previous model, where the 2LA is directly coupled to photons in the waveguide. This model is relevant to atomic cavity-QED experiments and also experiments involving line-defects in photonic bandgap crystals. It has been demonstrated that there exists a one-to-one correspondence between the transmission and reflection of photons in the side-coupled configuration and those in the directly coupled configuration [22]. Both these architectures bear connections with a number of problems important in condensed-matter physics, as for instance, the spin-boson problem which has found a revival of interest particularly in the context of various implementations of quantum bits [55]. However, in traditional condensed-matter perspectives, the photons in the 1D continuum play the role of the bosonic bath and are therefore traced out from the full system. This is different from the spirit in which we go about analyzing the coupled system in the current and the two subsequent chapters of this thesis. In condensed-matter context, the focal interest is on the dynamics of the spin or impurity (akin to our 2LA). We are mostly concerned with the dynamics of photons in the 1D continuum. In particular, our analysis will be premised on systems described in Fig. 2.1(a).

Model and Hamiltonian: A general Hamiltonian of a 2LA side-coupled to a 1D waveguide is

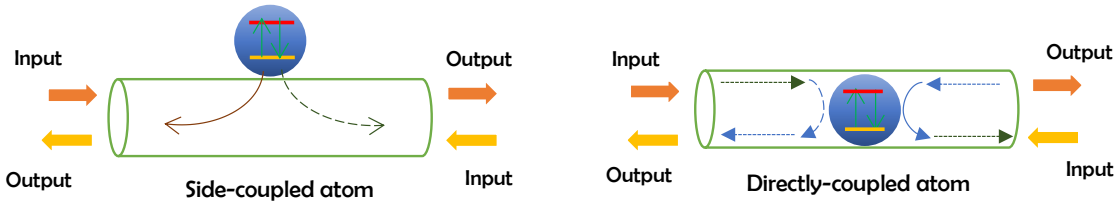

Figure 2.1: Single atom: (a) Side-coupled; (b) Directly coupled configuration. The location of the atom, assumed a point dipole, can be taken to be the origin, i.e., $x = 0$.

given by $\mathcal{H} = \mathcal{H}_0 + \mathcal{H}_{\text{int}}$, where

$$\begin{aligned} \mathcal{H}_0 &= \int \mathrm{d}k\, \hbar\omega(k) a^\dagger(k) a(k) + \hbar(\omega_e - i\Gamma_0) \left|e\right\rangle \left\langle e\right|, \\ \mathcal{H}_{\text{int}} &= \int \mathrm{d}k\, \hbar\mathcal{J}_k (a_k^\dagger \left|g\right\rangle \left\langle e\right| + a_k \left|e\right\rangle \left\langle g\right|), \end{aligned} \tag{2.1}$$

where $\mathcal{H}_0$ and $\mathcal{H}_{\text{int}}$ signify the free and the interaction Hamiltonians respectively. The first term in $\mathcal{H}_0$ represents the propagating photon fields of frequency ω_k and wavenumber k. The 2LA is described by the second term in $\mathcal{H}_0$, with transition frequency ω_e between the ground and the excited states $|g\rangle$ and $|e\rangle$ respectively. The ground-state energy has been calibrated at zero on the energy scale, and the operators $|g\rangle\langle e|$ and $|e\rangle\langle g|$ denote the lowering and raising operators on the 2LA. The imaginary term $i\Gamma_0$ accounts for spontaneous emission into photon modes outside of the 1D continuum, which dominates in atomic systems. In superconducting systems, one also has the possibility of dephasing which plays a similar role. The interaction of the propagating photons with the 2LA is governed by H_{int}, which is written in the rotating-wave approximation. This is valid for typical light-matter coupling strengths achieved in experiments, although, for studying the purely quantum regime of *a single or few photons*, this approximation naturally holds water. In the above expressions, a_k ($a_k^\dagger$) is the photon annihilation (creation) operator, and the coupling strength of a photon of wave vector k with the emitter is $\mathcal{J}_k$. This coupling strength is given by $\mathcal{J}_k = \left(\frac{\hbar\omega(k)}{2\varepsilon_0 V}\right)^{1/2} \mathbf{p}\cdot\hat{e}_k$, where $\mathbf{p} = \mathbf{p_{eg}} \left|\mathbf{e}\right\rangle \left\langle \mathbf{g}\right| + \mathbf{p_{ge}} \left|\mathbf{g}\right\rangle \left\langle \mathbf{e}\right|$ equals the dipole moment vector of the atom, $\hat{e}_k$ is the polarization unit vector of the photon mode, and ε_0 is the free-space permittivity

[56]. The expression is written in SI units, and that will be the chosen convention throughout this thesis. The atom is assumed to be of subwavelength dimensions and can therefore, be treated as a localized point dipole at $x = 0$. An ideal emitter-waveguide model would be one which totally excludes dissipation into free space. From a practical point of view, however, we only require that the decoherence effects are weak compared to the efficiency of emission into the guided modes.

Dispersion relation: The energy-momentum dispersion ($\omega(k)$ vs k) of photons in various 1D waveguides is generally nonlinear and depends on the geometrical and material properties of the waveguide. It is, however, convenient and reasonable to assume linear dispersion to describe the theoretical approach discussed here. We can linearize the dispersion near some arbitrary frequency ω_0 with the corresponding wave vector k_0, as shown in Fig. 2.2 [22]. The approximate linearized dispersion of $\omega(k)$ around k_0 (right-moving photons) and k_0 (left-moving photons) would then read

$$\begin{aligned} \omega(k \simeq -k_0) &\simeq \omega_0 - v_g(k + k_0) \quad \text{(left-moving branch)}, \\ \omega(k \simeq k_0) &\simeq \omega_0 + v_g(k - k_0) \quad \text{(right-moving branch)}, \end{aligned} \tag{2.2}$$

where $v_g = \left| \dfrac{\partial \omega(k)}{\partial k} \right|$ is the group velocity of these photons, assumed positive. We now change variables as $k + k_0 = k_L$ and $k - k_0 = k_R$, where the subscripts L and R would, henceforth, be referred to as the left- and right-propagating branches. Since we are interested in a narrow bandwidth of frequencies in the neighborhood of ω_0, we can extend the range of wavenumbers k_L and k_R to $(-\infty, \infty)$ and drop the subscripts L and R inside the integral. Similarly, we can decompose the field modes into two sets of operators, $a_L(k)$ and $a_R(k)$, corresponding to these branches. This divides the photonic energy contribution between the left- and right-traveling modes, and yields,

in the quasicontinuum limit,

$$\int_{-\infty}^{\infty} \mathrm{d}k\, \hbar\omega(k) a(k)^\dagger a(k) \simeq \underbrace{\int_{-\infty}^{\infty} \mathrm{d}k\, \hbar(\omega_0 - v_g k) a_L(k)^\dagger a_L(k)}_{\text{left-going modes}} + \underbrace{\int_{-\infty}^{\infty} \mathrm{d}k\, \hbar(\omega_0 + v_g k) a_R(k)^\dagger a_R(k)}_{\text{right-going modes}} . \tag{2.3}$$

In deriving Eq. (2.3), we have also assumed that the dispersion relations are non-degenerate, so that there is no undercounting of states. We also note in this context that the linearization procedure is analogous to a commonly applied procedure in electronic transport problems, where k_0 is chosen to be the Fermi wave vector.

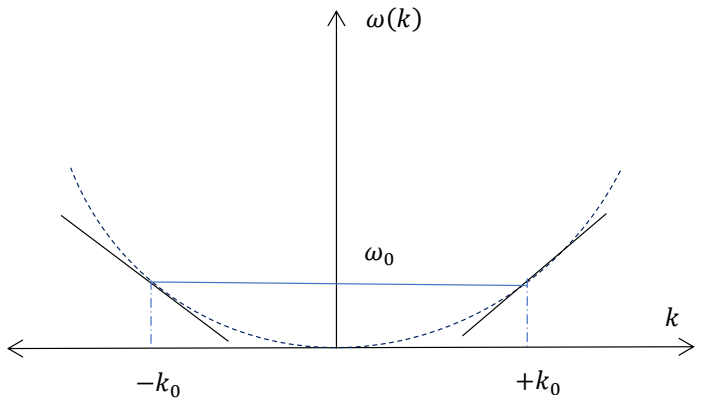

Figure 2.2: Linearization of the dispersion Relation near $\pm k_0$.

Transformation into a rotated frame: We can now switch to a frame rotating at the frequency ω_0, about which we had linearized our dispersion. Such a rotation is underpinned by the unitary operator $\mathcal{U}_r = e^{i\omega_0 \hat{N} t}$, where $\hat{N} = \int \mathrm{d}k\, [a_L(k)^\dagger a_L(k) + a_R(k)^\dagger a_R(k)] + |e\rangle\langle e|$ is the total excitation-number operator. Under this rotation, the Hamiltonian transitions as $\mathcal{H} \to \mathcal{U}_r \mathcal{H} \mathcal{U}_r^\dagger - i\hbar \dfrac{\partial \mathcal{U}_r}{\partial t} \mathcal{U}_r^\dagger$, and we obtain a new, effective Hamiltonian $\tilde{\mathcal{H}}$ in the rotating frame. Since $[\hat{N}, \mathcal{H}] = 0$, the transformed Hamiltonian is given simply by $\tilde{\mathcal{H}} = \mathcal{H} - \hbar\omega_0 \hat{N}$, which describes a rigid shift in the energy scale

of the system. Thus, the constituents become

$$\begin{aligned}\tilde{\mathcal{H}}_0 &= \int \mathrm{d}k\, \hbar v_g k \Big(a_R^\dagger(k) a_R(k) - a_L(k)^\dagger a_L(k) \Big) + \hbar(\tilde{\omega}_e - i\Gamma_0) \left|e\right\rangle \left\langle e\right|, \\ \tilde{\mathcal{H}}_{\text{int}} &= \int \mathrm{d}k\, \hbar \mathcal{J}_k \Big[\Big(a_R^\dagger(k) + a_L^\dagger(k) \Big) \left|g\right\rangle \left\langle e\right| + \Big(a_R(k) + a_L(k) \Big) \left|e\right\rangle \left\langle g\right| \Big], \end{aligned} \tag{2.4}$$

where $\tilde{\omega}_e = \omega_e - \omega_0$ is a shifted atomic frequency. Note that the interaction term remains conserved under this transformation. For brevity, we will dispense with the tilde notations, with the understanding that our analysis pertains to a rotated frame.

Introduction to real space: We now write down an effective representation of $\mathcal{H}$ in real space, where the evolution of the incident photons is more conveniently described. To this end, we take the photon operators in momentum space to be the Fourier transforms of real-space operators,

$$\begin{aligned} a_{L,R}(k) &= \frac{1}{\sqrt{2\pi}} \int_{-\infty}^{\infty} \mathrm{d}x\, a_{L,R}(x) e^{-ikx}, \\ a_{L,R}^\dagger(k) &= \frac{1}{\sqrt{2\pi}} \int_{-\infty}^{\infty} \mathrm{d}x\, a_{L,R}^\dagger(x) e^{ikx}, \end{aligned} \tag{2.5}$$

where $a_L(x)$ annihilates a left-moving photon and $a_R(x)$ annihilates a right-moving photon at the position x along the waveguide. These new operators satisfy the Bosonic commutation relation in *real space*, i.e. $[a_{R(L)}(x), a_{R(L)}^\dagger(x')] = \delta(x - x')$ and $[a_{R(L)}(x), a_{R(L)}(x')] = 0$. Substituting Eq. (2.5) into the Hamiltonian, we can find an effective real-space Hamiltonian for a 2LE coupled to the 1D continuum. For instance, in the position space, the free-field Hamiltonian would be recast into

$$\begin{aligned} \mathcal{H}_0^{(\text{field})} &= \int \mathrm{d}k\, \hbar v_g k \Big(a_R^\dagger(k) a_R(k) - a_L(k)^\dagger a_L(k) \Big) \\ &= i \int \mathrm{d}x\, \hbar v_g \Big(a_L^\dagger(x) \frac{\partial}{\partial x} a_L(x) - a_R^\dagger(x) \frac{\partial}{\partial x} a_R(x) \Big) \end{aligned} \tag{2.6}$$

Likewise, on switching to Fourier space, the interaction term also changes into

$$\begin{aligned}\mathcal{H}_{\text{int}} &= \int \mathrm{d}k\, \hbar\mathcal{J}_k \Big[\Big(a_R^\dagger(k) + a_L^\dagger(k) \Big) |g\rangle \langle e| + \Big(a_R(k) + a_L(k) \Big) |e\rangle \langle g| \Big] \\ &= \int \mathrm{d}x\, \hbar\mathcal{J}(x) \Big[\Big(a_R^\dagger(x) + a_L^\dagger(x) \Big) |g\rangle \langle e| + \Big(a_R(x) + a_L(x) \Big) |e\rangle \langle g| \Big]\end{aligned} \tag{2.7}$$

in which we have introduced the Fourier transform of the coupling strength $\mathcal{J}_k$ thus:

$$\mathcal{J}_k = \frac{1}{\sqrt{2\pi}} \int_{-\infty}^{\infty} \mathrm{d}x\, \mathcal{J}(x) e^{ikx} \tag{2.8}$$

In deriving Eq. (2.6), we have made use of the property $\delta(x - x') = \frac{1}{2\pi} \int_{-\infty}^{\infty} \mathrm{d}k\, e^{ik(x-x')}$. Details on the steps leading to (2.6) are provided in Appendix A.1. It is no coincidence that the free-field Hamilonian in (2.6) involves partial spatial derivatives of the annihilation operators. This is, in fact, connected with the interpretation of the momentum operator in real-space. Recall that ordinary quantum mechanics requires the momentum operator to be given by $\hat{p} = -i\hbar \dfrac{\partial}{\partial x}$ in 1D position representation. Thus, the appearance of first-order partial derivatives is hardly a mystery.

Hamiltonian under the slowly-varying-envelope approximation: The interaction Hamiltonian can be further simplified under the slowly-varying-envelope approximation, whereby the coupling parameter $\mathcal{J}_k$ can be taken to be independent of k, i.e., $\mathcal{J}_k \approx \dfrac{\mathcal{J}}{\sqrt{2\pi}}$ (the factor of $\sqrt{2\pi}$ is merely introduced for convenience). This makes sense considering that the factor $\left(\dfrac{\hbar\omega_k}{2\varepsilon_0 V} \right)^{1/2}$ varies slowly over the narrow bandwidth of waveguide frequencies that contribute maximally to the coupling. With this assumption, the Fourier transform of $\mathcal{J}_k$ reduces to a delta-function in x, centered on the origin, i.e.,

$$\mathcal{J}(x) = \mathcal{J}\delta(x) \tag{2.9}$$

Consequently, we get the simplified interaction term as

$$\mathcal{H}_{\text{int}} = \hbar\mathcal{J}\left[\left(a_R^\dagger(0) + a_L^\dagger(0)\right)|g\rangle\langle e| + \left(a_R(0) + a_L(0)\right)|e\rangle\langle g|\right]. \tag{2.10}$$

In the real-space picture, it can at once be seen from Eq. (2.10), that the interaction only couples up the field modes with the atom at the precise location of the atom, which is $x = 0$. Viewed in this way, the atom acts as a localized scattering agent which would partly reflect and partly transmit photons launched through the waveguide. This would be veritably manifested through our analytical treatment in Sec 2.3. But to start off, it is useful to further consolidate foundations of our approach by reviewing some of the core perspectives from scattering theory, which would offer intuitive insights into the problem.

2.2 Perspectives from scattering theory

Scattering theory is a methodical framework to study scattering of waves and particles from a central or localized potential, and it finds extensive applications in different branches of physics. In what follows, we shortly discuss this theoretical technique, contextualized within the paradigm of waveguide QED. In scattering theory, it is customary to introduce a matrix S, also termed the scattering matrix, which encapsulates all the scattering properties of the scattering source/agent. This matrix connects the scattered output to the incident input via the unitary time-evolution operator of the joint system consisting of the injected particle/wave and the scattering source. In a waveguide QED framework, such a technique can be employed for characterizing the transport properties of photons as they encounter a scattering medium, which could absorb and subsequently emit photons into the guided modes of the quasi-continuum. It is well known in literature that the S matrix for scattering of an single-photon state is defined by the matrix elements

$$S_{p;k} = \langle p|\, S\, |k\rangle\,, \tag{2.11}$$

where $|k\rangle$ and $|p\rangle$ stand for the incoming and the outgoing photonic states, respectively [57]. Here, the quantities k and p denote the incoming and the outgoing momenta (in units of $\hbar$) of the photon. These incoming and outgoing states are considered to be free states in the interaction picture, existing in the distant past and in the distant future respectively. The corresponding operator

$$S = \lim_{\substack{t\to-\infty \\ T\to\infty}} U_I(T,t) \tag{2.12}$$

is given simply by the time-evolution operator $U_I(T,t) = e^{iH_0 t/\hbar} e^{-iH_{\text{int}}(T-t)/\hbar} e^{-iH_0 t/\hbar}$ calculated in the interaction picture, wherein H_0 represents the free-Hamiltonian part and H_{int} corresponds to the interaction energy between the photons and the scattering medium. The scattering matrix can also be redefined as

$$S_{p;k} = \left\langle p^- \middle| k^+ \right\rangle, \tag{2.13}$$

where we have introduced the scattering eigenstates $|k^+\rangle$ and $|p^-\rangle$, which evolve unitarily in the interaction picture from/into a perfectly free-photon state either in the distant past or into the distant future:

$$\begin{aligned} \left|k^+\right\rangle &= \underbrace{\lim_{t\to-\infty} U_I(0,t)}_{:=\Omega_+} |k\rangle = \Omega_+ |k\rangle, \\ \left|p^-\right\rangle &= \underbrace{\lim_{T\to\infty} U_I(0,T)}_{:=\Omega_-} |p\rangle = \Omega_- |p\rangle. \end{aligned} \tag{2.14}$$

Thus, to quote Ref. [8], the S matrix, which can also be expressed as $S = \Omega_-^\dagger \Omega_+$, describes how an incoming state of monochromatic, free photons evolves via a local interaction with atoms into a superposition of outgoing monochromatic photons.

Scattering in 1D: In the context of waveguide-mediated photon transport, we present an ap-

proach which treats the atom-photon dynamics in real space, which is particularly convenient for discussing steady-state photon transport from one space-time point to another. We start with an ansatz for the full scattering eigenstate $|k^+\rangle$ of the full Hamiltonian, subject to specified unscattered state $|k\rangle$ of the free Hamiltonian H_0. Under the purview of the RWA, the total number of photons must be conserved during the scattering process. Thus, when all other interaction channels are suppressed relative to the scattering channel, energy conservation would be observed. To calculate different amplitudes of the scattering eigenstate, we employ the time-independent Schrödinger equation

$$H\left|k^+\right\rangle = \mathcal{E}_k\left|k^+\right\rangle, \tag{2.15}$$

where $\mathcal{E}_{\mathbf{k}} = \hbar\omega(k)$ is the energy of the incident photon*. This has to be supplemented by appropriate boundary conditions that determine the propagation direction of the incident photons. Quite naturally, the photon can be administered along the right-moving and/or left-moving channels. The nonequilibrium dynamics of the transport can be probed in experiments by measuring the transmission and reflection of photons at the opposite ports of the waveguide. For a side-coupled 2LA, the transmission coefficient can be calculated from the relative number of photons remaining in the incident channel after the scattering event, while the reflection coefficient can be determined by counting relative photons in the opposite channel. If the longitudinal dimension of a 1D waveguide is supposed to be large, then the frequency spacing between the allowed modes is small enough to merit a quasi-continuum description of these guided modes. In other words, an isolated waveguide would act as a 1D reservoir of electromagnetic vacuum fields. Therefore, the total number of photons, whether left-moving or right-moving, can be expressed in either momentum space or real space as

$$\int \mathrm{d}k\, a^\dagger_{L,R}(k)a_{L,R}(k) = \int_{-\infty}^{\infty} \mathrm{d}x\, a^\dagger_{L,R}(x)a_{L,R}(x), \tag{2.16}$$

*Since we have now transitioned into the rotating frame, the single-photon dispersion relation is to be assumed as $\omega(k) = v_g k$.

where the equality follows from Eq. (2.5) upon invoking the property of Dirac-Delta function. So the operator $a^\dagger_{L,R}(x)a_{L,R}(x)$ can be interpreted as the density of left-moving (L) or right-moving (R) photons at the location x. When we take expectation value of this operator in the incident state $|k\rangle$, we obtain the input photon flux, whereas the output photon flux is evaluated by taking the expectation value in the state $|k^+\rangle$. For example, the transmission and reflection coefficients for a right-moving incident photon would be respectively given by

$$\begin{aligned} T &= \frac{\langle k^+|\, a^\dagger_R(x)a_R(x)\,|k^+\rangle}{\langle k^+|\, a^\dagger_R(x)a_R(x)\,|k^+\rangle} \\ R &= \frac{\langle k^+|\, a^\dagger_R(x')a_R(x')\,|k^+\rangle}{\langle k^+|\, a^\dagger_R(x')a_R(x')\,|k^+\rangle} \end{aligned} \tag{2.17}$$

where the denominators are a measure of the incident photon flux and are independent of x and x' [8]. Assuming the scattering source to be located at the origin, we choose $x > 0$ and $x' < 0$. We now calculate the single-photon scattering eigenstate of $\mathcal{H}$, following the seminal approach of Shen and Fan [9, 22], which would allow us to evaluate the above coefficients.

2.3 Single-excitation regime: single 2LA coupled to a waveguide

The full system Hamiltonian for a single atom interacting with the modes of the waveguide continuum was derived as

$$\begin{aligned} \mathcal{H} = \underbrace{\hbar(\omega_e - i\Gamma_0)\,|e\rangle\,\langle e|}_{\text{atomic part}} + \underbrace{i\hbar v_g \int_{-\infty}^{\infty} dx \left(a^\dagger_L(x)\frac{\partial a_L(x)}{\partial x} - a^\dagger_R(x)\frac{\partial a_R(x)}{\partial x} \right)}_{\text{free field}} + \\ \underbrace{\hbar J \left[\left\{ a_L(0) + a_R(0) \right\} |e\rangle\,\langle g| + \text{h.c.} \right]}_{\text{atom-field interaction under rotating-wave approximation}}, \end{aligned} \tag{2.18}$$

The total excitation operator

$$\hat{N} = \int \mathrm{d}x \left[a_L(x)^\dagger a_L(x) + a_R(x)^\dagger a_R(x) \right] + |e\rangle\,\langle e|$$

commutes with $\mathcal{H}$, i.e., $[\hat{N}, \mathcal{H}] = 0$. It is, therefore, a conserved quantity. This allows one to work within the manifold of a given number of excitations. We now consider the problem of a single photon administered into the atom-waveguide apparatus. The Hamiltonian is non-Hermitian due to the presence of the dissipation term Γ_0. In the following, we calculate $|k^+\rangle$ using the Hermitian approximation, whereby we neglect the impact of Γ_0. We can always reintroduce the effect of Γ_0 by replacing ω_e with $\omega_e - i\Gamma_0$.

Formal expressions for reflection and transmission: We first chart out a theoretical template to probe the reflection and the transmission from the system. If we launch a photon with definite frequency into right-moving channel, the input state of this photon can be expressed as

$$|k\rangle = a_R^\dagger(k)\,|\phi\rangle = \frac{1}{\sqrt{2\pi}} \int \mathrm{d}x\, e^{ikx} a_R^\dagger(x)\,|\phi\rangle \tag{2.19}$$

where $|\phi\rangle = \left(\prod_k |0\rangle_k\right) \bigotimes |g\rangle$ represents the electromagnetic vacuum with the 2LA in its ground state, with the notation $\bigotimes$ signifying the tensor product between the photonic and atomic states. It is easy to compute the incident photon flux in this state and it turns out to be

$$\Phi_{\text{inc}}(x) \propto \langle k|\, a_R^\dagger(x) a_R(x)\,|k\rangle = \frac{1}{\sqrt{2\pi}}, \tag{2.20}$$

which, being a constant in space, is emblematic of its free-photon character. Considering different scattering processes, we write an ansatz for the *single-photon scattering eigenstate*,

$$\left|k^+\right\rangle = \frac{1}{\sqrt{2\pi}} \left[\int \mathrm{d}x \left(\psi_{R,k}(x) a_R^\dagger(x) + \psi_{L,k}(x) a_L^\dagger(x) \right) |\phi\rangle + c_k\,|\phi_1\rangle \right], \tag{2.21}$$

where $|\phi_1\rangle = (|e\rangle\langle g|)\,|\phi\rangle = \left(\prod_k |0\rangle_k\right) \bigotimes |e\rangle$ embodies the electromagnetic vacuum with the 2LA in its excited state. The functions $\psi_{R,L}(x)$ describe the wavefunctions or scattering amplitudes subject to the incident photonic state, while c_k denotes the atomic excitation amplitude. This ansatz is perfectly justified, given that the total excitation number $\hat{N}$ commutes with the Hamiltonian - this

leaves us with only three options: (i) the atom absorbs the photon and gets excited, (ii) the photon proceeds rightward, or (iii) the photon changes track and flips direction. This is shown in Fig. . Note that while the vacuum ket $|\phi\rangle$ is normalized according to $\langle\phi|\phi\rangle = 1$, the monochromatic, free-photon states subscribe to the Dirac-Delta normalization, i.e., $\langle k|k'\rangle = \delta(k-k')$. This is because the set $\{|k\rangle\}$ forms a complete, orthogonal basis of scattering continuum states. Similarly, one has the orthonormalization condition for the $\{|k^+\rangle\}$ states, $\langle k^+|k'^+\rangle = \delta(k-k')$. In this scattering eigenstate, one can infer the outgoing fluxes (rightward and leftward) by computing

$$\begin{aligned}\Phi_{\text{out}}(x>0) &\propto \left\langle k^+\right| a_R^\dagger(x)a_R(x)\left|k^+\right\rangle = \frac{|\psi_{R,k}(x)|^2}{2\pi}\\ \Phi_{\text{out}}(x<0) &\propto \left\langle k^+\right| a_R^\dagger(x)a_R(x)\left|k^+\right\rangle = \frac{|\psi_{L,k}(x)|^2}{2\pi}\end{aligned} \tag{2.22}$$

Therefore, upon invoking Eq. (2.17) and (2.20), we obtain the transmission and reflection coefficient as

$$T = |\psi_{R,k}(x>0)|^2, \quad R = |\psi_{L,k}(x<0)|^2. \tag{2.23}$$

Problem statement and exact solution: We now solve the Schrodinger equation $\mathcal{H}\,|k^+\rangle = \hbar v_g k\,|k^+\rangle$ to obtain the relevant amplitudes $\psi_{R,k}(x)$, $\psi_{L,k}(x)$, subject to the following boundary conditions

$$\psi_{R,k}(x<0) = e^{ikx}, \quad \psi_{L,k}(x>0) = 0, \tag{2.24}$$

In other words, the problem is framed as follows. To the left of the atom, i.e., in the region $x<0$, only the incident plane wave propagates along the right-moving channel, and we do not know a priori the solution for the left-going field. To the right of the atom, i.e., for $x>0$, we know that there is no left-going field (simply because there is none incident!), but we would like to eke out the solution for the right-going wave. On applying the Schrodinger equation, we obtain three coupled

linear equations for three unknown scattering amplitudes,

$$\begin{aligned}\bigg(-iv_g\frac{\partial}{\partial x}-v_gk\bigg)\psi_{R,k}(x)+\mathcal{J}c_k\delta(x)=0,\\ \bigg(iv_g\frac{\partial}{\partial x}-v_gk\bigg)\psi_{L,k}(x)+\mathcal{J}c_k\delta(x)=0,\\ -\Delta_kc_k+\mathcal{J}\bigg(\psi_{R,k}(0)+\psi_{L,k}(0)\bigg)=0,\end{aligned}\tag{2.25}$$

in which we have introduced the frequency detuning $\Delta_k = v_gk-\omega_e$. The first two equations can be solved to yield plane waves with different weights in the two regions $x<0$ and $x>0$. Compactly expressed, the solutions are given by

$$\begin{aligned}\psi_{R,k}(x)&=\bigg[\Theta(x)+t_k\Theta(-x)\bigg]e^{ikx},\\ \psi_{L,k}(x)&=r_ke^{-ikx}\Theta(-x),\end{aligned}\tag{2.26}$$

where the parameter $\Gamma=\dfrac{\mathcal{J}^2}{v_g}$ determines the coupling strength between the emitter and the field and has the dimension of frequency. Also, $\Theta(x)$ represents the Heaviside step function defined as

$$\Theta(x)=\begin{cases}1, & x>0\\ \\ 0, & x<0\end{cases},\tag{2.27}$$

Substituting these solutions back into the differential equations in (2.25), we find the coefficients r_k, t_k and c_k to be

$$\begin{aligned}r_k&=-\frac{i\Gamma}{\Delta_k+i(\Gamma+\Gamma_0)},\\ t_k&=\frac{\Delta_k+i\Gamma_0}{\Delta_k+i(\Gamma+\Gamma_0)},\\ c_k&=\frac{\mathcal{J}}{\Delta_k+i\Gamma},\end{aligned}\tag{2.28}$$

where we have now plugged back the dissipation parameter Γ_0. Since $\psi_{R,k}(x>0)=t_k$ and

$\psi_{L,k}(x < 0) = r_k$, we find, upon comparison with Eq. (2.23), $T(k) = |t_k|^2$ and $R(k) = |r_k|^2$. By virtue of this connection, we can identify t_k and r_k to be the transmission and reflection amplitudes as the photon scatters off the atom. In the limit $\Gamma_0 \to 0$, these expressions satisfy the expected energy conservation rule

$$T(k) + R(k) = 1. \tag{2.29}$$

The single-photon reflection exhibits a Breit-Wigner-like (Lorentzian) line shape around the resonance $\Delta_k = 0$. When the atom is excited on resonance, it emits equally into both propagation directions of the waveguide channel. This emitted wave interferes destructively with the weak probe signal and the transmitted signal is completely quenched. Thus, a lossless side-coupled emitter behaves as a perfect nanomirror for propagating photons in a 1D continuum [9].

2.4 Generalization to multiple 2LAs

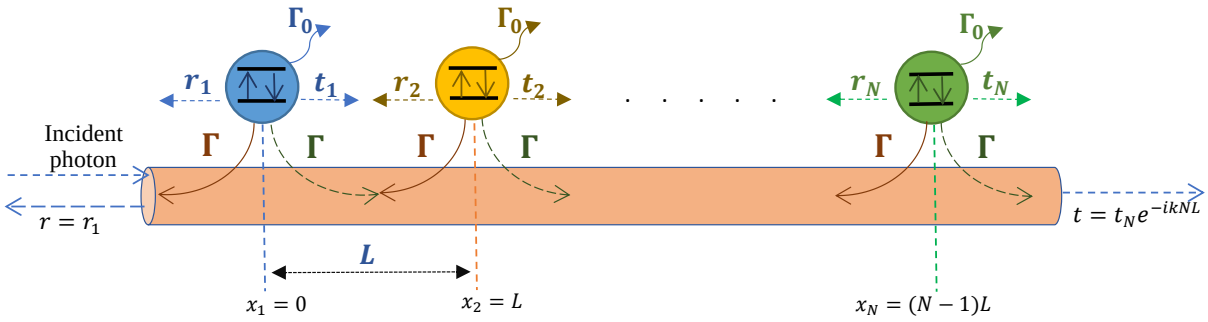

Figure 2.3: Chain of N identical 2LAs side-coupled to a 1D waveguide. r_j and t_j represent the reflection and transmission coefficients due to scattering from the j^{th} atom; L is the distance of separation.

In this section, we consider a periodic chain of atoms coupled to a waveguide. For simplicity, we assume the first atom to be located at the origin, so that the jth atom is placed at $x_j = (j -$

$1)L$. Multiatom-integrated lattice models can be rather intriguing, considering the wide variety of scattering pathways supported by these models. As a photon can address a multitude of atoms, with each of these interaction events featuring a finite probability, the overall effect is realized as a superposition of these events. Viewed from the perspective of waves, the spontaneous emission from these individual emitters can either coherently or destructively interfere to yield interesting transport properties. In order to analyze these models, we can extend our previous analysis to include multiple atoms interfacing with the waveguide. The free-field part of the Hamiltonian remains untouched, but the atomic and the interaction Hamiltonians are modified as follows

$$\begin{aligned}\mathcal{H}_{\text{atoms}} &= \hbar \sum_{j=1}^{N} (\omega_j - i\Gamma_0^{(j)}) \left|e\right\rangle_j \left\langle e\right|, \\ \mathcal{H}_{\text{int}} &= \hbar J \sum_{j=1}^{N} [\{a_L(x_j) + a_R(x_j)\} \left|e\right\rangle_j \left\langle g\right| + \text{h.c.}],\end{aligned} \tag{2.30}$$

where, for simplicity, we assumed identical coupling strengths for all the atoms. The jth atom has a transition frequency of ω_j. The single-photon scattering eigenstate should now be extended to account for multiple atomic excitations. We, therefore, solve for an eigenstate of the form

$$\left|k^+\right\rangle = \frac{1}{\sqrt{2\pi}} \left[\int \mathrm{d}x \left(\psi_{R,k}(x) a_R^\dagger(x) + \psi_{L,k}(x) a_L^\dagger(x) \right) \left|\phi\right\rangle + \sum_{j=1}^{N} c_k^{(j)} \left|\phi_1^{(j)}\right\rangle \right], \tag{2.31}$$

where $\left|\phi\right\rangle = \left(\prod_k \left|0\right\rangle_k \right) \bigotimes \left(\prod_j \left|g\right\rangle_j \right)$ is the ground state of the composite system, and $\left|\phi_1^{(j)}\right\rangle = \left(\prod_k \left|0\right\rangle_k \right) \bigotimes \left(\prod_{m \neq j} \left|g\right\rangle_m \left|e\right\rangle_j \right)$ symbolizes the state where the field is vacuum and only the jth atom is excited. Proceeding like in the case of a single atom, we can solve for the transmission and reflection coefficients in terms of the outgoing photon fluxes, which, in this case, would be given by

$$T = \left|\psi_{R,k}(x > x_N)\right|^2, \quad R = \left|\psi_{L,k}(x < x_1)\right|^2. \tag{2.32}$$

The scattering amplitudes are to solved from the Schrodinger equation $\mathcal{H} \left|k^+\right\rangle = \hbar v_g k \left|k^+\right\rangle$, which

yields a set of coupled linear equations as follows:

$$\begin{aligned}\Big(-iv_g\frac{\partial}{\partial x}-v_gk\Big)\psi_{R,k}(x)+\mathcal{J}\sum_{j=1}^{N}c_k^{(j)}\delta(x-x_j)=0,\\ \Big(iv_g\frac{\partial}{\partial x}-v_gk\Big)\psi_{L,k}(x)+\mathcal{J}\sum_{j=1}^{N}c_k^{(j)}\delta(x-x_j)=0,\\ -\Delta_k^{(j)}c_k^{(j)}+\mathcal{J}\Big(\psi_{R,k}(x_j)+\psi_{L,k}(x_j)\Big)=0\end{aligned} \tag{2.33}$$

Here, $\Delta_k^{(j)}=v_gk-\omega_j$ is the detuning of the jth atom. The solutions to the plane waves turn out to be

$$\phi_{kL}(x)=\begin{cases}r_1e^{-ikx}, & x<0\\ r_{j+1}e^{-ik(x-jL)}, & (j-1)L<x<jL\\ 0, & x>(N-1)L\end{cases}, \tag{2.34}$$

$$\phi_{kR}(x)=\begin{cases}e^{ikx}, & x<0\\ t_je^{ik(x-jL)}, & (j-1)L<x<jL\\ t_Ne^{ik(x-NL)}, & x>(N-1)L\end{cases}, \tag{2.35}$$

where we assumed $x_j=(N-1)L$. Plugging them back into (2.33), we obtain a set of linearly coupled equations involving the transmission and reflection coefficients, and the single-atom-excitation amplitudes.

$$\begin{aligned}t_je^{-ikL}-t_{j-1}+\frac{i\mathcal{J}c_k^{(j)}}{v_g}=0,\\ r_{j+1}e^{ikL}-r_j-\frac{i\mathcal{J}c_k^{(j)}}{v_g}=0,\\ t_{j-1}+r_j-\frac{\Delta_k^{(j)}c_k^{(j)}}{\mathcal{J}}=0.\end{aligned}$$

Eliminating the atomic excitation coefficients engenders a recursive matrix relation

$$\begin{bmatrix} r_j \\ t_{j-1} \end{bmatrix} = \mathcal{L}_j \begin{bmatrix} r_{j+1} \\ t_j \end{bmatrix}, \tag{2.36}$$

where the transfer matrix

$$\mathcal{L}_j = \begin{bmatrix} e^{ikL}(1 - i\delta_{k(j)}^{-1}) & -ie^{-ikL}\delta_{k(j)}^{-1} \\ ie^{ikL}\delta_{k(j)}^{-1} & e^{-ikL}(1 + i\delta_{k(j)}^{-1}) \end{bmatrix} \tag{2.37}$$

connects the left- and right-propagating fields across the jth atom, k is the wavenumber of the incident photon, $\delta_{k(j)} = \dfrac{v_g k - \omega_j + i\Gamma_0^{(j)}}{\Gamma}$, and $\Gamma = \dfrac{J^2}{v_g}$. The above relation can be solved iteratively to extract the ultimate reflection and transmission coefficients. In addition, we would need apposite boundary conditions, which are given by $t_0 = 1$, $r_{N+1} = 0$, $r_1 = r$, and $t = t_N e^{-iNkL}$. The correspondence between t and t_N accounts for the phase shift that the incident wave suffers till it scatters off the final atom. The joint consideration would yield the reflection and transmission coefficients as follows

$$r = \frac{\left(\prod_{j=1}^{N} \mathcal{L}_j\right)_{12}}{\left(\prod_{j=1}^{N} \mathcal{L}_j\right)_{22}}, \quad t = \frac{e^{-iNkL}}{\left(\prod_{j=1}^{N} \mathcal{L}_j\right)_{22}}. \tag{2.38}$$

The above expressions are absolutely general, and will apply irrespective of the individual emitter properties. However, because of the presence of the phase factors $e^{\pm ikL}$ and the generally differential detunings assigned to the emitters, it is analytically hard to find out compact expressions from the above. It turns out, however, that closed-form analytical expressions for r and t can be extracted for two independent scenarios: (i) when all the atoms are identical, and (ii) when the phase kL equals an integer multiple of π. These two settings would be the basis of the next two chapters.

2.5 Summary

To summarize, we have developed the real-space formulation to study photonic transport in real space, and are ready to apply this model to a comprehensive analysis of the single-photon regime. In the two forthcoming chapters, we would examine quantum interference effects due to absorption and emission from multiple atoms coupled to a waveguide and highlight the modifications they entail with regard to single-photon transport properties. We note that the same procedure outlined here can be applied to the study of correlated two-photon transport, and also multiphoton scattering problems, in general. Such systems can be analytically solved for a single 2LA interacting with the waveguide. However, for more than one atom, to the best of our knowledge, while numerical treatments have partially borne fruit, no analytical solution exists to date in the multiphoton excitation regime. We also note that certain resonators, waveguides, and photonic crystals admit modes that allow photon transport with specific polarizations [58–61]. As a result, the atomic emission is not symmetric in either direction. Chirality can also ensue from the application of an external magnetic field. The problem can be handled by assigning different coupling constants to the left- and right-propagating fields in Eq. (2.30). This would be a subject for further study.

3. FANO INTERFERENCES IN MULTIEMITTER WAVEGUIDE MODELS*

They focal point of this chapter is to analytically solve the waveguide model for an arbitrary number of *identical 2LAs* and bring out interesting possibilities originating from the *quantum interference of scattering pathways*. A system of two-level atoms coupled to a 1D continuum enables one to study a number of interesting collective effects depending on the chain size. These include, for example, modification of optical band structure [62], single-photon super-radiance [63], realization of Bragg mirrors [64, 65] and single-photon isolators [66]. The impact of chain size on spontaneous emission from one of the excited atoms was treated in [19]. The dynamical evolution of emitter excitations and photon pulses in a waveguide interfacing with multiple emitters was studied by Liao *et al.* in [67], by taking into account dipole-dipole couplings between the emitters. A significant amount of theoretical [13, 67–73] progress has been made in regards to single-photon transport in the context of these models, which has shed light on the role of spatial separation between atoms. Equally important a question was the feasibility of effecting strong atom-photon couplings in waveguide-based platforms. This was theoretically addressed in plasmonic structures [74] and photonic crystal waveguides [75, 76], which laid out a propitious roadmap for the novel possibilities. All of these were accompanied by an abundance of experimental works on closely associated configurations [4, 7, 63–65, 77–85], which reported efficient coupling of emitters to the guided modes.

Since a chain of two-level emitters strongly coupled to a waveguide scatters wave excitations, one can observe the emergence of asymmetric Fano lineshapes [36, 37] due to interference effects between the scattering amplitudes, a feature which is absent in the single-emitter scenario. This is an example of the Fano interference phenomenon [86], which has been extensively reviewed in Ref. [87] in the context of modern nanotechnology. The possibility of quantum interference stems from the existence of multiple quantum pathways in the transport of single photons. This

*A major part of this chapter is reprinted with permission from *Multiple Fano interferences due to waveguide-mediated phase coupling between atoms* by D. Mukhopadhyay and G. S. Agarwal, Phys. Rev. A **100**, 013812 (2019), published by the American Physical Society.

is because following each interaction with an atom, new pathways are created. Such interference phenomena give rise to multiple Fano minima depending on the relative location of atoms in the chain. The manifestation of multiple Fano minima has been discussed in other contexts ([88, 89]). In this chapter, we study the Fano interference phenomena in relation to *single-photon transport* through a waveguide. The atoms coupled to the waveguide are all assumed to be identical. By deriving exact expressions for the reflected and transmitted intensities, we show the development of Fano lineshapes with multiple reflection minima. The maximum number of minima typically allowed for a chain size of N is $(N-1)$. In the absence of DDI, the origin of Fano coupling can be attributed to the relative phase picked up by the propagating photon as it traverses from one emitter to the next. The waveguide-mediated phase coupling can occur over long distances (of the order of a wavelength), which has been reported in the context of two optical/microwave resonators [90, 91]. An adjustment of the emitter-spacing allows us to regulate this phase-coupling, which in turn controls the existence and the locations of Fano minima. Even though the Fano profiles are generally asymmetric, we observe a Dicke-type super-radiant effect in the reflection when the emitter-spacing equals an integral or half-integral multiple of the resonant wavelength. Discounting this special case, a key finding concerning the reflection lineshapes is the appearance of flat-topped broadband spectra in the highly reflecting domain, with the flatness as well as the frequency bandwidth increasing with the chain size. This is due to super-Gaussian nature of the spectra in frequency domain. For a large chain size, we find a finite band gap over which the system remains opaque to a single photon. This is enabled by the periodic nature of the lattice arrangement. Finally, we find that an increase in the atom-photon coupling strength opens up the possibility of observing new Fano minima in the reflection spectrum.

We structure the chapter in the following manner. In Sec. 3.1, we obtain the analytical formulae characterizing the reflection and transmission profiles. Based on these analytical expressions, we illustrate, in Sec. 3.2, the Fano lineshapes and extract the points of Fano minima. Certain features of these spectra are discussed in the light of Fano interference effect. In Sec. 3.3, we elaborate how an increase in the chain size has a direct role to play in the introduction of a spectral band gap.

Subsequently, in Sec. 3.4, we underline the appearance of symmetric lineshapes, with or without the presence of Fano minima, subject to pertinent choices of the spatial periodicity. Following that, we numerically report some non-Markovian signatures in the system in Sec. 3.5, when the coupling to the waveguide becomes quite large. Sec. 3.6 foregrounds the impact of lattice disorder when empirical uncertainties in the lattice spacing is accounted for. In Sec. 3.7, we repeat our theoretical analysis for the case when extraneous dissipation is included. Sec. 3.8 concludes with a summary of the key results in this manuscript.

3.1 Exact solution for identical atoms

We consider a one-dimensional array of N identical 2LAs spaced periodically apart from each other (recall Fig. 2.3). The real-space Hamiltonian for this system was derived in Chapter 2. Typically, one also needs to account for dipole-dipole interaction (DDI) between the atoms, especially when the spatial separation is in the extreme subwavelength domain of the resonant excitation [56]. Mu-Tian et al. demonstrated the appearance of non-Lorentzian lineshapes for the case of two emitters and brought to light the enhancement of asymmetry and splitting of the reflection spectrum as fundamental ramifications of the DDI [37]. In our model, we disregard the DDI contribution to the Hamiltonian by assuming that the atomic separation is size-wise comparable the resonance wavelength. In order to keep the physics transparent, we also ignore radiative losses into modes beyond the 1D continuum. This enables us to work with a perfectly lossless system. The more general dissipative case is sketched out in a later section.

In view of the fact that scattering occurs at the level of a single photon implying a single excitation in the system, the scattering eigenstate, with an eigenvalue $v_g k$, can be constructed as a superposition of single-photon and vacuum states,

$$\left|k^{+}\right\rangle = \frac{1}{\sqrt{2\pi}}\left[\int \mathrm{d}x \left(\psi_{R,k}(x)a_R^{\dagger}(x) + \psi_{L,k}(x)a_L^{\dagger}(x)\right)|\phi\rangle + \sum_{j=1}^{N} c_k^{(j)}\left|\phi_1^{(j)}\right\rangle\right]. \tag{3.1}$$

Derivation for arbitrary N: Assuming that the photon is incident from the left, the explicit

forms for $\psi_{L,k}(x)$ and $\psi_{R,k}(x)$ can be worked out, subject to appropriate continuity relations at the boundaries. These solutions turn out to be plane waves. Substituting them into the Schrödinger equation $(\mathcal{H}-\hbar\omega_k)\,|k^+\rangle = 0$, one is led to a system of coupled equations involving the transmission and reflection coefficients. This leads to a recursive matrix relation

$$\begin{bmatrix} r_j \\ t_{j-1} \end{bmatrix} = \begin{bmatrix} e^{ikL}(1-i\delta_k^{-1}) & -ie^{-ikL}\delta_k^{-1} \\ ie^{ikL}\delta_k^{-1} & e^{-ikL}(1+i\delta_k^{-1}) \end{bmatrix} \begin{bmatrix} r_{j+1} \\ t_j \end{bmatrix}, \tag{3.2}$$

where $\Gamma = \dfrac{\mathcal{J}^2}{v_g}$ and $\delta_k = \dfrac{\Delta_k}{\Gamma}$. From this, we identify a transfer matrix

$$\mathcal{L} = \begin{bmatrix} e^{ikL}(1-i\delta_k^{-1}) & -ie^{-ikL}\delta_k^{-1} \\ ie^{ikL}\delta_k^{-1} & e^{-ikL}(1+i\delta_k^{-1}) \end{bmatrix}. \tag{3.3}$$

Upon using Eq. (3.2) iteratively N times in succession, we find a simultaneous equation involving r and t:

$$\begin{bmatrix} r \\ 1 \end{bmatrix} = \mathcal{L}^N \begin{bmatrix} 0 \\ te^{ikNL} \end{bmatrix}. \tag{3.4}$$

It follows that in order to extract the analytical expressions for r and t, one needs to evaluate the N^{th} power of the 2×2 matrix $\mathcal{L}$. To that end, one can invoke a well-known and straightforward technique as follows: consider the diagonal form of $\mathcal{L}$, say $\mathcal{D} = U^{-1}\mathcal{L}U$, where U is the diagonalizing transformation, and then raise the inverse relation to its N^{th} power to get $\mathcal{L}^N = U\mathcal{D}^N U^{-1}$. A simple eigenvalue analysis yields the diagonal form of $\mathcal{L}$ to be

$$\mathcal{D} = \begin{bmatrix} e^{\Lambda} & 0 \\ 0 & e^{-\Lambda} \end{bmatrix}, \tag{3.5}$$

where the auxiliary parameter Λ is related to δ_k and kL as

$$\cosh(\Lambda) = \cos(kL) + \delta_k^{-1} \sin(kL). \tag{3.6}$$

Using the above definition, it becomes convenient to work out compact expressions for the reflection and transmission coefficients:

$$\begin{aligned} r &= \frac{(\mathcal{L}^N)_{12}}{(\mathcal{L}^N)_{22}} = -ie^{-ikL}\left[\frac{\mu_N(\Lambda)}{\Omega_N(\delta_k,\Lambda)}\right], \\ t &= \frac{e^{-ikNL}}{(\mathcal{L}^N)_{22}} = e^{-ikNL}\left[\frac{\delta_k}{\Omega_N(\delta_k,\Lambda)}\right], \end{aligned} \tag{3.7}$$

where the functions μ_N and Ω_N are defined respectively as

$$\mu_N(\Lambda) \coloneqq \frac{\sinh(N\Lambda)}{\sinh(\Lambda)}, \qquad \Omega_N(\delta_k,\Lambda) \coloneqq \delta_k \cosh(N\Lambda) - i\mu_N(\Lambda)\zeta(\delta_k, kL), \tag{3.8}$$

with $\zeta(\delta_k, kL) = \delta_k \sin(kL) - \cos(kL)$. This completes our derivation of the transmission and reflection coefficients for a chain of identical atoms.

On the conservation of energy: It is useful to note that Λ, defined as a solution to Eq. (3.6), can be generally complex. Since the RHS of (3.6) happens to be real, $\cosh(\Lambda)$ would be constrained to assume all real values between $-\infty$ and $+\infty$. When the value of this function exceeds unity, Λ has a real solution. In the range $-1 \leq \cosh(\Lambda) \leq 1$, Λ can be described by purely imaginary values, as changing $\Lambda \to i\Lambda$ turns the function into $\cos(\Lambda)$. For $\cosh(\Lambda) < -1$, the solutions to Λ are neither real nor purely imaginary. Nevertheless, one can establish a one-to-one correspondence between the solutions of $\cosh(\Lambda) < 0$ and those of $\cosh(\Lambda) > 0$. Observe that $\cosh(\Lambda)$ flips signature when we let $\Lambda \to i\pi \pm \Lambda$, and consequently, for any real $\Lambda = \Lambda_0$ satisfying $\cosh(\Lambda_0) > 1$, we find that $\tilde{\Lambda}_0^{\pm} = i\pi \pm \Lambda_0$ satisfy $\cosh\left(\tilde{\Lambda}_0^{\pm}\right) = -\cosh(\Lambda_0) < -1$. Now essentially, both the transformation schemes $\Lambda \to i\Lambda$ and $\Lambda \to i\pi \pm \Lambda$ ensure that $\cosh(N\Lambda)$ and $\mu_N(\Lambda)$ continue to assume real values, provided Λ is originally chosen to be real. Furthermore, it can be verified that

$\zeta^2 = 1 - \delta_k^2 \sinh^2(\Lambda)$. Considering all these subtleties, we conclude that $|\Omega_N|^2 = \delta_k^2 + \mu_N^2$, whence we compute, quite generically, the expressions for $\mathcal{R} = |r|^2$ and $\mathcal{T} = |t|^2$:

$$\mathcal{R} = \frac{\mu_N^2(\Lambda)}{\delta_k^2 + \mu_N^2(\Lambda)}, \quad \mathcal{T} = \frac{\delta_k^2}{\delta_k^2 + \mu_N^2(\Lambda)}. \tag{3.9}$$

This satisfies $\mathcal{R} + \mathcal{T} = 1$ as radiative decays have been ignored in the current model. It should also be borne in mind that Eqs. (3.7) and (3.9) do not showcase the explicit dependence of the amplitudes and intensities on the dimensionless detuning parameter $\delta_k = \dfrac{\Delta_k}{\Gamma}$. This is because Λ itself is determined by δ_k.

3.2 Emergence of Fano interference minima

From Eq. (3.7), we can identify the roots or zeros of the reflection, which would correspond to the points of Fano minima and determine the peaks in the transmission spectrum. The appropriate values of the detuning Δ_k at which the system becomes transparent are obtained by solving the equation

$$\mu_N(\Lambda) = 0 \tag{3.10}$$

This leads to exactly $(N-1)$ simpler root equations, each of which may be expected to yield a solution. Of course, it might turn out that for certain choices of kL and/or N, some of these equations either make no sense or do not provide finite solutions. In what follows, we briefly review the known results for $N = 1$ and $N = 2$ and then proceed to obtain the roots for a general value of N.

Comparison between single-atom and two-atom settings: For a single emitter coupled to the waveguide, r reduces to an extremely simple form, as can be seen by plugging $N = 1$ and $kL = 0$

into Eq. (3.7):

$$r^{(1)} = -\frac{1}{1 - \dfrac{i\Delta_k}{\Gamma}}. \tag{3.11}$$

In compliance with previously known results, this function has no roots. In fact, the spectrum $\mathcal{R} = \left|r^{(1)}\right|^2 = \dfrac{1}{1 + \dfrac{\Delta_k^2}{\Gamma^2}}$ has a Lorentzian lineshape (Fig. 3.1) of width 2Γ and is symmetric in Δ_k with a peak at $\Delta_k = 0$. This is quite reasonable given that there are no interference channels for a single scatterer, which precludes the existence of a Fano minimum.

The double-emitter case is more interesting as it allows for multiple photon transport channels leading to the possibility of destructive interference between these channels. The reflection coefficient is now given by

$$r^{(2)} = -\frac{2ie^{ikL}[\sin(kL) + \frac{\Delta_k}{\Gamma}\cos(kL)]}{(\frac{\Delta_k}{\Gamma} + i)^2 + e^{2ikL}}. \tag{3.12}$$

The numerator goes to zero at $\Delta_k^{\text{r min}} = -\Gamma \tan(kL)$, which is a special case of the result obtained in Ref. [37] for symmetrical coupling between the emitters and the field in the absence of DDI. Thus, there exists a Fano minimum at this value of detuning which renders the system transparent. Further, the location of this root demonstrates the generally asymmetric nature of the spectrum, in contrast to the single-emitter scenario. Finally, it is crucial to draw attention to the fact that not for all values of kL are we guaranteed to observe a Fano minimum (see Fig. 3.1).

Extension to arbitrary number of emitters: solving Fano minima in general: For arbitrary N, one would expect the possibility of multiple minima in the reflection lineshape as the number of interference channels increases with the number of scatterers, since each of them contributes to the final reflected output. Indeed, when Eq. (3.10) is solved, it leads to $(N-1)$ simplified root equations pertaining to any value of N. Using the definition of hyperbolic sine function, i.e.

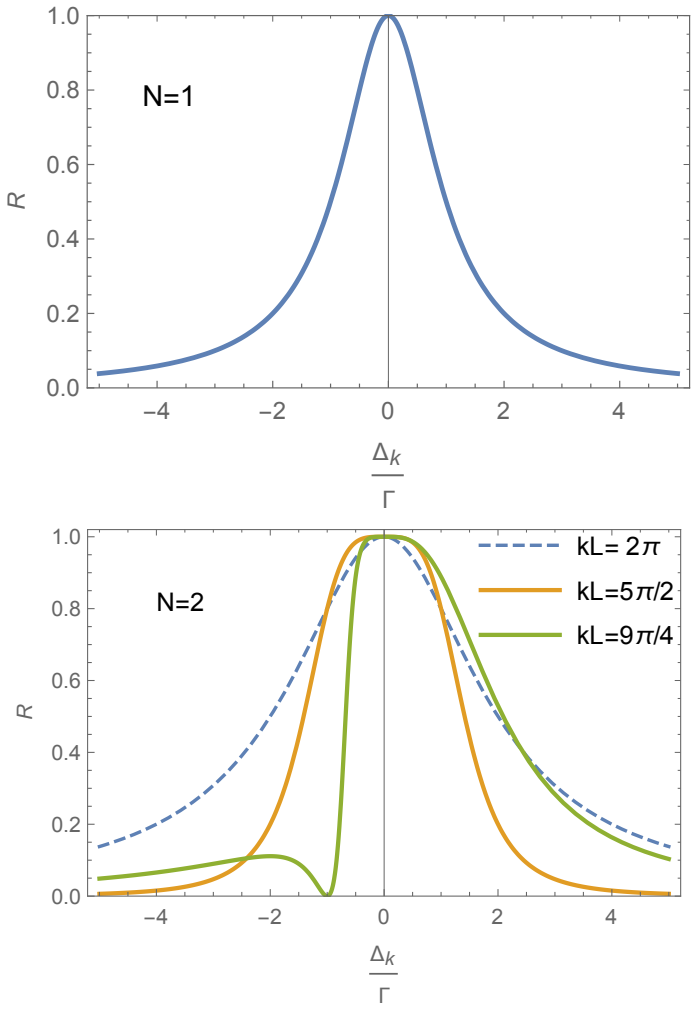

Figure 3.1: Plots of $\mathcal{R} = |r|^2$ vs $\dfrac{\Delta_k}{\Gamma}$ for $N = 1$ and $N = 2$ respectively. The spectrum for $N = 1$ is symmetric with no Fano minimum. For $N = 2$, the choice of kL, or equivalently $\frac{L}{\lambda}$, heavily influences the spectral characteristics, including the existence of a Fano minimum.

$\sinh(x) = \dfrac{e^{2x} - 1}{2e^x}$, it is possible to express the function μ_N as

$$\mu_N(\Lambda) = \frac{1}{e^{(N-1)\Lambda}} \prod_{l=1}^{N-1} (e^{2\Lambda} - e^{2il\pi/N}). \tag{3.13}$$

Setting this equal to zero, one finds that the Fano minima occur at purely imaginary values of the

quantity Λ

$$\Lambda_l^{\text{r min}} = \frac{il\pi}{N}, \quad \text{for } l = 1, 2, ..., N-1, \tag{3.14}$$

which, when combined with Eq. (3.6), yields

$$\begin{aligned} \cos(kL) + \frac{\Gamma}{\Delta_k}\sin(kL) &= \cos\left(\frac{l\pi}{N}\right); \\ \implies \Delta_k^{\text{r min}} &= -\frac{\Gamma\tan(kL)}{1-\cos\left(\frac{l\pi}{N}\right)\sec(kL)}, \\ &\text{for } l = 1, 2, ..., N-1. \end{aligned} \tag{3.15}$$

For N=1, Eq. (3.15) provides no roots, while for $N = 2$, there is a single equation corresponding to $l = 1$, which reduces to $\Delta_k^{\text{r min}} = -\Gamma\tan(kL)$, in agreement with the result obtained earlier. It makes for a relevant observation in this context that for $N = 2$ and $kL = \frac{n\pi}{2}$, with odd n, $\Delta_k^{\text{r min}}$ blows up and therefore, no finite solution exists. In fact, for any even N, the root equation stipulated by the choice $l = \frac{N}{2}$ does not lead to a finite solution. Similarly, in the instance when $kL = n\pi$, there exists no finite solution for any N, as can be figured out from the more fundamental equation (3.15). Therefore, the spectral properties and the existence of well-defined transmission peaks are heavily reliant on the size of emitter-spacing relative to the resonant wavelength $\lambda = \frac{2\pi}{k}$. This also explains the absence of Fano minima in Fig. 3.1 for $N = 2$ and $kL = 2\pi, \dfrac{5\pi}{2}$.

In Fig. 3.2, we plot the spectra for a couple of higher values of N ($= 3, 4$), each subject to three distinct choices of kL. The plots clearly illustrate how the choice of phase plays a pivotal role in determining the symmetric or asymmetric nature of the spectrum. The spectra also reveal how the precise choice of kL dictates the feasibility of observing as many Fano minima as the number of root equations in 3.15. For instance, in the case $kL = \frac{7\pi}{3}$ with three emitters, a single Fano minimum is observed, while for the choice $kL = \frac{5\pi}{2}$, two symmetric points of minima appear.

As a direct consequence of the existence of multiple Fano minima, one can notice the emergence of multiple shorter sidebands in the reflection spectrum. It makes for a more intriguing

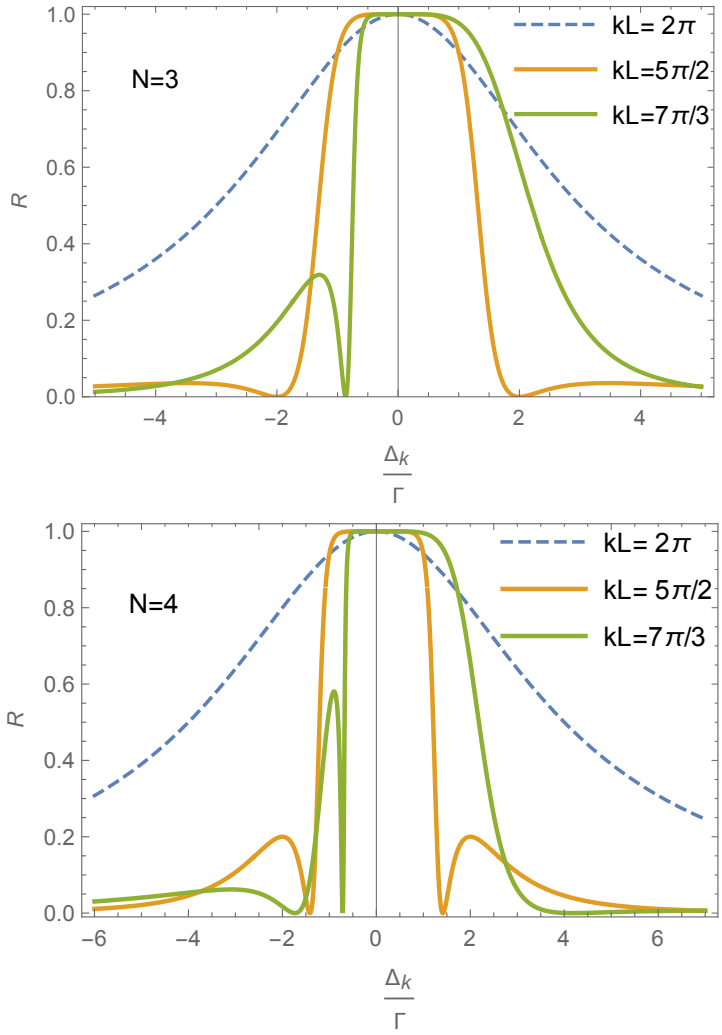

Figure 3.2: Spectral characteristics for $N = 3$ and $N = 4$ respectively. As expected, the value of kL fundamentally impacts the nature of the graphs and therefore, the existence of Fano minima. For $N = 3$, the number of observed roots vary between none to at most 2, while for $N = 4$, there can be at most 3 roots. Higher number of scatterers lead to higher number of interference channels and hence, to the possibility of a greater number of roots. It can also be observed that in the cases $kL = \frac{5\pi}{2}$ and $kL = \frac{7\pi}{3}$, the lineshapes become very flat near the origin giving rise to broadband characteristics.

observation that some of the lineshapes corresponding to $N = 2, 3$ and 4 (Figs. 3.1 and 3.2) are almost flat near resonance, thereby exhibiting the characteristic feature of a broadband spectrum. This broadband region signifies an opacity window because transmission is almost entirely blocked out. It turns out that this flatness in the highly reflecting domain is quite a generic feature for the

case of multiple emitters, which holds as long as kL does not get too close to an integral multiple of π. This statement will be analytically justified in the next section. Finally, Eq. (3.15) also shows that for arbitrarily large values of N, the roots corresponding to $l \ll N$ and $l \sim N$ evolve into sets of continuum leading to the formation of broadband regions of high transmittance.

Explanation of Fano Interference: The root cause behind the appearance of asymmetric lineshapes and corresponding minima in the spectra can be attributed to the Fano effect. Fano profiles are generally asymmetric in nature, as we have seen in many of the plots, and stem from the interference between various scattering amplitudes generated due to photonic interaction with the scatterers. Compactly described, the photon in the waveguide can be absorbed and emitted by any one of the atoms, and as such, there exists a number of such possible channels determined by the number of scattering agents. Since, quantum mechanically, all these processes have finite probabilities, the net effect is an interference between all these transition amplitudes. In particular, destructive interference between the scattering amplitudes leads to suppression of the reflected amplitude and one can encounter a zero (or, more generally, a minimum) in the corresponding profile. The atomic separation can be seen to play a vital role in giving rise to these Fano profiles and multiple points of transparency. In Ref. [37], it was explained how the phase factor e^{ikL}, brought about due to the propagation of light from one emitter to the next, was crucial in introducing asymmetry in the lineshapes. More precisely, it was interpreted as being a key contributor to waveguide-mediated interaction between the emitters existing even in the absence of the actual DDI.

3.3 Flatbanded spectral character: an effect of periodicity

In the vicinity of $\delta_k = \dfrac{\Delta_k}{\Gamma} \sim 0$, under the assumption $kL \neq n\pi$, we have the asymptotic behavior $\cosh(\Lambda) \sim \delta_k^{-1} \sin kL$, $\sinh(\Lambda) \sim \delta_k^{-1} \sin kL$ and $e^{\Lambda} \sim 2\delta_k^{-1} \sin kL$. On account of these

considerations, we obtain the asymptotic form of the function μ_N to be

$$\mu_N(\Lambda) \sim \{2\delta_k^{-1} \sin kL\}^{N-1} \left[1 - \left\{\frac{\delta_k}{2 \sin kL}\right\}^{2N}\right]. \tag{3.16}$$

Substituting this expression into Eq. (3.7), one obtains the behavior of the lineshape near zero detuning:

$$\mathcal{R}(\delta_k)\Big|_{\delta_k \sim 0} \approx 1 - 4 \sin^2 kL \left[\frac{\delta_k}{2 \sin kL}\right]^{2N} + \mathcal{O}\left[\frac{\delta_k}{2 \sin kL}\right]^{4N}. \tag{3.17}$$

Hence, viewed as a Taylor series expansion in $\delta_k/(2 \sin kL)$ around the origin, this manifests a couple of features: (i) $\mathcal{R} \to 1$ as $\delta_k \to 0$, and (ii) the leading order non-vanishing derivative of R w.r.t δ_k at the origin is $\mathcal{R}^{(2N)}(\delta_k)$. The first feature testifies to the validity of a well-known result in literature that the zero-detuned case corresponds to perfect reflection with zero transmission. This fact holds true for arbitrary chain size.

The second feature is a direct algebraic manifestation of spectral flatness in the region near zero detuning, applicable to all $N \geq 2$. In order to exemplify this point, we can consider the case for $N = 2$, where the leading-order expansion of $\mathcal{R}(\delta_k)$ goes as $1 - \dfrac{\delta_k^4}{4 \sin^2 kL} \approx \exp\left[-\dfrac{{\delta_k}^4}{4 \sin^2 kL}\right]$ and therefore, possesses super-Gaussian characteristics. This is in contrast to the Lorentzian nature of the lineshape for $N = 1$ (see Eq. (3.11)), which resembles a Gaussian distribution in the vicinity of zero detuning. In fact, whenever N exceeds 1, the order of the lowest non-vanishing derivative at the origin exceeds two, since $\mathcal{R}(\delta_k)$ behaves approximately as $\exp\left[-\dfrac{{\delta_k}^{2N}}{\{2 \sin kL\}^{2N-2}}\right]$. The essential implication is that the function varies rather slowly in relation to a Gaussian, leading to the emergence of an almost horizontal plateau-top near the origin. Consequently, lineshapes pertaining to multiple emitters are significantly flatter than what is realized in the single-emitter setting and quite generically display broadband characteristics. Moreover, at the qualitative level, the existence of this property is insensitive to the choice of kL, barring $kL = n\pi$ when the emitter-

spacing is an integral or half-integral multiple of the resonant wavelength. More interestingly, since the super-Gaussian characteristics get progressively amplified with the increase in N, an emitter chain of large size ($N \gg 1$) is capable of fabricating a broadband rectangular profile over the frequency domain. One can discern its validity by considering the graphs of $e^{-x^{2N}}$ or $(1 - x^{2N})$ for increasingly larger values of N.

The order of the super-Gaussian distribution scales linearly as N and therefore, for a given kL, both the flatness and the frequency bandwidth grow with N. In the limit $N \to \infty$, the bandwidth approaches $\sim 3.4\Gamma \sin(kL)$. We, therefore, observe the emergence of a band gap of finite width in an infinitely long chain, which can be reconciled with the formation of band structures in crystalline geometries. In periodic systems of infinite size, the discrete translational symmetry leads to band formation as a direct consequence of Bloch's theorem. Note that the flatbanded character becomes particularly prominent as kL moves further and further away from any integral multiple of π, with the bandwidth peaking at $kL = \dfrac{n\pi}{2}$. In what follows next, we treat the case $kL = n\pi$ separately and reveal a Lorentzian superradiant character of the spectrum at this phase.

3.4 Symmetrical Lineshapes w.r.t qubit detunings for special choices of phase-coupling

The reflection spectra for $N > 1$ are endowed with certain interesting features, some of which are quite generic while some pertain to particular categories of choices for kL. In this section, we analytically uphold the symmetric nature of the output spectra, subject to suitable choices of kL. It follows from Eq. (3.9) that the reflection and transmission spectra can be symmetric in δ_k if and only if the function $\mu_N(\Lambda)$ is either even or odd under a sign flip in δ_k. Specifically, this condition is always satisfied when kL equals any integral or half-integral multiple of π.

Dicke Superradiant character of reflection for $kL = n\pi$: This corresponds to $L = \dfrac{n\lambda}{2}$, where n can assume both even and odd values. It is easy to see that the Taylor series expansion laid out in Sec. 3.3 does not hold good for this particular choice of kL. This stems from the fact that $\cosh(\Lambda)$ and $\sinh(\Lambda)$ are identically equal to $(-1)^n$ and 0 respectively. Consequently, Λ equals 0 when n

is even and $i\pi$ when n is odd, making the variable independent of δ_k. Hence μ_N remains invariant under the transformation $\delta_k \to -\delta_k$. In fact, we can plug in the values of Λ to obtain an expression for $\mathcal{R}$ as an explicit function of $\dfrac{\Delta_k}{\Gamma}$. To that end, we employ the relation

$$\mu_N(\Lambda) = \sum_{m\to\text{odd}}^{N} \binom{N}{m} \cosh^{N-m}(\Lambda) \sinh^{m-1}(\Lambda), \tag{3.18}$$

which yields

$$\lim_{kL\to n\pi} \mu_N(\Lambda) = (-1)^{n(N-1)} N, \tag{3.19}$$

and immediately determines a Lorentzian lineshape for the reflection spectrum:

$$\mathcal{R} = \frac{1}{1 + \dfrac{\Delta_k^2}{N^2\Gamma^2}}. \tag{3.20}$$

This generalization also encompasses the case $N = 1$. Thus, the spectrum for $kL = n\pi$, which pins down a real phase $e^{ikL} = (-1)^n$, is perfectly symmetric in the detuning and has a Dicke-type super-radiant structure. Viewed as a function of Δ_k, the spectrum has a width that scales linearly as the size of the chain and equals $2N\Gamma$. It is also bereft of a Fano minimum, which is in line with the prediction made by Eq. (3.15) for $kL = n\pi$.

Non-Lorentzian symmetry for the $kL = \dfrac{n\pi}{2}$ spectral family ($n \to$ odd): For even values of n, the spectrum possesses Lorentzian symmetry, as we have obtained in the preceding subsection. For odd n, we have $\cos(kL) = 0$ which leads to $\cosh(\Lambda) = (-1)^{(n-1)/2}\delta_k^{-1}$. Under a parity transformation in δ_k, $\cosh(\Lambda)$ flips signature, which, as we saw in Sec. 3.1, can be embodied as the transformation scheme $\Lambda \to i\pi \pm \Lambda$. In this process, $\mu_N(\Lambda)$ acquires a real phase given by $(\mp 1)^{N-1}$. Invoking these transformation properties in Eq. (3.7), it becomes apparent that $\mathcal{R}$ is indeed an even function of δ_k, whenever kL is chosen to be an half-integral multiple of π. This

property makes for an interesting observation, since, even though one observes Fano minima, the lineshapes exhibit perfect symmetry.

3.5 Effect of the variation of Δ_k with kL

So far, everything has been discussed under the assumption that kL can be treated as a constant, considering its weak variation w.r.t. $\dfrac{\Delta_k}{\Gamma}$. However, it should be noted that kL has a one-to-one correspondence with Δ_k. As a consequence, contingent on the strength of their interdependence, one can possibly encounter multiple observable roots for a given choice of l in Eq. (3.15). Recall that $\Delta_k = v_g k - \omega_0$ and therefore, one has the relation

$$kL = k_0 L\left[1 + \frac{\eta\Delta_k}{\Gamma}\right], \tag{3.21}$$

where $k_0 = \dfrac{\omega_0}{v_g}$, $\eta = \dfrac{\Gamma}{\omega_0}$. Hence, kL depends linearly on Δ_k, and a specified choice of kL ideally pins down a unique value of Δ_k. That said, in most practical experiments, the value of η tends to be quite small, i.e. $\eta \ll 1$. For instance, in the case of cold atoms coupled to an optical fiber, the resonance frequency lies in the optical THz domain, while the coupling constant Γ lies in the GHz regime. Besides, since one is concerned with waveguide frequencies in the vicinity of the atomic transition frequency, i.e. $\dfrac{\Delta_k}{\Gamma} \approx 0$, one typically drops the correction term $\dfrac{\eta\Delta_k}{\Gamma}$ from Eq. (3.21) altogether and examines the spectral characteristics by treating kL as a constant ($kL \approx k_0 L$). This assumption has been a cornerstone for the Markovian approximation, and is especially relevant in the framework of RWA. In Fig. 3.3, we graph the exact spectrum for $N = 2$ and $k_0 L = \dfrac{5\pi}{2}$ by including the correction term $\dfrac{\eta\Delta_k}{\Gamma}$ in Eq. (3.21) and illustrate what modification it brings about for the following ballpark order-of-magnitude choices of η: (i) $\eta \sim 0$, (ii) $\eta \sim 10^{-3}$, (iii) $\eta \sim 10^{-2}$ and (iv) $\eta \sim 10^{-1}$. For the sake of comparison, these plots are superimposed on top of each other. Expectedly, case (ii) yields an almost identical spectrum to (i). Case (iii) reveals a slight narrowing of the lineshape, whereas case (iv) shows considerable shrinking in its width. Even more curiously, one happens to observe new points of Fano minima in (iii) and (iv) which did not exist in

the approximate spectrum where η was small enough to be ignored. Moreover, even though there is only a single value of l in Eqs. (3.15) for the case of two symmetrical emitters, there happens to be two distinct values of the detuning in case (iv) for which the reflection vanishes. This is because the condition for Fano minima is transformed into a transcendental equation when Γ becomes very large.

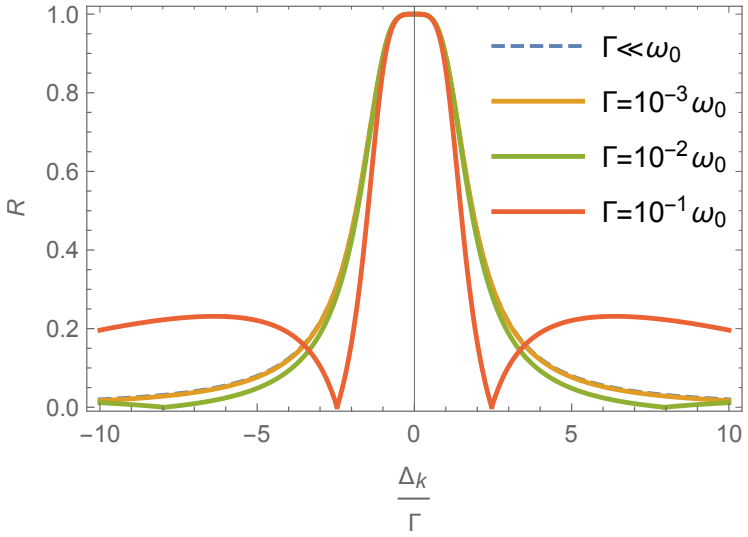

Figure 3.3: Reflection lineshapes for two quantum emitters with (i) $\Gamma \ll \omega_0$ (no correction term), (ii) $\Gamma = 10^{-3}\omega_0$, (iii) $\Gamma = 10^{-2}\omega_0$ and (iii) $\Gamma = 10^{-1}\omega_0$. Cases (i) and (ii) are indistinguishable whereas cases (iii) and (iv) reveal noticeable aberrations from case (i). Specifically, one can observe a couple of symmetric zeros in their reflection spectra. In (iv), these zeros appear at $\left|\Delta_k^{\mathrm{r\,min}}\right| \approx 2.2\Gamma$. All of these plots correspond to $k_0 L = \frac{5\pi}{2}$.

3.6 Lattice disorder: localization uncertainty

There are obvious experimental challenges to fix the lattice length (atomic separation) to arbitrary degree of precision. Consequently, given that we are working in the nanoscale regime, the spatial separation between neighbouring emitters should possess an experimental uncertainty. To get a better estimate of the reflected output, we should, therefore, view the separation as a stochastic variable and consider an average of the intensity over the associated probability distribution in the empirical model. Let us consider the simplest case of two atoms with separation L and define

the random variable $\theta \equiv kL = \theta_0 + \epsilon$, where ϵ signifies fluctuation of the parameter kL about θ_0. We can model the fluctuation by assigning a Gaussian probability distribution, as follows:

$$\rho(\theta) = \frac{1}{\sqrt{2\pi}\sigma} \exp\left[-\frac{(\theta - \theta_0)^2}{2\sigma^2} \right]. \tag{3.22}$$

In the absence of any fluctuation in θ, we have the following reflection output (see Eq. 3.12):

$$\mathcal{R}^{(2)}(\theta) = \left| r^{(2)}(\theta) \right|^2 = \frac{(\sin\theta + \delta_k \cos\theta)^2}{(\delta_k^2 - 1 + \cos 2\theta)^2 + (2\delta_k + \sin 2\theta)^2}. \tag{3.23}$$

Hence, the averaged output will be obtained as:

$$\overline{\mathcal{R}^{(2)}(\delta_k)} = \int_0^\infty \mathrm{d}\theta\, \rho(\theta) \mathcal{R}^{(2)}(\theta). \tag{3.24}$$

In Fig. 3.4, we plot the reflected intensity $\overline{\mathcal{R}^{(2)}(\delta_k)}$ averaged w.r.t the aforementioned Gaussian distribution with mean $\theta_0 = \frac{\pi}{4}$ and standard deviations $\sigma = 0.1\theta_0$ and $\sigma = 0.25\theta_0$. We observe that for $\sigma = 0.1\theta_0$, the spectrum closely resembles the non-fluctuating case and at the Fano minimum, the reflected intensity is quite close to zero. The observed spectrum for $\sigma = 0.25\theta_0$ is more interesting in the context of our investigation. In this case, the Fano minimum is clearly affected and becomes almost unnoticeable. However, the rest of the graph is barely affected. Essentially what this demonstrates is that the existence of a Fano minimum is largely sensitive to fluctuations in the atomic spacing.

3.7 Inclusion of atomic couplings to the side modes

In our analytical treatment, we have conveniently neglected radiative decays into all modes outside the propagating modes of the 1D waveguide. However, in real experiments, spontaneous emissions into these 'outsider' modes will always be present. In light of such considerations, one could be prompted to question the relevance of our results that neglect these losses. Hereby, we put to rest such doubts through a re-evaluation of the problem by accounting for radiative decays. We

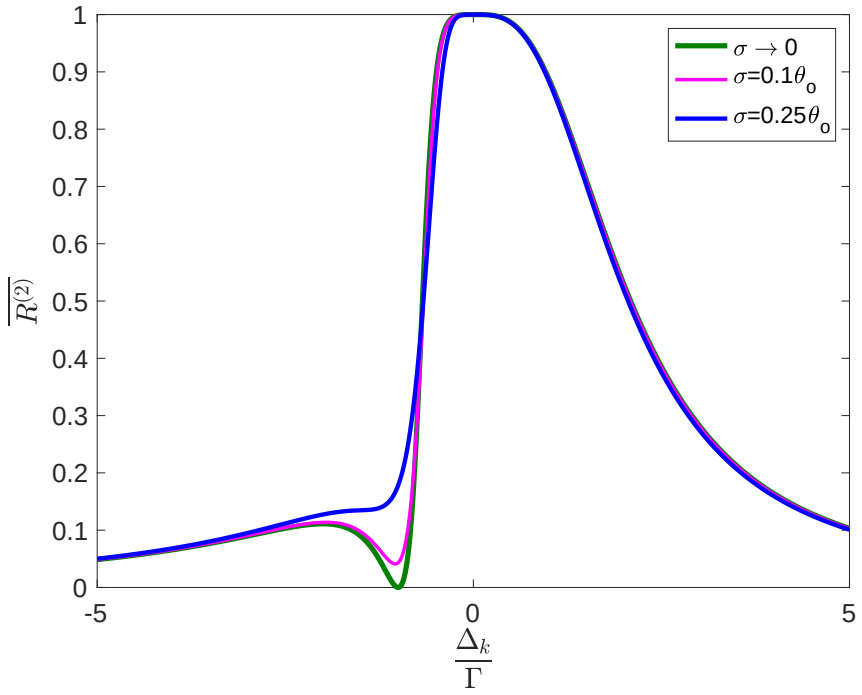

Figure 3.4: Plots of $\overline{\mathcal{R}^{(2)}}$ vs $\dfrac{\Delta_k}{\Gamma}$ for $\theta_0 = \frac{\pi}{4}$ and different choices of σ. The dashed line indicates the spectrum corresponding to zero fluctuation in the atomic separation, i.e. when the Gaussian takes the form of a Dirac-delta function.

demonstrate that if this decay rate is small compared to the parameter $\Gamma = \dfrac{\mathcal{J}^2}{v_g}$, the spectral nature does not exhibit appreciable variation. The decay rate will be reflected in the Hamiltonian of the atom and can be given substance to by augmenting an anti-Hermitian contribution to the atomic Hamiltonian, as follows:

$$\tilde{\mathcal{H}}_A = \hbar(\omega_0 - i\Gamma_0) \sum_{i=1}^{N} |e\rangle_j \langle e| \,, \tag{3.25}$$

The presence of additional decay channels incorporates an imaginary offset to the real atomic transition frequency in the quantum description of the transport model, i.e., $\omega_0 \to \tilde{\omega}_0 = \omega_0 - i\Gamma_0$. Consequently, the quantities Δ_k and δ_k will turn into complex parameters $\tilde{\Delta}_k = \Delta_k + i\Gamma_0$ and $\tilde{\delta}_k = \delta_k + i\gamma_0$ respectively, with $\gamma_0 = \dfrac{\Gamma_0}{\Gamma}$. On account of the modified complex nature of $\tilde{\delta}_k$, one

would have to redefine a new parameter $\tilde{\Lambda}$ in place of Λ satisfying

$$\cosh\left(\tilde{\Lambda}\right) \equiv \cos(kL) + \tilde{\delta}_k^{-1} \sin(kL). \tag{3.26}$$

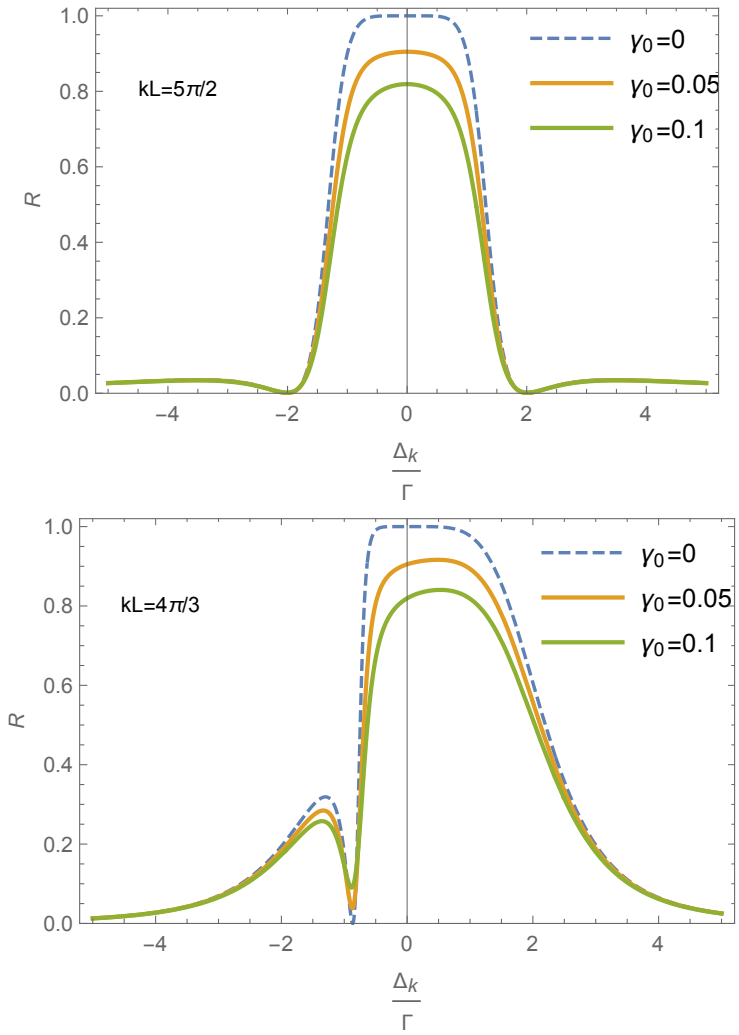

Figure 3.5: Plots of $\mathcal{R} = |r|^2$ vs $\dfrac{\Delta_k}{\Gamma}$ for $N = 3$ corresponding to two distinct choices of phase. The presence of decay barely changes the nature of the graphs. The Fano minima remain almost unaltered, although the flat-banded characteristic suffers a decline as the dissipation increases.

It is clear that $\cosh\left(\tilde{\Lambda}\right)$ is no longer constrained to be real, and it can be shown that $R+T < 1$. Thus, the new parameter $\tilde{\Lambda}$ not only depends on the detuning but is also sensitive to the decay rate.

Hence, the analytical results have to generalized by letting $\delta_k \to \tilde{\delta}_k$:

$$r = -ie^{-ikL}\left[\frac{\mu_N(\tilde{\Lambda})}{\Omega_N(\tilde{\delta}_k, \tilde{\Lambda})}\right], \quad t = e^{-ikNL}\left[\frac{\tilde{\delta}_k}{\Omega_N(\tilde{\delta}_k, \tilde{\Lambda})}\right], \tag{3.27}$$

where $\mu_N(\tilde{\Lambda}) = \sinh\Big(N\tilde{\Lambda}\Big)\sinh\Big(\tilde{\Lambda}\Big)$ and $\Omega_N(\tilde{\delta}_k, \tilde{\Lambda}) \equiv \tilde{\delta}_k \cosh\Big(N\tilde{\Lambda}\Big) - i\mu_N(\tilde{\Lambda})\zeta(\tilde{\delta}_k, kL)$, with $\zeta(\tilde{\delta}_k, kL) = \tilde{\delta}_k \sin(kL) - \cos(kL)$. As $\tilde{\delta}_k$ is now complex, all of $\mu_N(\tilde{\Lambda})$, $\cosh\Big(N\tilde{\Lambda}\Big)$ and $\zeta(\tilde{\delta}_k, kL)$ will also be complex. Hence, the expressions for $\mathcal{R} = |r|^2$ and $\mathcal{T} = |t|^2$ turn out to be more complicated, as follows:

$$\mathcal{R} = \frac{|\mu_N|^2}{\xi\{\delta_k^2 + \gamma_0^2\} + |\mu_N|^2 + 2\,\mathrm{Im}\{\mu_N \zeta \cosh^*(N\tilde{\Lambda})(\delta_k - i\gamma_0)\}}, \tag{3.28}$$

$$\mathcal{T} = \frac{\delta_k^2 + \gamma_0^2}{\xi\{\delta_k^2 + \gamma_0^2\} + |\mu_N|^2 + 2\,\mathrm{Im}\{\mu_N \zeta \cosh^*(N\tilde{\Lambda})(\delta_k - i\gamma_0)\}}. \tag{3.29}$$

where we introduced the function ξ, defined below:

$$\xi(\tilde{\Lambda}) \equiv 2 - \frac{\left|\cosh\Big(\tilde{\Lambda}\Big)\right|^2 - 1}{\left|\sinh\Big(\tilde{\Lambda}\Big)\right|^2}. \tag{3.30}$$

Note that in the limit $\gamma_0 \to 0$, ξ approaches unity and Eqs. (3.28) and (3.29) go over into Eqs. (3.7) and (3.9).

From the modified expression for $\mathcal{R}$, it follows that zero-reflection points do not exist anymore. This is because the root equation $\mu_N = 0$ yields purely imaginary values of $\tilde{\Lambda}$ which imposes the restriction $\mathrm{Im}\{\cosh\Big(\tilde{\Lambda}\Big)\} = 0$, or $\gamma_0 = 0$. However, if we plot the reflection spectrum for $N = 3$ with the choices $\gamma_0 = 0.1$ and $\gamma_0 = 0.05$, we find that the fundamental nature of the graphs remain fairly unaffected (see Fig. 3.5). We still get Fano minima (suppression of the reflection amplitude) in the close vicinity of the original zero-reflection points. The flatbanded nature of the spectra gets more and more prominent as γ_0 diminishes in magnitude. This is obviously related to the fact that since the broadbanded structure appears in the proximity of zero detuning, i.e. $\mathrm{Re}\Big\{\tilde{\delta}_k\Big\} = \delta_k \sim 0$, unless the parameter $\mathrm{Im}\Big\{\tilde{\delta}_k\Big\} = \gamma_0$ is sufficiently small, appreciable deviations from flatband char-

acteristics would be noticed in this highly reflecting region.

3.8 Experimental Feasibility

All the results that have been derived in this chapter would allow experimental verification in a variety of models of topical interest. Some of these are resonators on a transmission line, laser-cooled atoms near a fiber and semiconducting QDs coupled to plasmonic excitations in a metallic or diamond nanowire, or to photonic crystal waveguides. Our theoretical results were, however, premised on loss-free or low-decoherence models. Therefore, it is desirable to contextualize the verification of these results in realistic empirical systems that allow adequate qubit-waveguide couplings, i.e. $\Gamma \gg \Gamma_0$. In that regard, superconducting circuit-QED models have marched way past all other systems, and would, consequently, be one of the prime candidates for realizing our predictions. In fact, except for QDs coupled to photonic crystals, almost none of the setups have come close to the staggering success rate of superconducting circuits.

Strong emission of single photons into a waveguide was first demonstrated in a circuit QED setting, with superconducting flux qubits playing the role of artificial atoms [82]. The experimenters were able to couple a flux qubit to an open microwave transmission line and observe a reflectance of about 94% at resonance, i.e., $\omega_{qubit} = \omega_{probe}$, which was a hallmark achievement. This observation was made at a very weak probe power, where a single-photon analysis would be more relevant, while at higher probe powers, saturation effects in the atom restored high transmittivity. The major advantage of these types of systems in achieving strong coupling is that superconductors can confine the electromagnetic fields to deeply subwavelength sizes in the transverse dimensions. In addition, transition dipoles of superconducting qubits are much larger than those of real atoms [92]. These systems work in the microwave regime, with frequencies around $5 - 12$ GHz, and the resonant qubit-transition is well below the superconducting energy gap Δ_{SC}. Such frequencies cannot induce transitions between the *superconducting energy levels*, as the corresponding transition frequencies are *strictly greater than the energy gap*. This is why superconductors incur little-to-no losses into side-modes and the coherence of the circuits is robustly protected. A necessary con-

cession is that these systems must be operated at cryogenic temperatures, typically below 50 mK, in order for the background thermal radiation to be sufficiently suppressed. However, superconducting systems suffer from *pure dephasing*, which can be significant and still low enough for our theoretical results to hold valid. In the resonance fluorescence experiment of Ref. [82], the resonance frequency of the artificial atom was reported as $\omega_{qubit} = 2\pi \times 10.204$ GHz, and the coupling strength Γ was inferred from experimental curve-fitting to be $2\pi \times 5.5$ MHz. While loss of emission into undesirable modes was negligible, they could identify a dephasing rate of $\Gamma_\phi = 2\pi \times 1.7$ MHz, which effectively plays the role of Γ_0 in our theoretical description. A subsequent experiment in 2011 using a superconducting transmon qubit achieved an even higher extinction rate, and a reflectance of nearly 99.6% was recorded by further alleviating the effects of decoherence due to both dephasing and relaxation into extrinsic channels [4]. Operating at the microwave resonance frequency of $\omega_{qubit} = 2\pi \times 6.38$ GHz, they achieved very strong coupling strength of $\Gamma = 2\pi \times 96$ MHz while simultaneously tamping down the dephasing rate to $\Gamma_\phi = 2\pi \times 2$ MHz. Going beyond a single qubit, Ref. [93] experimentally demonstrated collective decay rates, including both subradiance and superradiance, in a system of two spatially separated transmon qubits coupled to a 1D transmission line. The experiment clearly showcased a separation-sensitive exchange interaction between the atoms.

In parallel with superconducting circuitry, quantum dots coupled to surface plasmons and cold atoms trapped inside or near optical fibers have also largely led the way in the engineering of strongly integrated atom-waveguide architectures, due to their strong coherence properties. In 2014, researchers were able to manipulate and channel the emission of a quantum dot strongly into a photonic crystal waveguide, reporting 98.4% coupling efficiency to the transmission line [5]. The coupling efficiency is defined as $\beta = \dfrac{\Gamma}{\Gamma + \Gamma_0}$. Quite recently, a $\beta-$factor of 99% was reported at cryogenic temperature by Scarpelli *et al* [94]. Till date, superconducting microwave circuits and QD-based platforms have demonstrated the best performance metrics primed for the study of waveguide-controlled fluorescence phenomena. These are the two systems which could readily corroborate our theoretical predictions. On the cold-atom frontier, Bragg reflection off a

large chain of identical atoms trapped in an optical lattice in a waveguide was demonstrated by two experimental groups [64, 65]. However, these systems still pose a significant challenge in reducing the deleterious effects of decoherence. Typically, these platforms contain laser-cooled Cesium (Cs) or Rubidium (Rb) atoms trapped in the vicinity of an optical nanofiber. The associated $\beta-$factor remains quite low.

3.9 Summary

To put things into perspective, we have analytically investigated the Fano interference effect for single-photon transport through a one-dimensional waveguide that is evanescently coupled to a periodic array of two-level quantum emitters. The expression for the reflection amplitude reveals the existence of multiple Fano minima corresponding to induced transparency in the system. At any of the Fano minima, the atomic chain behaves effectively like a reflection-less potential. In the absence of DDI, waveguide-mediated phase-coupling between the atoms owing to their spatial separation acts as the driving agent behind the emergence of Fano profiles. Typically, for a chain size of N, the reflection amplitude can possess upto $(N-1)$ roots. However, appropriate choices of the phase e^{ikL} can lead to suppression of one or more of these roots. In fact, when kL is an integral multiple of π, the observed spectrum happens to be a Lorentzian which is devoid of any roots. The case when kL is a half-integral multiple of π also stands out, in the sense that it pertains to symmetrically located roots. With the exception of $kL \approx n\pi$, one observes flat-topped spectral lineshapes in the region of high reflectivity. Such characteristics are a manifestation of super-Gaussian signature, with both the flatness and the frequency bandwidth increasing with the chain size. In the limit of $N \to \infty$, the reflection spectrum resembles a rectangular profile with a width of $3.4\Gamma \sin(kL)$. We have also illustrated how strong enhancements in the atom-photon coupling strength can generate new points of Fano minima, which remain untapped in weaker coupling regimes where the *Markovian approximation* remains valid. In the non-Markovian regime, the condition for Fano minima evolves into a *transcendental* equation and requires numerical solutions. For the special case of $N = 2$, on choosing $\Gamma = 0.1\omega_0$, we observed the appearance of

two distinct Fano minima almost symmetrically situated w.r.t the common qubit detuning. Lastly, we have identified two main test beds for verifying our theoretical predictions, superconducting microwave circuits and QDs coupled to line defects in a photonic crystal waveguide.

4. TRANSPARENCY WITHOUT ANY CONTROL FIELD*

EIT is a well-known mechanism in quantum optics whereby a strong coherent field renders a system transparent to a probe field under appropriate conditions [95, 96]. The notion of EIT was originally envisaged in the context of a Λ-type three-level system. Conjoined with a weak optical probe field coupling to a selected transition, a strong control field was used to drive a *different transition* in the system. By regulating the frequency of the control field, the *complex susceptibility* (i.e., both its real and imaginary parts) of the *probe-coupled transition*, could be effectively suppressed. Owing to zero dispersion, the probe suffered no absorption in the medium and passed through the latter unimpeded. In the current chapter, we introduce a distinct protocol to implement transparency in an ensemble of *non-identical 2LAs*, *without applying any coherent coupling field*. This is based on our work in which we addressed the spectral properties of a periodic array of atoms, strongly coupled to a waveguide, with the periodicity being an *integer multiple of the resonant wavelength* [40]. Our key result was that the individual atomic detunings could be strategically adjusted to ensure destructive interference between the atomic emissions into the left-moving channel, allowing the input light to be fully transmitted. In other words, the interplay between atomic detunings effectively appropriated the role of a coupling field in inducing transparency in our system. The underlying mechanism, of course, is completely different.

As we had hinted in Chapter 2, the scattering eigenstate under the constraint $kL = n\pi$ could be exactly solved, even when the atomic frequencies were left different. The parity of the chain size, i.e., whether it is even or odd, was found to play a crucial role on the control of collective radiance. For even parity, we showcased a scheme to effect transparency by assigning equal and opposite pairwise detunings to the atoms. More generally, we derived the general condition for observing

*A major part of this chapter is reprinted with permission from *Transparency in a chain of disparate quantum emitters strongly coupled to a waveguide* by D. Mukhopadhyay and G. S. Agarwal, Phys. Rev. A **101**, 063814 (2020), published by the American Physical Society.

transparency in the system to be

$$\frac{1}{\Delta_k^{(1)}} + \frac{1}{\Delta_k^{(2)}} + \frac{1}{\Delta_k^{(3)}} + \ldots \frac{1}{\Delta_k^{(N)}} = 0, \tag{4.1}$$

where $\Delta_k^{(j)} = v_g k - \omega_j$ is the detuning of the jth atom. Our results are strong enough to withstand dissipative effects as long as the dissipative channel is weak compared to the waveguide channel and the atomic detunings are large compared to their decay rates. In the usual scenario for EIT, the system comprises noninteracting atoms, whereas in a waveguide, an effective phase coupling between the emitters persists even at long spatial separations (of the order of a wavelength). Furthermore, while reciprocity in single-photon transport does not generally hold due to the phase coupling, we observed an interesting exception for $kL = n\pi$ at which the waveguide demonstrates reciprocal behavior with regard to both the transmission and reflection coefficients.

The chapter is organized as follows. In Sec. 4.1, we solve single-photon transport through a waveguide coupled to two non-identical emitters. Such an arrangement allows nonreciprocal photon transport, which we will discuss in Sec. 4.2. In the special case $kL = n\pi$, the nonreciprocity disappears. In Sec. 4.3, we solve the system for an arbitrary number of non-identical emitters, deriving the condition under which transparent behavior unfolds. The analysis is simplified by the assumption $kL = n\pi$. In Sec. 4.4, we show numerical plots that testify to the robustness of the transparency condition to extraneous losses. The experimental feasibility of our theoretical model is discussed at length in Sec. 4.5. Finally, in Sec. 4.6, we draw some analogies with transparent behavior observed in a cavity-QED system with multiple atoms coupled to a single intracavity field mode. Section 4.7 summarizes the key ideas explored.

4.1 Solution for two non-identical 2LEs

In Chapter 2, Sec. 2.4, we had obtained the reflection and transmission coefficients across a general system of emitters as

$$r = \frac{\left(\prod_{j=1}^{N} \mathcal{L}_j\right)_{12}}{\left(\prod_{j=1}^{N} \mathcal{L}_j\right)_{22}}, \quad t = \frac{e^{-ikNL}}{\left(\prod_{j=1}^{N} \mathcal{L}_j\right)_{22}}. \tag{4.2}$$

where

$$\mathcal{L}_j = \begin{bmatrix} e^{ikL}(1 - i\delta_{k(j)}^{-1}) & -ie^{-ikL}\delta_{k(j)}^{-1} \\ ie^{ikL}\delta_{k(j)}^{-1} & e^{-ikL}(1 + i\delta_{k(j)}^{-1}) \end{bmatrix} \tag{4.3}$$

was the transfer matrix across the jth atom, with $\delta_{k(j)} = \dfrac{v_g k - \omega_j + i\Gamma_)^{(j)}}{\Gamma}$, $\Gamma = \dfrac{\mathcal{J}^2}{v_g}$. For notational convenience, we let $v_g k - \omega_j = \Delta_k^{(j)}$. Nevertheless, in order to avoid cumbersome notation, we suppress the $k-$ dependence and assume identical damping rates for the atomic systems. We, therefore, denote these variables as $\delta_j = \dfrac{v_g k - \omega_j + i\Gamma_0}{\Gamma}$ and $\delta_j = v_g k - \omega_j$. This convention would be retained throughout the rest of the chapter. Let us first consider the simpler scenario of two differentially detuned atoms in a waveguide and define the mean detuning of the incident photon $\overline{\Delta} = v_g k - \frac{1}{2}(\omega_1 + \omega_2)$ and relative atomic detuning $s = \omega_1 - \omega_2$.

Emergence of transparency: It turns out that while $(\mathcal{L}_1\mathcal{L}_2)_{22}$ is symmetric in s, $(\mathcal{L}_1\mathcal{L}_2)_{12}$ is not, owing to the phase coupling between the emitters mediated by the waveguide. In other words, in view of Eq. 4.2, even though transmission is perfectly reciprocal, reflection is not. For this system,

the reflection and transmission coefficients reduce to

$$r = \frac{-i\Gamma[(e^{i\alpha}+1)(\overline{\Delta}+i\Gamma_0)-(e^{i\alpha}-1)s/2]-\Gamma^2(e^{i\alpha}-1)}{[\overline{\Delta}+i(\Gamma+\Gamma_0)]^2+\Gamma^2e^{i\alpha}-(s/2)^2},$$
$$t = \frac{(\overline{\Delta}+i\Gamma_0+s/2)(\overline{\Delta}+i\Gamma_0-s/2)}{[\overline{\Delta}+i(\Gamma+\Gamma_0)]^2+\Gamma^2e^{i\alpha}-(s/2)^2}, \tag{4.4}$$

where we have taken $\alpha = 2kL$. We note, however, in the special case $kL = n\pi$, that the above expressions turn symmetric in s, thereby leading to reciprocity in the transport properties. In subsequent considerations, we analyse the results pertaining to this special choice of phase.

We now assume an idealized scenario where Γ_0 can be ignored. The effect of Γ_0 on the transmission is studied later in Sec. 4.4. With Γ_0 set to 0, one observes an emergence of transparent behavior when the two atoms are equally detuned, albeit in opposite directions, with respect to the laser frequency. In other words, t becomes unity when $\overline{\Delta}$ equals zero, or $\omega_k - \omega_1 = \omega_2 - \omega_k$, i.e. for a pair of antisymmetrically detuned emitters. It follows, from Eq. 4.4 and the plots in Fig. 4.1, that there is a transmission peak at $\overline{\Delta} = 0$, while there are two roots of the profile at $\overline{\Delta} = \frac{s}{2}$ (or $v_g k = \omega_1$) and $\overline{\Delta} = -\frac{s}{2}$ (or $v_g k = \omega_2$) corresponding to perfect reflection. The peak has unit height in the absence of decay, signifiying transparent behavior. The height of this peak is strictly less than unity for any other choice of phase, as can be verified from 4.4 (for instance, in the specific scenario, when $kL = \frac{n\pi}{2}$ with odd n, the height of this peak is $\left[\frac{s^2}{s^2+8\Gamma^2}\right]^2$ – see Fig. 4.1). For a sufficiently small yet non-zero value of $|\omega_1 - \omega_2|$, one finds a very narrow window of size s over which the system is capable of demonstrating both opacity as well as transparency. As $s \to 0$, the two roots come progressively closer. Fig. 4.1 illustrates this scenario for various choices of $|\omega_1 - \omega_2|$.

Level Attraction: It can be noted that the poles of the transmission and reflection demonstrate

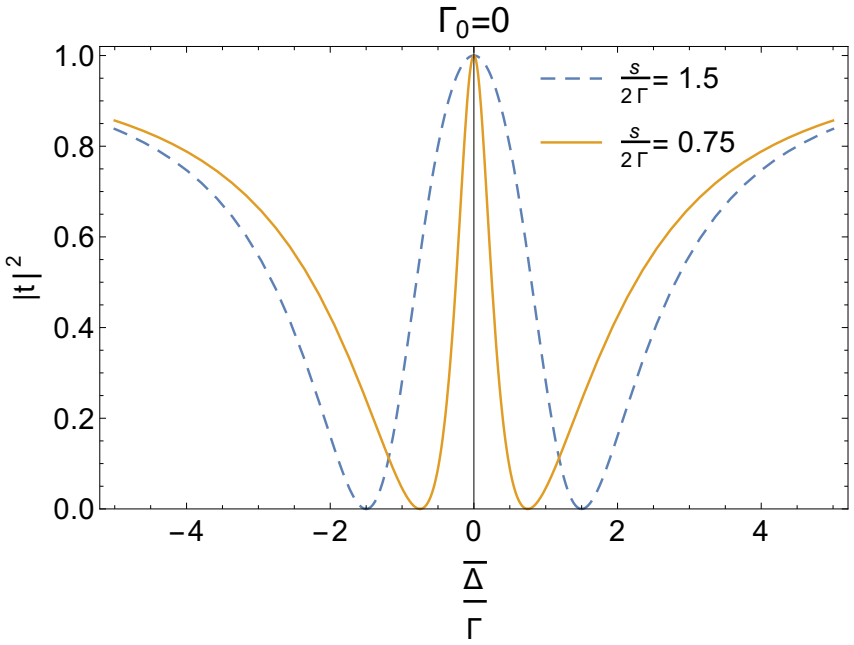

Figure 4.1: Transmission for a two-atom system without decay for a couple of values of $s = \omega_1 - \omega_2$ and with $kL = n\pi$. Perfect transparency is observed at $\omega_k = \frac{1}{2}(\omega_1 + \omega_2)$ (zero mean detuning), unless $\omega_1 = \omega_2$, in which case, the system is perfectly reflecting at zero detuning. The two roots of the transmission come closer as the atomic frequencies approach each other.

features remindful of level attraction. These poles occur at

$$\overline{\Delta}_{\pm}^{(\mathrm{p})} = -i\Gamma \pm \sqrt{\left(\frac{s}{2}\right)^2 - \Gamma^2}. \tag{4.5}$$

Level attraction is typically observed between the normal modes of two coupled oscillators when one of the bare modes has negative energy and the modes have comparable decay rates. When the coupling strength equals or exceeds a critical value, the level separation vanishes. As a direct analogy, we see, in our case, that the real parts of the transmission poles coincide and become 0 in the region $\frac{s}{2} \leq \Gamma$, while the imaginary parts expand and shrink respectively. The point of transition where the coupling equals this critical value is referred to as an exceptional point where the complex eigenfrequencies coincide [97]. Realizing level attraction has been quite a challenge from an experimental perspective and consequently, there is burgeoning interest in level attraction and phenomena occuring in the vicinity of exceptional points. Recently, level attraction has been

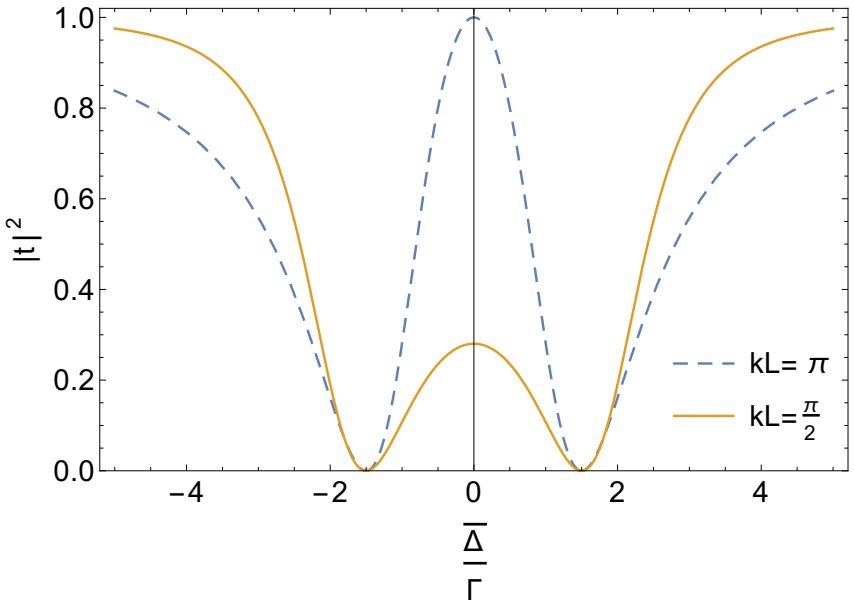

Figure 4.2: Comparison of transmission spectra corresponding to $kL = \pi$ and $kL = \frac{\pi}{2}$, with $s = 1.5\Gamma$. The transmission peak attains unit height for $kL = \pi$ whereas it is much shorter than unity for $kL = \frac{\pi}{2}$.

observed in a variety of systems and topological behavior around an exceptional point has also been explored [98–104].

In the waveguide case with two atoms, we see that the transmission has zeros at

$$\overline{\Delta}_{\pm}^{(\mathrm{r})} = \pm\frac{s}{2}, \tag{4.6}$$

which simultaneously determine the peaks of the reflection spectrum. These zeros are close to the the real parts of the poles when $\frac{s}{2} \gg \Gamma$. In the complementary regime, when $\frac{s}{2}$ is comparable to Γ, the real parts of the poles become small compared to the respective imaginary parts, as a consequence of which, the resolution between the two levels (or the two poles) becomes difficult. This problem of resolution arises fundamentally because Γ not only appears in the discriminant of the poles, but also acts as a natural broadening term.

The shrinking of the transmission width as $\frac{s}{2}$ goes below Γ is clearly reflected in the transmis-

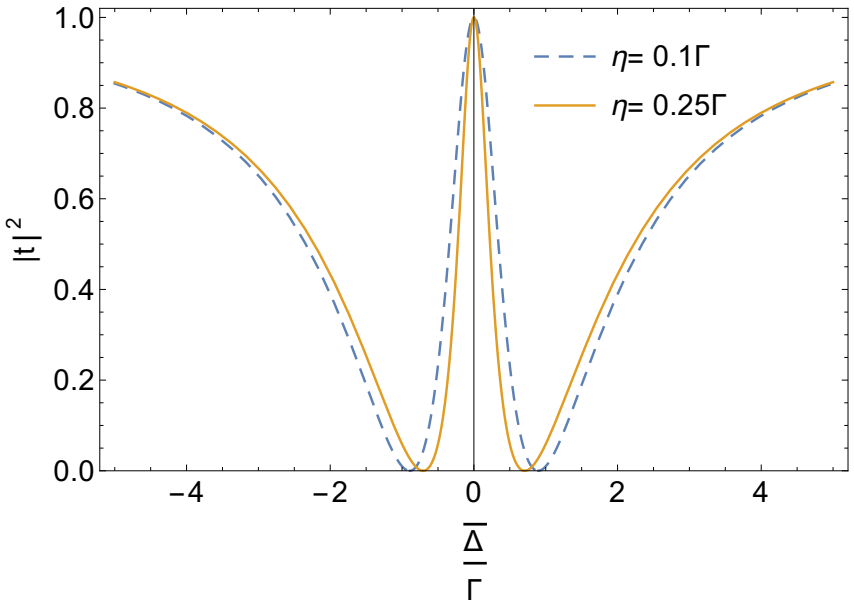

Figure 4.3: Transmission at $kL = n\pi$ for $\frac{s}{2} = \Gamma - \eta$ with $\eta = 0.1\Gamma$ and $\eta = 0.25\Gamma$.

sion plots shown in Fig. 4.3. Note that for $\frac{s}{2} = \Gamma$, the poles given by Eq. 4.5 become degenerate. Thus, if we define $\frac{s}{2} = \Gamma - \eta$, then η depicts how far we are off the degeneracy point. For a positive value of $\eta > 0$, the pole $\overline{\Delta}_+^{(\mathrm{p})}$ shrinks in width, with the relevant width given by $\left(1 - \sqrt{\frac{2\eta}{\Gamma}}\right)\Gamma$. Choosing $\frac{\eta}{\Gamma} \sim 10^{-1}$, we find, in Fig. 4.3, that the transmission window becomes narrower as η becomes larger.

4.2 On the nonreciprocity of photon transport

For general system parameters, the noncommutativity of transfer matrices precludes the possibility of having reciprocal photon transport through the waveguide, even while there is symmetric coupling between the atoms and the waveguide. However, when kl is a multiple of π, one has perfect reciprocity. Let us consider the simpler scenario of two differentially detuned atoms in a waveguide and define the mean detuning of the incident photon $\overline{\Delta} = v_g k - (\omega_1 + \omega_2)/2$ and the relative atomic detuning $s = \omega_1 - \omega_2$. Then, for the general phase-dependent paradigm, the

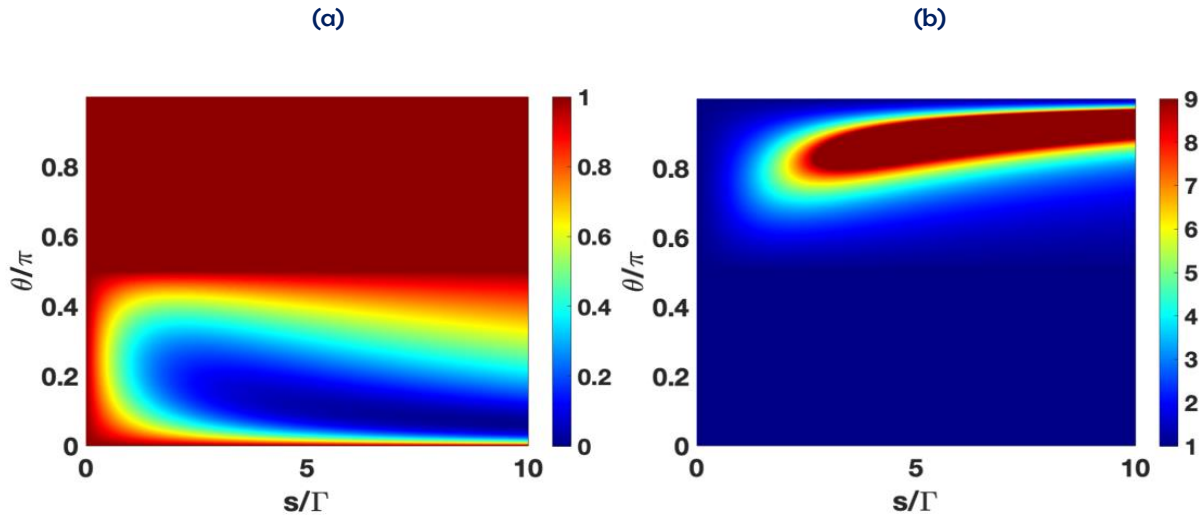

Figure 4.4: Degree of non-reciprocity, η, as a bivariate function of $\theta = kl$ and s/Γ. The left graph (a) prominently captures the region where $\eta < 1$, while the right one (b) accentuates the spot in which $\eta < 1$. All values in the range $\eta \geqslant 1$ are encoded as 1 in (a), while those in the set $\eta \geqslant 9$ are mapped to 9 in (b). Very small or very large values of η indicate substantial non-reciprocity. System parameters have been constrained to the space $\overline{\Delta} = 0$ (i.e., equal and opposite detunings), and $\Gamma = \Gamma_0$ (i.e. critical coupling).

reflection from the atomic system can be expressed as

$$r = -\frac{\Gamma^2(e^{i\alpha}-1) + i\Gamma[(e^{i\alpha}+1)(\overline{\Delta}+i\Gamma_0) - (e^{i\alpha}-1)s/2]}{(\overline{\Delta}+i(\Gamma+\Gamma_0))^2 + \Gamma^2 e^{i\alpha} - (s/2)^2}, \tag{4.7}$$

where $\alpha = 2kl$. Therefore, unless kl is an integral multiple of π, the above expression depends on s which is order dependent.

Quantifying Nonreciprocity: To quantify the extent of non-reciprocity, we could define the ratio $\eta = \left|\frac{r_{12}}{r_{21}}\right|^2$, where r_{ij} represents the coefficient of reflection from an atomic chain with the atoms with frequency ω_i and ω_j in positions 1 and 2 respectively. Clearly, $\eta = 1$ would signify perfect reciprocity. From Eq. (4.7), it follows, on using $(e^{i\alpha}-1)/(e^{i\alpha}+1) = i\tan(\alpha/2)$, that

$$\eta = \frac{(\overline{\Delta} + \Gamma\tan kl)^2 + (\frac{s}{2}\tan kl - \Gamma_0)^2}{(\overline{\Delta} + \Gamma\tan kl)^2 + (\frac{s}{2}\tan kl + \Gamma_0)^2}, \tag{4.8}$$

which deviates from unity whenever $\Gamma_0 \neq 0$ and $kl = n\pi$. Thus, the existence of a dissipative channel is central to the absolute reciprocity of photonic energy transfer. Note that Eq. (4.7) also implies $\eta(-s) = [\eta(s)]^{-1}$, which means that if a certain s maximizes η, flipping the sign of s would minimize the same for an otherwise constant set of parameters. The two panels in Fig. 4.4 demonstrate the two-dimensional plots of η when $\overline{\Delta} = 0$ and $\Gamma = \Gamma_0$, with the convention $s > 0$. The value of η can be much larger than 1 as well if it lies well within the dark red regions shown on either panel. For instance, the phase $kl = 5\pi/6$ supports a maximum asymmetry of $\eta \approx 13.78$ in the chosen parameter space. This indicates that the reflected intensity for one direction of incidence is almost 14 times that for the opposite direction of incidence[105].

Reciprocity for $kL = n\pi$ as a general fact: As was discussed in the context of a two-atom system, reciprocity is entailed for the choice of phase $kL = n\pi$ even for a multiatom chain. It follows, quite generally, from the expressions in Eq. (4.3), that $kL = n\pi$ ensures perfect optical reciprocity for any arbitrary chain size. In fact, this choice of phase is both necessary and sufficient for reciprocity in both the reflection and the transmission. The fundamental property that brings about this reciprocal character is the commutativity between any two transfer matrices, i.e.

$$[\mathcal{L}_r, \mathcal{L}_s] = 0 \ \ \forall\, r, s. \tag{4.9}$$

The commutation relation follows from the form in Eq. 4.3. As an essential implication of this, one finds that the matrix product $\prod_{j=1}^{N} \mathcal{L}_j$ is insensitive to the order in which the individual matrices are multiplied. Consequently, no matter what the order of the atoms is, one has the same transmission and reflection coefficients. Of course, this result is valid under the assumption that each emitter couples identically to the left as well as the right-propagating fields, as far as the two coupling strengths are concerned.

4.3 General multiemitter chain: Condition for transparency

We now bring out some interesting features of the spectral behavior collectively induced by a chain of multiple emitters with nonidentical detunings, corresponding to a spatial periodicity so chosen that $kL = n\pi$. In Chapter 3, Sec. 3.1, the analytical expressions for the spectral amplitudes were derived for a system of identical emitters for which the transfer matrices were also identical. Through a diagonalization procedure, the matrix product could be exactly calculated. However, $kL = n\pi$ is an EP of the transfer matrices, since the eigenvalues coincide and become $(-1)^n$. Hence, diagonalization fails. However, the cascaded transfer-matrix product becomes tractable when the lattice periodicity becomes commensurate with the wavelength, i.e., for $kl = n\pi$, with n as any natural number.

Analytical solution for $kL = n\pi$: In this case, the transfer matrices reduce to

$$L_j = (-1)^n(\mathbb{1} + \delta_j^{-1}\rho_-), \tag{4.10}$$

where $\mathbb{1}$ is the 2x2 Identity matrix, and $\rho_- = \sigma_y - i\sigma_z$ is a spin-annihilation operator in the σ_x-eigenbasis. Since $\rho_-^n = 0\ \forall n \geq 2$, the transfer matrices commute, and the transfer matrix product becomes

$$\begin{aligned}\prod_{j=1}^{N}\mathcal{L}_j &= (-1)^{nN}\left[\mathbb{1} + \left(\sum_{j=1}^{N}\delta_j^{-1}\right)\rho_-\right] \\ &= (-1)^{nN}\begin{bmatrix} 1 - i\Gamma\sum_{j=1}^{N}\delta_{k(j)}^{-1} & -i\Gamma\sum_{j=1}^{N}\delta_{k(j)}^{-1} \\ i\Gamma\sum_{j=1}^{N}\delta_{k(j)}^{-1} & 1 + i\Gamma\sum_{j=1}^{N}\delta_{k(j)}^{-1}\end{bmatrix}.\end{aligned} \tag{4.11}$$

By virtue of this simplification, the following transmission and reflection coefficients entail:

$$t = \frac{1}{1 + i\Gamma\sum_{j=1}^{N}(v_g k - \omega_j + i\Gamma_0)^{-1}}, \quad r = -\frac{i\Gamma\sum_{j=1}^{N}(v_g k - \omega_j + i\Gamma_0)^{-1}}{1 + i\Gamma\sum_{j=1}^{N}(v_g k - \omega_j + i\Gamma_0)^{-1}}. \tag{4.12}$$

The collective effect due to emission from multiple periodically spaced emitters is clearly embodied in the aforementioned expressions. The spectral dependence on the detunings has a close resemblance with that in the single-emitter scenario. The key factor that modifies the spectrum is $\sum_{j=1}^{N}(v_g k-\Omega_j)^{-1}$, an additive effect of the inverse detunings pertaining to the individual emitters. The expression is, of course, not as simple for other choices of phase. As a further simplification, let us focus on the case where Γ_0 is small enough to be dropped from consideration. This, in principle, entails in the possibility of generating perfect transmission through suitable arrangements of the individual detunings. The condition for transparency ($r = 0$ and $t = 1$) is, thus, given by

$$\sum_{j=1}^{N} \frac{1}{\Delta_{k(j)}} = 0. \tag{4.13}$$

For a single emitter, this relation is clearly impossible to satisfy and therefore, a single atom in a waveguide can not suppress reflection completely[†]. One must have multiple atoms to be able to achieve transparency. In a double-emitter scenario, where $N = 2$, the condition translates to $2\omega_k = \omega_1 + \omega_2$, which implies an exactly antisymmetric assignment of detunings to the two emitters. This is in line with what was highlighted in the previous section dedicated to the study of a two-atom chain (see Fig. 4.1).

For $N = 3$, the corresponding constraint appears as a quadratic equation

$$3\omega_k^2 - 2(\omega_1 + \omega_2 + \omega_3)\omega_k + \omega_1\omega_2 + \omega_2\omega_3 + \omega_3\omega_1 = 0, \tag{4.14}$$

with roots given by

$$\frac{1}{3}\left[\omega_1 + \omega_2 + \omega_3 \pm \sqrt{\omega_1^2 + \omega_2^2 + \omega_3^2 - \omega_1\omega_2 - \omega_2\omega_3 - \omega_3\omega_1}\right].$$

The discriminant can be re-expressed as $\frac{1}{2}[(\omega_1 - \omega_2)^2 + (\omega_2 - \omega_3)^2 + (\omega_3 - \omega_1)^2]$, which, being a sum of squares, is strictly non-negative, and hence, the roots are real.

[†]In fact, for a single atom, the solution is trivial, i.e., $\Delta_k \to \infty$, which practically symbolizes the absence of an atom.

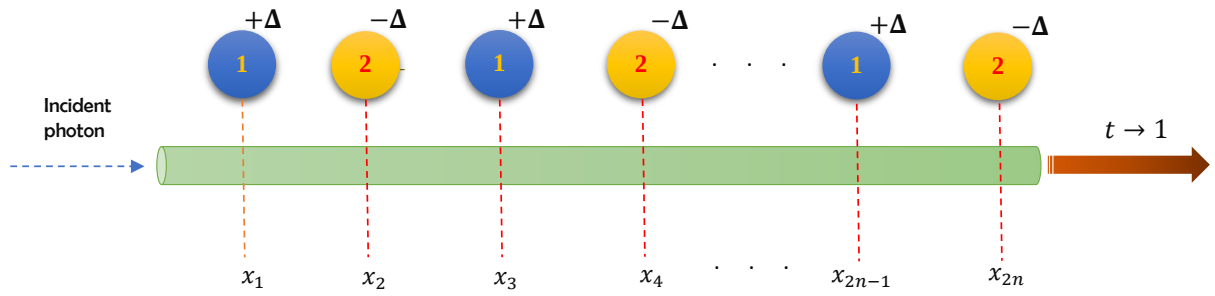

Figure 4.5: Even number of emitters with equal and opposite detunings assigned in pairs generates transparency. The order of the atoms is not important, so the arrangement shown here is just one of the possible permutations.

Even chain size: In general, it is easy to see that for even number of emitters in the chain, it is always possible to make the system transparent if the atomic transition frequencies can be so adjusted that for any atom detuned by a certain amount, there exists another atom in the chain detuned by the same amount but in the opposite sense (Fig. 4.5). In other words, for a chain of $2l$ atoms, an assignment of the frequency detunings $+\Delta_1$, $-\Delta_1$, $+\Delta_2$, $-\Delta_2$,... $+\Delta_l$, $-\Delta_l$, in no particular order, would give rise to transparency in the system. Such an asymmetric pairwise assignment of detunings lead to Fano minima in the reflection spectrum, which signifies a destructive interference between the reflected waves emanating from the emitters. Concomitantly, the transmitted waves constructively interfere, leading to perfect transmission. This extreme resonant inhibition of the reflection amplitude relative to the single-atom emission is a new phenomenon that is not observed at $kL = n\pi$ for a system of identically detuned emitters.

Odd chain size: On the other hand, if one has odd number of emitters in the chain, one can recover the single-atom emission spectra by assigning pairwise asymmetric detunings to any randomly chosen $(N-1)/2$ emitter pairs, leaving out a single atom. It then follows from Eqs. 4.12, that the remaining atom completely determines the spectral characteristics. That is, if this particular atom has a transition frequency ω_0, the transmitted spectrum due to the entire atomic chain

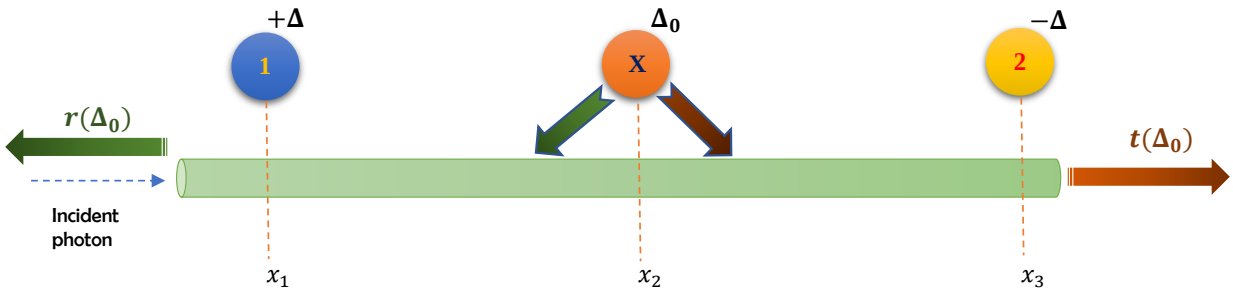

Figure 4.6: A system of three atoms, out of which two carry equal and opposite detunings $+\Delta$ and $-\Delta$. The odd one out (the middle one, in this figure) with a detuning of Δ_0 determines the spectral behavior, and no collective effects exist. This behavior transcends to the case of any odd number of emitters in the chain with a commensurate assignment of frequency detunings. When $\Delta_0 = 0$, the system behaves as a perfectly reflecting mirror.

reduces simply to

$$t = \frac{1}{1 + i\Gamma(\omega_k - \omega_0)^{-1}} , \tag{4.15}$$

which is identical to the transmission coefficient with just that single atom coupled to the waveguide (Fig. 4.6). Stated differently, when an even number of atoms with a pairwise asymmetric assignment of frequency detunings are added, in a periodic fashion, to a single atom coupled to a waveguide, no discernible collective effects emerge. The order of this arrangement and therefore, the location of the odd atom are not important. This makes sense from the perspective of Fano interference, since the reflected waves from the appended atoms destructively interfere, while that from the residual atom effectively goes through unperturbed. As a consequence, if the odd atom is in resonance with the laser frequency, the system resembles a perfectly reflecting mirror, regardless of the frequency detunings of the other atoms.

When all atoms are identical: Finally, in the event that all the atoms have identical frequencies, one can observe Dicke-type superradiant behavior due to enhancement of the reflection amplitude. If the atomic frequencies are all set equal to ω_0, the corresponding transmitted spectrum is obtained

to be

$$t = \frac{1}{1 + iN\Gamma(\omega_k - \omega_0)^{-1}} \,, \tag{4.16}$$

which pertains to a Lorentzian with a half-width of $N\Gamma$. One can see a direct analogy of this result with the phenomenon of resonant diffraction from a system of periodically spaced quantum wells, which demonstrates superradiant properties under the Bragg reflection condition, i.e. when the periodicity is a half-integral multiple of the incident wavelength [106, 107]. At $kL = n\pi$, the reflection from the atomic chain is endowed with a single pole, identical to the Bragg reflection scenario, which has a linewidth proportional to the size of the system. However, having the added flexibility of adjusting the atomic frequencies brings out different types of interesting radiant behavior that one can observe, in principle. We do not merely encounter the possibility of superradiant reflection, but also come across new points of transparency.

4.4 Robustness against dissipation into side modes

The simplistic results laid out in the preceding discussions in Secs. 4.1 and 4.3 hold only when Γ_0 is small enough to be ignored. However, we can look at more realistic scenarios with dissipation included ($\Gamma_0 \neq 0$) and examine the effect of the same on those observations. For a two-atom chain, we discover that the behavior changes drastically depending on how the relative detuning between the atomic frequencies compares to this decay rate. Fig. 4.7 shows the plots for $|t|^2$ vs. $\left|\frac{\overline{\Delta}}{\Gamma}\right|$ for a good-quality waveguide with a weak dissipative channel ($\Gamma_0 = 0.1\Gamma$), for varying values of $|\omega_1 - \omega_2|$. It is observed that for sufficiently small values of the latter, the transmission peak almost disappears, whereas for large values, the height of the peak approaches unity. In other words, by adjusting the relative frequency detuning between the emitters, one can achieve either high opacity or high transparency around $v_g k = \frac{1}{2}(\omega_1 + \omega_2)$. For perfectly matched up atomic frequencies, i.e. $\omega_1 = \omega_2$, one observes a diametrically opposite behavior as the two roots coincide - the central peak is replaced by a trough. This is a Dicke-type superradiant effect - for negligible decay, the

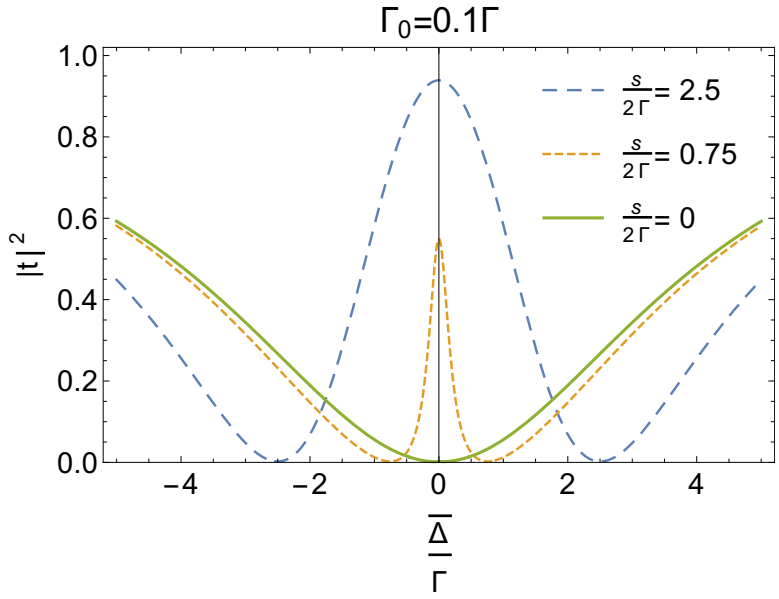

Figure 4.7: Effect of dissipation on the transmission of a two-atom system. If the dissipative channel is weak compared to the waveguide channel, the profile closely resembles the dissipation-free spectrum, except when the frequency mismatch between the atoms is smaller than or comparable to the rate of dissipation. The central peak disappears as $s \to 0$ and is replaced by a trough at $s = 0$.

transmission profile is a vertically inverted Lorentzian with a half-width of 2Γ.

One can analytically understand this behavior by considering two specific regimes, (i) $s \ll 2\Gamma_0$ and (ii) $s \gg 2\Gamma_0$. At $\overline{\Delta} = 0$, one obtains

$$t = \frac{\left(\frac{s}{2}\right)^2 + \Gamma_0^2}{\left(\frac{s}{2}\right)^2 + \Gamma_0(\Gamma_0 + 2\Gamma)} . \tag{4.17}$$

For small relative detuning between the atoms, i.e. $s \ll 2\Gamma_0$, the approximate form is given as $|t|^2 \approx \frac{\Gamma_0^2}{4\Gamma^2}$, which is vanishingly dimunitive, as long as the decay rate is much less than Γ. In the opposite scenario when $s \gg 2\Gamma_0$, we get $|t|^2 \approx 1 - \mathcal{O}\left(\frac{8\Gamma\Gamma_0}{\delta^2}\right)$. Thus, a fairly high degree of transparency can be achieved by specifically working with a large relative detuning $|\omega_1 - \omega_2|$.

For a system of even number of emitters, in which half of them have detuning $+\Delta$ whereas the

other half have detuning $-\Delta$, the transmission goes as

$$t = \frac{\Delta^2 + \Gamma_0^2}{\Delta^2 + \Gamma_0(\Gamma_0 + N\Gamma)} \,. \tag{4.18}$$

For $\Delta \ll \Gamma_0$, $|t|^2 \approx \left(\frac{\Gamma_0}{N\Gamma}\right)^2$, which testifies to highly reflecting behavior. However, when $\Delta \gg \Gamma_0$, we have $|t|^2 \approx 1 - \mathcal{O}\left(\frac{4N\Gamma\Gamma_0}{\Delta^2}\right)$, implying near-transparency. The situation here is reminiscent of EIT where perfect transparency emerges in the absence of dissipative transitions.

Similarly, when there are odd number of emitters, with $\frac{N-1}{2}$ emitters each having a detuning of $+\Delta$ and $\frac{N-1}{2}$ other emitters each detuned by $-\Delta$, one has, for the transmission coefficient,

$$t = \frac{1}{1 + \frac{(N-1)\Gamma\Gamma_0}{\Delta^2 + \Gamma_0^2} + \frac{i\Gamma}{v_g k - \omega_0 + i\Gamma_0}} \,, \tag{4.19}$$

where ω_0 is the frequency of the remaining atom. When Δ is large compared to Γ_0, one can discern a re-emergence of single-atom behavior.

One might also wonder how robust the transparency effect happens to be against sign-flip error in the detunings. If we take the instance of a simple two-emitter system and ignore dissipative couplings to keep the physics transparent, we know that perfectly transparency ensues from assigning detunings that are equal in magnitude but opposite in signature to the individual emitters. Practical setups are not devoid of noise, and perfect flip in signature would be too ideal to achieve. In order to test the robustness against this indispensable error, we can re-examine the case of an atomic array of even parity, with frequency detunings assigned in a way such that the j^{th} pair carries the detunings $\{+\Delta_j, -\Delta_j + \epsilon_j\}$. The transmission becomes

$$t = \frac{1}{1 - i\Gamma \sum_{j=1}^{N} \frac{\epsilon_j}{\Delta_j^2}} \sim 1 + i \sum_{j=1}^{N} \frac{\Gamma\epsilon_j}{\Delta_j^2} + \ldots \tag{4.20}$$

This means that the transparency in our optical setup can largely withstand fluctuations in sign-flip, as long as the the fluctuations are tiny compared to the magnitude of the detunings. An error

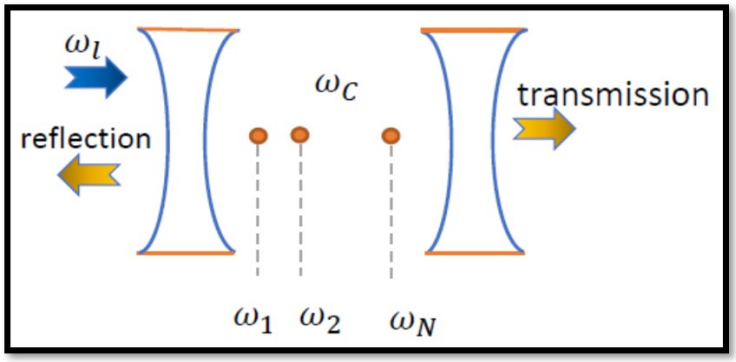

Figure 4.8: Chain of emitters placed inside a cavity resonator which is driven by an external laser.

analysis can also be made in relation to the proclaimed reemergence of single-atom behavior in a chain of odd size, subjected to a similar assignment protocol, which will similarly vindicate its robustness against imperfections in sign-flip.

4.5 Transparency in cavity QED: General analogies and discrepencies

Having discussed how to generate transparency in waveguide setups, it is instructive to explore similar effects in a cavity-based platform. To that end, we consider a chain of N atomic scatterers placed at the antinodes of an optical cavity, as depicted in Fig. 4.8. An optical laser of frequency ω_l drives the cavity (resonant mode ω_c), which, then, excites the emitters coupled to the intracavity field. Assuming a cavity leakage rate of κ across each mirror, while ignoring internal cavity losses and atomic dampings, the system Hamiltonian in the reference frame of the laser frequency takes the form

$$H/\hbar = \delta a^\dagger a + \sum_{j=1}^{N} \Delta_j S_z^{(j)} + \sum_{j=1}^{N} g_j (S_+^{(j)} a + S_-^{(j)} a^\dagger) + i\mathcal{E}_{\text{in}}(a^\dagger - a) \tag{4.21}$$

where $\delta = \omega_c - \omega_l$, g_j's quantify the strengths of atom-cavity coupling, $\Delta_j = \omega_j - \omega_l$ is the detuning of the j^{th} atom, and $\mathcal{E}_{\text{in}} = \sqrt{\dfrac{2\kappa P_l}{\hbar\omega_l}}$ is the Rabi frequency of the control field, and P_l is the driving power. We have also introduced the atomic pseudospin operators $S_+^{(j)} = |e\rangle_j \langle g|$, $S_-^{(j)} = |g\rangle_j \langle e|$,

and $S_z^{(j)} = \frac{1}{2}(|e\rangle_j \langle e| - |g\rangle_j \langle g|)$, which satisfy the spin-$\frac{1}{2}$ angular momentum algebra. Now, from the master equation for cavity QED,

$$\frac{\partial \rho}{\partial t} = -\frac{i}{\hbar}[H, \rho] - \kappa(a^\dagger a \rho - 2a\rho a^\dagger + \rho a^\dagger a) - \gamma \sum_{j=1}^{N} (S_+^{(j)} S_-^{(j)} \rho - 2S_-^{(j)} \rho S_+^{(j)} + \rho S_+^{(j)} S_-^{(j)}) \quad (4.22)$$

which assumes the reservoirs to be vacuum fields, we find the equations of motion to be

$$\begin{aligned} \dot{a} &= -(2\kappa + i\delta)a - i\sum_{j=1}^{N} g_j S_-^{(j)} + \mathcal{E}_{\text{in}}, \\ \dot{S}_-^{(j)} &= -(\gamma_j + i\Delta_j)S_-^{(j)} + 2ig_j S_z^{(j)} a, \end{aligned} \quad (4.23)$$

where we have dropped the expectation value notation $\langle . \rangle$. The damping terms are assumed to be identical for all the qubits. In the steady state, using the mean-field approximation, one can decouple the field and the atomic operators thus, $\left\langle S_z^{(j)} a \right\rangle \simeq \left\langle S_z^{(j)} \right\rangle \langle a \rangle$ for brevity. Further, in the weak excitation limit, it is safe to invoke the approximation $\left\langle S_z^{(j)} \right\rangle \approx -\frac{1}{2}$, i.e., the populations remain predominantly in their ground states. This allows us to solve the steady-state amplitude of the intracavity field,

$$a_{\text{s.s}} = \frac{1}{2\kappa + i\left(\delta - \sum_{j=1}^{N} \frac{g_j^2}{\Delta_j - i\gamma_j}\right)} \mathcal{E}_{\text{in}} \quad (4.24)$$

Next, on using the input-output relation for cavity QED, $\mathcal{E}_{\text{out}} = 2\kappa a_{\text{s.s}}$, where $\mathcal{E}_{\text{out}}$ corresponds to the transmitted field (in frequency units), we find the transmission coefficient to be

$$\begin{aligned} t = \frac{\mathcal{E}_{\text{out}}}{\mathcal{E}_{\text{in}}} &= \frac{2\kappa}{2\kappa + i\left(\delta - \sum_{j=1}^{N} \frac{g_j^2}{\Delta_j - i\gamma_j}\right)}, \\ &\xrightarrow{\Gamma_j \ll \Delta_j} \frac{2\kappa}{2\kappa + i\left(\delta - \sum_{j=1}^{N} \frac{g_j^2}{\Delta_j}\right)}. \end{aligned} \quad (4.25)$$

We find that on setting $\delta = 0$ and treating the coupling constants as equal, i.e. $g_j = g \; \forall j$, we recover results akin to the waveguide transport. When the atoms have identical detunings, superradiant effect becomes evident from Eq. (4.25), as the collective linewidth becomes $\frac{Ng^2}{2\kappa}$. For disparate detunings, the possibility of transparency hinges on the parity of the ensemble size. An even chain size allows transparency upon imparting equal and opposite pairwise detunings, while an odd chain size, for a similar assignment protocol, leads to an effective retrieval of single-atom emission characteristics. Thus, there are obvious parallels between cavities and waveguides when they are integrated with atomic scale dipoles [105]. However, photon transfer in cavity setups does not depend on the order in which the atoms are arranged, and is, therefore, always reciprocal. On the other hand, a waveguide mediates a phase-sensitive coupling between atoms, and this phase-dependence makes photon transport generally nonreciprocal, as has been discussed earlier.

4.6 Summary

To summarize, we have thrown light on new possibilities that emerge in relation to the collective effects of a chain of atoms side-coupled to a waveguide when the interemitter separation is fixed to satisfy $kL = n\pi$, where n is an integer. For a chain of N atoms, we have demonstrated the emergence of new Fano minima (transparency points) in the reflection spectrum for negligible dissipation. When N is even, we have seen how transparency can be generated by assigning equal and opposite detunings to the atoms in pairs, while for odd N, we have highlighted the possibility of reproducing single-atom behavior through a similar assignment, so that the odd one out completely determines the emission spectrum. A system of identically detuned emitters, on the other hand, demonstrates superradiant behavior, similar to the reflection from a system of equidistant quantum wells under Bragg condition. We have also shown that the optical system demonstrates reciprocal behavior with respect to both transmission and reflection. In general, the system turns out to be insensitive to the order in which the atoms are arranged. Finally, it has been demonstrated, both analytically and graphically, that when dissipation into nonwaveguide modes cannot be neglected, one can still produce highly transparent behavior by implementing a considerable disparity in the

atomic transition frequencies. For a small mismatch in the frequencies, one, however, observes predominantly opaque behavior in its place.

5. NON-HERMITIAN PHYSICS AND ANTI-PT SYMMETRY*

In standard quantum mechanics, observable quantities are always represented by Hermitian operators. The eigenvalues of a Hermitian operator represent possible outcomes of the measurement of an observable represented by that operator. Once the measurement of, say, the energy is performed and the outcome recorded, the system collapses into a state of definite energy. States of definite energy are characterized by the *eigenstates* of the operator. If an operator has a complete set of eigenstates and real eigenvalues, then it becomes a viable candidate for representing a physical observable. Carl Bender was amongst the first to question the stringent criterion of Hermiticity and investigated the feasibility of non-Hermitian Hamiltonians which could *also support* real eigenvalues. This spawned the development of *PT-symmetric quantum theory* [108–110] where the Hermiticity condition is replaced by the invariance under simultaneous parity ($\hat{P}$) and time-reversal ($\hat{T}$) operation, i.e.

$$[\hat{PT}, H] = 0. \tag{5.1}$$

A *PT-symmetric Hamiltonian* is not Hermitian, but if the corresponding eigenstates are also symmetric w.r.t the $\hat{PT}$ operation, then its eigenvalues are real and eigenstates may be complete. Consequently, PT-symmetric Hamiltonians can, *also* be used, in principle, to describe quantum mechanical systems.

The Hamiltonian of a physical system characterizes its energy spectrum and time evolution, and is thus, of fundamental importance in quantum theory. In nature, all systems are invariably dissipative as they interface with their environment and relax into equilibrium. As a consequence, an open-system formulation in terms of the master equation becomes imperative. Such a description leads to the system dynamics being described in terms of an effective non-Hermitian Hamiltonian.

*Sec. 5.4 of this chapter is reprinted with permission from *Cavity mediated level attraction and repulsion between magnons* by J. M. P. Nair, D. Mukhopadhyay, and G. S. Agarwal, Phys. Rev. B **105** 214418 (2022), published by the American Physical Society. Collaboration with J. M. P. Nair is acknowledged.

The transient as well as the steady-state characteristics of an open system depends strongly on the symmetry properties of their effective Hamiltonian. Enigmatically, PT symmetry necessitates systems to feature a balanced tradeoff between gain and loss. Such a criterion would demand extrinsic administration of gain into the system. To circumvent the challenge of gain administration, a separate category of systems that exhibit a modified symmetry property was theoretically proposed by Ge and Turecii in 2013 [44] and later experimentally implemented by various scientific groups [45, 47, 48] as interest in its utility flourished expeditiously. This has been classified as *anti-PT symmetry* where the commutator in Eq. (5.1) is replaced by the anticommutator, i.e.,

$$\{\hat{PT}, H\} = 0. \tag{5.2}$$

Alternatively, a Hamiltonian with anti-PT symmetry flips sign under the joint action of the parity and time-reversal operations. Such systems can display intriguing properties in the absence of any gain medium, which set them apart from the class of PT-symmetric systems. Traditionally, much attention has, however, been invested on the transient dynamics of anti-PT symmetric systems. Our research, on the other hand, is focused on the steady-state character of these systems, and contextualized, for specificity, on *hybrid cavity-magnonic systems*.

This chapter is organized in the following manner. Briefly acknowledging the relevance of non-Hermitian dynamics in coupled optical systems, we outline the operational features of the $\hat{PT}$ operator in Sec. 5.1, and discuss spontaneous phase transition in anti-PT symmetric systems. In Sec. 5.2, we provide a compact background on some optical implementations of anti-PT symmetry, following which, we uncover the role of *dissipative coupling* in realizing the associated Hamiltonian. Sec. 5.3 is dedicated to a thorough analysis of cavity magnonics. We also discuss how anti-PT symmetry can be achieved in magnon-based platforms. In Sec. 5.4, we analyze the bad-cavity regime which also supports a realization of this symmetry. We conclude with a summary of discussions in Sec. 5.5.

5.1 General characteristics of non-Hermitian systems and introduction to anti-PT symmetry

According to the coupled-mode theory in optics, the temporal evolution of an open system of two harmonic oscillators can be described via a 2×2 non-Hermitian Hamiltonian matrix H. In response to any electromagnetic excitation, the dynamics of the system, in the rotating frame of the drive, can be encoded as

$$\begin{pmatrix} \dot{\alpha_0} \\ \dot{\beta_0} \end{pmatrix} = -iH \begin{pmatrix} \alpha_0 \\ \beta_0 \end{pmatrix} + \Omega \begin{pmatrix} 1 \\ 0 \end{pmatrix}, \tag{5.3}$$

where (α_0, β_0) signify the mean-field amplitudes of the two modes, $\mathcal{E}$ is some generalized Rabi frequency, and ω_d is the laser frequency. The steady-state properties of the system would hinge on the symmetry properties of $H = \begin{pmatrix} \rho & \sigma \\ \eta & \zeta \end{pmatrix}$, where the matrix elements are currently taken to be arbitrary complex numbers. The diagonal terms are related to the frequency detunings and the individual dissipation rates, while the off-diagonal terms signify coupling between the two modes, often found to be symmetric. The spectrum of this matrix would be generally complex and the evolution non-unitary. If the corresponding eigenfrequencies never intersect in the parameter space, a minimum frequency gap exists between the normal modes, which has been variously referred to as level repulsion/splitting or mode anticrossing. In contrast, there could be scenarios where the eigenfrequencies converge and coalesce over a band of frequencies in the parameter space. This phenomenon is termed level attraction or mode crossing. Compared to level repulsion, extensive exploration into the subject of level crossing is a fairly recent pursuit [98–104]. In the following, we shall discuss the feasibility of implementing level attraction in a bimodal framework, starting from a brief exegesis of the $\hat{PT}$ operation on these systems.

$\hat{PT}$ transformation: The generic 2×2 matrix H lends itself to two very interesting symmetries, namely PT-symmetry, which is defined by the condition $[PT, H] = 0$, and anti-PT symmetry,

which subscribes to $\{PT, H\} = 0$. The operators $\hat{P}$ and $\hat{T}$ commute, $[\hat{P}, \hat{T}] = 0$, and both satisfy the property $\hat{P}^2 = \hat{T}^2 = \mathbb{1}$. In a 2×2 system, the effect of the parity operator is underscored by the transformation property

$$\hat{P} \left|\pm\right\rangle_z = \left|\mp\right\rangle_z , \tag{5.4}$$

$\left|\pm\right\rangle_z$ are eigenstates of the Pauli spin operator $\hat{\sigma}_z$. In the parlance of quantum information theory, this is equivalent to a bit-flip operation, and therefore, $\hat{P} = \hat{\sigma}_x = \begin{pmatrix} 0 & 1 \\ 1 & 0 \end{pmatrix}$. The time-reversal operator $\hat{T}$ is characterized by its operational signature of complex conjugation, i.e.,

$$\hat{T} z \hat{T} = z^*, \tag{5.5}$$

where $z \in \mathbb{C}$ is any complex scalar quantity. This is an anti-linear operation since, it discriminates between real and imaginary scalars. However, it does leave the basis states $\left|\pm\right\rangle_z$ untouched. Taking stock of all these properties, we can formally write down the transformation of the matrix H under the joint application of $\hat{P}$ and $\hat{T}$:

$$H = \begin{pmatrix} \rho & \sigma \\ \eta & \zeta \end{pmatrix} \xrightarrow{\hat{P}} \begin{pmatrix} \zeta & \eta \\ \sigma & \rho \end{pmatrix} \xrightarrow{\hat{T}} \begin{pmatrix} \zeta^* & \eta^* \\ \sigma^* & \rho^* \end{pmatrix} = H'. \tag{5.6}$$

The matrix is said to be PT-symmetric when $H' = H$, and anti-PT symmetric for $H' = -H$. The two symmetries can be visualized as follows. Consider two systems A and B, which could feature either gain or loss. Now swap the two systems, $A \leftrightarrow B$ and interchange the gain/loss in the individual modes. If the composite system can be described exactly by the *same Hamiltonian* as before, it is PT-symmetric. Contrarily, if the Hamiltonian undergoes *only a sign change* in the process, the composite system is anti-PT symmetric.

Anti-PT symmetry and spontaneous phase transition: The PT-symmetric configuration is con-

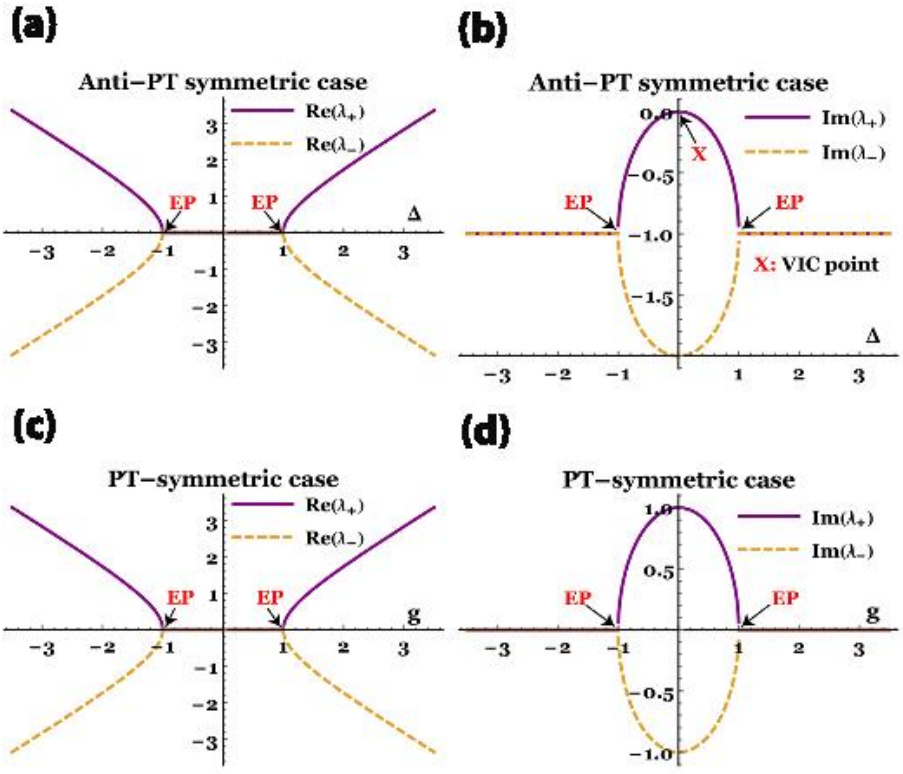

Figure 5.1: a), b) Eigenfrequencies and linewidths for an anti-PT symmetric system, plotted against a variable $\Delta = \delta/2$, calculated in units of Γ. While EPs emerge at $\Delta = \pm\Gamma$, the VIC-induced linewidth suppression (designated as X) corresponds to $\delta = 0$. c), d) Analogous plots for the PT symmetric system, against the coupling strength g, in units of γ, at $\Delta = 0$. EPs are found at $g = \pm\gamma$.

formable with the parameter structure $H_{11} = \delta/2 - i\gamma$, $H_{22} = \delta/2 + i\gamma$, $H_{12} = H_{21} = g$, where δ, γ, g are all real. This structure implies that a loss in mode a must be offset by a commensurate gain in mode b. An anti-PT symmetric realization of mode hybridization can be reconciled with the parameter description $H_{11} = \delta/2 - i\gamma$, $H_{22} = -\delta/2 - i\gamma$, $H_{12} = H_{21} = -i\Gamma$, where δ, γ, Γ are all real. The coherence-inducing off-diagonal elements of H characterize a purely dissipative form of interaction between the two modes, which is termed as vacuum induced coherence (VIC) [56]. The diagonal terms indicate equal damping rates but opposite detunings in the two modes. Both PT-symmetric and anti-PT symmetric Hamiltonians exhibit level attraction, as illustrated by Fig. 5.1.

Let us now discuss the spontaneous phase transition of this anti-PT symmetric model [46]. It can be shown that the $\hat{PT}$ operator can share simultaneous eigenstates with H under certain conditions. On denoting the eigenvectors of H as $|\phi\rangle_\pm$ with their corresponding eigenvalues $\lambda_\pm$, we are led to the relation

$$\begin{aligned} H(\hat{PT}\,|\phi\rangle_\pm) &= -(\hat{PT})(H\,|\phi\rangle_\pm) \\ &= -\lambda_\pm^*(\hat{PT}\,|\phi\rangle_\pm), \end{aligned} \tag{5.7}$$

in which the defining property $\{PT, H\} = 0$ was used in the first step. This shows that $\hat{PT}\,|\phi\rangle_\pm$ are themselves eigenvectors of H with eigenvalues $-\lambda_\pm$. This is conformable with two distinct possibilities: (i) $\lambda_\pm$ are purely imaginary, satisfying $\lambda_\pm = -\lambda_\pm^*$, and $\hat{PT}\,|\phi\rangle_\pm = e^{i\theta_\pm}\,|\phi\rangle_\pm =$ for some phases $\theta_\pm$; (ii) $\lambda_\pm$ satisfy $\lambda_\pm = -\lambda_\mp^*$, with $\hat{PT}\,|\phi\rangle_\pm = e^{i\theta_\pm}\,|\phi\rangle_\mp$. The first possibility (i) describes the PT-symmetric phase, where $|\phi\rangle_\pm$ are also eigenstates of the $\hat{PT}$ operator, and therefore, themselves PT-symmetric. The second (ii) denotes the symmetry-broken phase, where the states are not direct eigenvectors of the $\hat{PT}$ operator but transform into each other under $\hat{PT}$ operation. The analytical forms of the eigenvalues of H are obtained to be $-i\gamma \pm \sqrt{(\delta/2)^2 - \Gamma^2}$ for $|\delta/2| > \Gamma$ and $-i\gamma \pm i\sqrt{\Gamma^2 - (\delta/2)^2}$ for $|\delta/2| < \Gamma$ (see Fig. 5.1(a,b)). Therefore, the former refers to the symmetry-broken phase whereas the latter pertains to the symmetric phase. The points of

transition $|\delta/2| = \pm\Gamma$, where the eigenvalues become degenerate, are known as exceptional points (EPs), which have been found useful in the context of sensing. The existence of EPs is *unique to non-Hermitian systems*. At an EP of order 2, both eigenfunctions of the system coalesce into a single level. That is to say, as the eigenvalues coincide, the corresponding eigenfunctions also *collapse into a unique eigenfunction* at an EP. The Hamiltonian becomes non-diagonalizable at this point, since its rank reduces to 1. Such a peculiar behavior sets EPs apart from ordinary degeneracies in Hermitian Hamiltonians. A Hermitian Hamiltonian *always* remains diagonalizable, regardless of the multiplicity of its spectrum. This is because, even at a degeneracy, a Hermitian Hamiltonian continues to possess a *complete set of eigenstates*. This is not the case for an EP observed in non-Hermitian systems, and one must resort to a Jordan normal decomposition of this Hamiltonian at the EP. Conventional degeneracies in Hermitian systems are also called Diabolic Points (DPs). Owing to the unique character of an EP, this has been found to useful in sensing applications as well as topological energy transfer [102–104, 111–113]. The sensing utility at an EP and its advantage over a DP would be explained in Sec. 6.1 of Chapter 6.

In addition to an EP, anti-PT systems possess a real singularity at $\delta \to 0$, $\gamma \to \Gamma$, which has immense sensing potential, allowing efficient detection of both linear and nonlinear perturbations in the system. This limiting point where one of the eigenmodes is completely quenched has been utilized for the sensing of weak nonlinearities. This is discussed in great detail in the following chapter. A key difference between PT-symmetric and anti-PT symmetric Hamiltonians is the existence of a unique steady state. A similar analysis as above would show that PT-symmetric eigenmodes are in the symmetric phase when the corresponding eigenvalues are purely real, i.e., when $g \geq \gamma$ in Fig. 5.1(c,d). In the symmetric phase, the eigenmodes are oscillatory, while in the symmetry-broken phase, one of these modes, λ_+ sustains exponential amplification. Thus, these systems, in general, do not permit a unique, non-equilibrium steady state. On the other hand, anti-PT symmetric eigenmodes always feature finite decay rates, except when the limit $\delta = 0$, $\gamma = \Gamma$ is attained. Consequently, the long-time behavior of these systems can be perfectly encapsulated in terms of well-defined and unique steady states, if one makes sure to avert the limiting real singu-

larity.

5.2 Realization of anti-PT symmetry in dissipatively coupled optical systems

Optical systems provide a versatile playground for exploring non-Hermitian physics, because light-matter interactions in nature are naturally accompanied by dissipative effects. More importantly, current technology allows the tunability of the optical properties of a medium through the appropriate incorporation of gain or loss. The realizability of PT symmetry in photonic systems has contributed immensely to the advancement of the study of non-Hermitian physics [114–116]. PT symmetry has been pivotal to the discovery of a number of unprecedented properties in photonics, such as asymmetric light transport [114, 117], simultaneous coherent perfect absorption and lasing [118, 119], superprism effect [120], and enhanced metrological precision [121]. The phase transition associated with PT symmetry has been measured in topological photonic systems [122] and complex-frequency band structures [123]. Unlike PT symmetry, anti-PT symmetry does not require any extrinsic gain, and is predisposed to simple laboratory realization. The seminal theoretical work in Ref. [44] envisioned the tailoring of anti-PT symmetry via the symmetrical balance of positive and negative refraction indices in a 1D synthetic heterostructure. In fact, the refractive index was supposed to be spatially modulated to satisfy antisymmetry under $\hat{PT}$ operation, i.e., $n(-x) = -n^*(x)$. In addition, the magnetic permeability was demanded to obey $\mu(-x) = -\mu(x)$. However, designing a composite system of metamaterials by balancing positive and negative refraction is experimentally not feasible. Subsequently, several theoretical studies were published, which were contextualized on optically dressed atomic lattices [124] and nonlinear optical systems [125]. However, the primary method for devising anti-PT symmetry, which is experimentally tenable, is via the indirect coupling of two systems mediated by a common reservoir. Such kinds of coupling have become popularized as *dissipative coupling*, since this is brought about by dissipation into the shared bath. The coupling is essentially non-Hermitian, ensuing from the master equation description of the two systems.

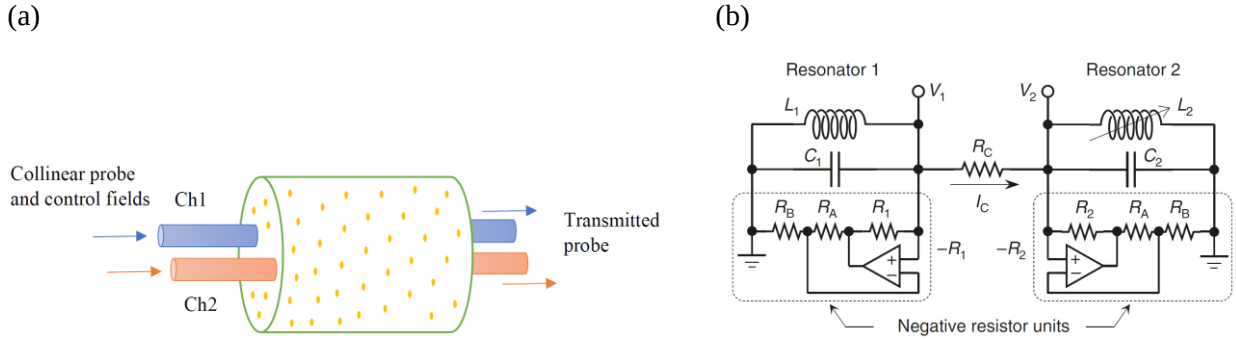

Figure 5.2: (a) Ballistic atomic motion in an atomic vapor cell distributes atomic coherence and establishes dissipative coupling between two optical channels, each of which contains a weak probe and a strong control field operating under the condition of EIT; (b) Realization of anti-PT symmetry in an electrical circuit: Two resistively coupled amplifying LRC resonators, each with a negative resistor unit.

Engineering anti-PT symmetry through dissipative couplings: The pioneering experiment by Peng *et al.* reported anti-PT symmetry by employing dissipative couplings between atomic spin waves resulting from rapidly moving atoms in a warm atomic vapor cell [45]. The corresponding setup is reproduced in Fig. 5.2(a). F. Yang *et al.*, in 2017, advanced a theoretical explanation highlighting how anti-PT symmetry could be engineered via dissipative couplings in linear optical systems [46]. Riding high on the sudden upsurge in interest on this subject, there was a proliferation of efforts to fabricate expedient systems featuring anti-PT symmetry. In 2018, this was experimentally demonstrated in a resistively coupled electrical LRC resonators [47]. The simplicity of the associated circuit model, as shown in Fig. 5.2(b), makes it especially attractive [†]. By now, a wide array of physical systems have been tailored to exhibit anti-PT symmetry in a multitude of settings including, but not limited to, driven cold atoms [126, 127], laser-cooled atomic ensembles [128], waveguides [46, 129], diffusive systems [130], coupled cavity-magnon systems [48], and many more. Recently, Wen *et al.* demonstrated anti-PT symmetry in a quantum circuit model with three qubits using nuclear spins [131]. Akin to the PT-symmetric setting, anti-PT symmetry also

[†]Fig. 5.2(a) has been redrawn from *Nature Physics, 12(12):1139–1145, (2016)*, while Fig. 5.2(b) has been adapted from *Nature Communications, 9(1):2182, (2018)* published as open access under the Creative Commons Attribution 4.0 International License.

supports spontaneous phase transition in the photonic eigenmodes across an EP, and experiments have successfully verified this phase transition (see, for example, [47]).

Origin of dissipative coupling: a quantum perspective: A notable example of a dissipatively coupled system which we have already discussed in the earlier chapters, is an array of atoms coupled to the 1D field continuum supported by a waveguide. However, in those chapters, we were principally concerned with the steady-state transport properties of photons. But the waveguide can also be treated as a Bosonic bath, which permits the adiabatic elimination of the waveguide degrees of freedom. This leads to an effective dissipative coupling between the atoms. The coupling has a quantum origin, as it is induced by the vacuum fields of the common bath, i.e., even when the bath contains no photons. We note, however, that this coupling is not specifically restricted to 2LAs. In fact, any quantum emitters, whether multilevel systems or harmonic oscillators would acquire the same characteristic coupling mediated by the waveguide photons. This implies that waveguide-integrated photonics can serve as a reliable platform to generate and modulate dissipative couplings between spatially separated quantum emitters. The general schematic is shown in Fig. 5.3. For instance, it has been shown that a microwave cavity can be dissipatively coupled to a single magnon mode in a ferrimagnetic material through an interceding microwave transmission line (see Fig. 5.4). A systematic prescription to study magnetic systems and magnon-photon couplings would be laid out in the next section. But before going into the topic of cavity-magnonics, we briefly outline, through a quantum mechanical treatment, how anti-PT symmetry can be achieved by coupling two modes dissipatively, i.e., through a shared reservoir.

For a non-interacting two-mode system irradiated by a laser drive of Rabi frequency $\mathcal{E}$, the dynamics in the rotating frame of the input drive is underpinned by the Hamiltonian operator

$$\mathcal{H}/\hbar = \Delta_a a^\dagger a + \Delta_b b^\dagger b + i(\mathcal{E}a^\dagger - \mathcal{E}^* a), \tag{5.8}$$

where Δ_a and Δ_b denote the frequency detunings of the individual modes a and b relative to the

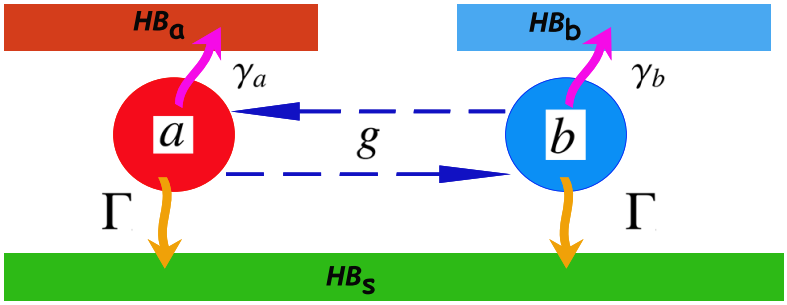

Figure 5.3: Schematic of a general two-mode system dissipatively coupled through a waveguide. $\gamma_{a(b)}$ and Γ describe decay into the surrounding (local heat bath) and coupling to the fiber (shared bath), respectively.

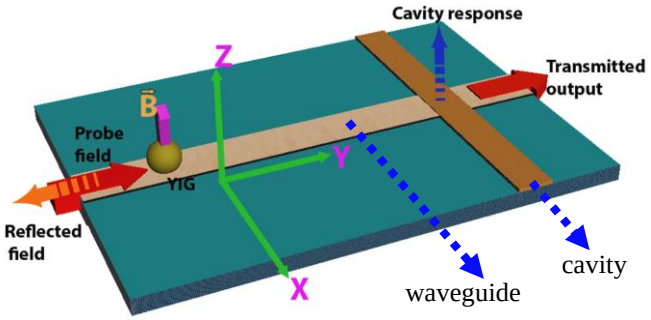

Figure 5.4: Schematic of a ferrimagnetic YIG sample interacting dissipatively with the transverse cavity, with the coupling mediated by an interposing microwave transmission line. YIG samples have frequencies in the microwave domain while Γ, γ are in the MHz range. (Redrawn from *Phys. Rev. Lett.* ***125****, 147202 (2020).*)

carrier frequency. In addition, if both the modes are interfacing with dissipative reservoirs, we can derive the master equation of the two modes as

$$\frac{\mathrm{d}\rho}{\mathrm{d}t} = -\frac{i}{\hbar}[\mathcal{H}_{eff}, \rho] + \kappa\mathcal{L}(a)\rho + \kappa\mathcal{L}(b)\rho + 2\Gamma\mathcal{L}(c)\rho, \tag{5.9}$$

where κ stands for the intrinsic damping rate of either of the modes into its local heat bath, $\mathcal{L}$ is

the Liouvillian operator defined by $\mathcal{L}(\alpha)\rho = 2\alpha\rho\alpha^\dagger - \alpha^\dagger\alpha\rho - \rho\alpha^\dagger\alpha$ for any annihilation operator α. The final term, with $c = \dfrac{1}{\sqrt{2}}(a+b)$ emerges due to dissipation from the two modes into a shared reservoir, such as a waveguide. Therefore, Γ quantifies the rate of spontaneous emission into the waveguide channel. This equation holds under the approximation that the phase delay due to light propagation from one mode to another is an integral multiple of 2π. The general master equation for an ensemble of arbitrary number of oscillators coupled to a shared bath is derived in Appendix B. Evaluating mean values of the mode operators $\langle a\rangle = \mathrm{Tr}(a\dot{\rho})$ and $\langle b\rangle = \mathrm{Tr}(b\dot{\rho})$, we obtain the dynamics

$$\begin{aligned}\dot{\langle a\rangle} &= -(i\Delta_a + \kappa + \Gamma)\langle a\rangle - \Gamma\langle b\rangle + \mathcal{E},\\ \dot{\langle b\rangle} &= -(i\Delta_b + \kappa + \Gamma)\langle b\rangle - \Gamma\langle a\rangle .\end{aligned} \tag{5.10}$$

We have dropped all quantum fluctuations at the mean-field level, i.e., set the averages of the noise terms to zero. On making the identification $\alpha_0 = \langle a\rangle$ and $\beta_0 = \langle b\rangle$, we recover a dynamical equation of the form 5.3. Additionally, on choosing $\Delta_a = -\Delta_b = \delta/2$, we obtain

$$H = \begin{pmatrix} \delta/2 - i(\kappa+\Gamma) & -i\Gamma \\ -i\Gamma & -\delta/2 - i(\kappa+\Gamma) \end{pmatrix}, \tag{5.11}$$

which fulfils the conditions for anti-PT symmetry. This shows how dissipative coupling can lead to an anti-PT symmetric effective Hamiltonian under an antisymmetric assignment of the mode detunings. In the forthcoming section, we dive into the subject of cavity magnonics and establish it as a useful test bed for probing the interesting signatures of dissipative coupling and anti-PT symmetry.

5.3 Cavity magnonics: a test bed for producing dissipative coupling

Of late, cavity magnonics has emerged as an important platform to implement many of the ideas from quantum optics and non-Hermitian physics. Magnetic systems are often more interesting to

study as one deals with the dynamical features of the collective spin excitations in macroscopic systems instead of a small cluster of qubits. The low-lying collective excitations in magnetically ordered materials have wave-like characteristics, as was demonstrated by Bloch in the context of ferromagnets. These waves are known as spin waves and they have quantized energies [132]. Just the quantum of vibrational energy is denoted as a phonon, an elementary excitation of a spin wave is represented as a quasiparticle called magnon. There are various types of magnon modes that typify a magnetic sample, however, we focus on a very special mode known as the Kittel mode, which describes a spatially homogeneous magnetic mode in the long-wavelength limit of a spin wave [133]. To understand the concept of this mode better, we first recall the classical picture of spin precession (also known as Larmor precession) in an external magnetic field. If a magnetic field is applied to a spin-system making an angle with the direction of spin, one observes a precession of the spin about the field axis. Now imagine we have a cluster of spins coupled through exchange interaction (typically, nearest-neighbor couplings) spread across space and an external magnetic field causes one of the spins to precess about the field direction. The exchange interaction subsequently distributes this precession amongst other spins, forming spin waves. In other words, any magnetic sample subjected to an external magnetic field which makes an angle with its magnetization would necessarily incur a precession in its magnetization due to a net torque acting on the same. In experiments, this is typically carried out by applying a small alternating magnetic field, which oscillates at a fixed frequency, to the magnetic sample. Now, there exists a unique mode, in which the individual spins are locked together resulting in all of these spins precessing in phase and with the same amplitude. Because of this in-phase coherent oscillation, the entire assemblage of spins can be mapped onto a large macroscopic spin, precessing as a giant magnetic dipole. This particular mode of precession, which is characterized by its spatially uniform magnetization density, is known as the ferromagnetic resonance (FMR) mode. In more popular parlance, this came to be known as the Kittel mode, named after Charles Kittel, who proposed the theory of FMR. The precession frequency of the Kittel mode in the presence of a

Quantities of interest	Experimental range	Units
Frequency of Kittel mode, $\omega_m = \gamma_e B_0$	1-10	GHz
Anharmonicity constant, U	$\mathcal{O}(0.01) - \mathcal{O}(10)$	nHz
Damping constant, $\gamma/(2\pi)$	1-10	MHz
Coherent magnon-photon coupling, $g/(2\pi)$	$50 - 100$	MHz
Dissipative magnon-photon coupling, $\Gamma/(2\pi)$	1-25	MHz

Table 5.1: Typical experimental parameters relevant to cavity magnonics, based on literature. The values shown are ballpark numbers.

static magnetic field B_0 is given, upto a good approximation, by

$$\omega_m \simeq \gamma_e B_0, \tag{5.12}$$

where $\gamma_e/(2\pi) = 28$ GHz/T is the gyromagnetic ratio of the electron spin. Therefore, for $B_0 \simeq 36$ mT, the resonance frequency is obtained as $\omega_m/(2\pi) = 1$ GHz, which makes this a good candidate for coupling to microwaves. Also, being spatially uniform, it is much simpler to model than other non-uniform modes.

Motivation to study cavity-magnonics: All said and done, it is perhaps more pertinent to address the real motivation in exploiting magnon-photon couplings. While there is an indispensable damping effect associated with the precession of magnetization, the losses are much lower than qubits or two-level atoms. Thus, magnonic excitations are fairly robust and the frequencies easily tunable. Moreover, these excitations can be observed at very low driving powers, even at fractions of a microwatt. A number of discretely spaced magnetostatic magnon modes are found in a magnetic sample, out of which the simplest is the Kittel mode. It is always possible to to selectively excite the homogeneous Kittel mode by judiciously tuning the carrier frequency and selecting the cavity mode most proximal to the Kittel mode. All of these in a magnetic sample afford a reliable paradigm for designing futuristic spintronic devices using magnon-photon couplings [134, 135].

Strong coupling of magnons to microwaves was first successfully demonstrated by Tabuchi *et al.* [136] and Zhang *et al.* [137] in 2014. They performed their experiments with spherical samples of YIG, which is a ferrimagnetic insulator and consequently suffers from low dissipation. Propitiously, YIG is endowed with very high spin density $\rho = 4.22 \times 10^{27}$ m^{-3}, with $s = \frac{5}{2}$ being the spin number of the ground state Fe^{3+} ion in YIG. With a value of $\rho = 4.22 \times 10^{27}$ m^{-3} for the Fe^{3+} ion density, and a diameter $d = 1$ mm of the spherical sample, the total spin becomes

$$S = s\rho V_m = 5.524 \times 10^{18}, \tag{5.13}$$

which is extremely high. Here, $V_m = \frac{4}{3}\pi\left(\frac{d}{2}\right)^3$ is the volume of the YIG. The quantity $\rho = 4.22 \times 10^{27}$ m^{-3} has been borrowed from literature [138, 139]; however, this could be even higher. In [136], the experimenters demonstrated mode splitting due to strong magnon-photon coupling of ~ 50 MHz, permitting a cooperativity of 3×10^3. The following year, in 2015, they were able to couple a superconducting qubit to magnons via microwave fields in a cavity [140]. The current state of the art allows even ultrastrong photon-magnon couplings to be achieved, which makes the study of magnon-photon interfaces particularly tempting [141]. This enables theory and experiment to proceed hand in hand, reliably guiding each other in their pursuits. YIG systems enable us to study various signatures of non-Hermitian physics like nonreciprocity, EPs, level attraction and repulsion [48, 99, 142–147].

In addition to semiclassical phenomena, several quantum features, like entanglement and squeezing, have also been proposed in such systems [138, 139, 148, 149]. The magneto-crystalline anisotropy of magnons leads to Kerr-like nonlinearity, familiar from nonlinear optics. The Kerr effect has been shown to be responsible for multistability and photon-mediated control of spin current [150–154]. Spherical samples of YIG with diameters ranging from $\sim 100\mu$m to 1 mm have been fabricated in a myriad of experiments, clearly underscoring the macroscopic sizes of the samples used. In light of the immense topicality of cavity magnonics, we have analyzed some of the general features of hybrid quantum systems using the master-equation approach, applying

them numerically to the context of cavity-magnonic systems. We have been particularly interested in the study of anti-PT symmetric systems, in which the magnons are dissipatively coupled to microwave fields (see Fig. 5.4). This type of coupling offers definite advantages over coherently coupled PT-symmetric systems in a number of physical problems, some of which we will expand on in the forthcoming chapters.

Quantization of magnons in a magnetic field: We now provide a quantum mechanical description of a YIG sphere subjected to a static, uniform magnetic field $\mathbf{B} = B_0\hat{z}$ applied along the $\hat{z}$ direction. Such a bias magnetic field enkindles the spatially uniform Kittel mode. The magnetization associated with the Kittel mode, which is the magnetic dipole moment per unit volume, can simply be written as $\mathbf{M} = \dfrac{\hbar\gamma_e\mathbf{S}}{V_m}$, where $\gamma_e = \dfrac{e}{m_e c}$ is the gyromagnetic ratio for electron spin, $\mathbf{S}$ denotes the collective spin operator, and V_m the volume of the YIG sphere. The collective spin variables represent spin angular momentum operators spanning the appropriate SU(2) Lie algebra, $[S_j, S_k] = i\varepsilon_{jkl}S_l$. We know that a spin $\mathbf{s}$ in a magnetic field attains a Hamiltonian $H_s = -\mathbf{m}\cdot\mathbf{B}$, where $\mathbf{m} = \hbar\gamma_e\mathbf{s}$ is the magnetic moment. For a macroscopic magnetic material, this expression generalizes to $H_M = -\int \mathbf{M}(\mathbf{r})\cdot\mathbf{B}(\mathbf{r})\,\mathrm{d}^3r$ in the magnetic dipole approximation. This is the usual Zeeman Hamiltonian. This approximation works pretty well in the long-wavelength limit of low-energy spin-waves, as exchange interactions between spins can be effectively subordinated in comparison to the dipolar effect. For the uniformly precessing Kittel mode with a space-invariant magnetization within the sample, this reduces to $H_M = -\hbar\gamma_e B_0 S_z$. Owing to the magnetocrystalline anisotropy, an additional anisotropic magnetic field $\mathbf{H}_{\text{an}}$ is entailed, which has only a non-zero z-component when the static magnetic field is aligned parallel to the crystallographic axis. This field is then given by $H_{\text{an}} = -2K_{\text{an}}M_z/M^2$, where K_{an} denotes the dominant first anisotropy constant, and M is the saturation magnetization. This anisotropic field shifts the Hamiltonian by an amount $H_M^{(\text{a.i})} = -\dfrac{\mu_0}{2}\int M_z(\mathbf{r})H_{\text{an}}(\mathbf{r})\mathrm{d}^3r = \gamma_e^2\dfrac{\hbar\mu_0 K_{\text{an}}}{M^2V}S_z^2$. Here, μ_0 is the magnetic permeability of the material. Summing up the two contributions, the Hamiltonian of the Kittel mode, in the

presence of an applied bias field, assumes the expression

$$H = H_M + H_M^{(\text{a.i})} = -\hbar\gamma_e B_0 S_z + \hbar^2\gamma_e^2 \frac{\mu_0 K_{\text{an}}}{M^2 V_m} S_z^2. \tag{5.14}$$

One can, thereafter, diagonalize this Hamiltonian in the simultaneous eigenspace of S^2 and S_z. However, since the total spin is very large, one can obtain a Bosonic representation of the Kittel mode operators via the Holstein-Primakoff transformation, *viz.*

$$\begin{aligned} S_z &\simeq S - m^\dagger m, \\ S^+ &\simeq \sqrt{2S}\left(1 - \frac{m^\dagger m}{2S}\right)^{1/2} m, \\ S^- &\simeq \sqrt{2S}\left(1 - \frac{m^\dagger m}{2S}\right)^{1/2} m^\dagger. \end{aligned} \tag{5.15}$$

Note that the magnon creation operator $m^\dagger$ corresponds to deexcitation of the spin state, or the down-flipping of any one of the constituent spins. For a typical YIG sphere, $S \sim 10^{18}$, which far exceeds the mean magnon number $\left\langle m^\dagger m \right\rangle$ achievable in the space of low-lying excitations. It is then safe to approximate the spin raising and lower operators as $S^+ \simeq \sqrt{2S}m$ and $S^- \simeq \sqrt{2S}m^\dagger$. Armed with these simplifications, we can recast the Hamiltonian in Eq. () into

$$H/\hbar = (\omega_m + U)m^\dagger m + U(m^{\dagger 2} m^2), \tag{5.16}$$

where $\omega_m = \gamma_e B_0 - \dfrac{2S\hbar\mu_0\gamma_e^2 K_{\text{an}}}{M^2 V_m}$, $U = \dfrac{\hbar\mu_0\gamma_e^2 K_{\text{an}}}{M^2 V_m}$. Now, while ω_m is of the order of GHz, the anharmonicity constant U relevant to YIGs lies in the nanoscale regime (see, for instance, [150, 155]) and therefore, as a frequency, it is around 18 orders of magnitude smaller than ω_m. This facilitates the further approximation $\omega_m + U \simeq \omega_m$. But we cannot afford to be flippant by approximating $\omega_m = \gamma_e B_0 - 2SU \simeq \gamma_e B_0$. This particular approximation would make sense only when U is the sub-nHz domain, i.e., $U \lesssim 0.1$ nHz, which often happens to be the case.

Nevertheless, quite generally, the Hamiltonian can be expressed as

$$H/\hbar = \omega_m m^\dagger m + U(m^{\dagger 2} m^2), \tag{5.17}$$

where the second term, resulting from magnetocrystalline anisotropy, embodies the Kerr nonlinearity in the sample.

Hamiltonian of coherent interaction with a microcavity: We first consider a YIG sphere wedged inside a microwave cavity so that the Kittel mode can be coupled efficiently to the intracavity field. Strong coupling can be achieved via the Purcell effect. The Hamiltonian of the cavity mode is obtained in the usual harmonic oscillator form, i.e.,

$$H_c = \frac{1}{2}\int_{V_a}\left(\varepsilon_0 \mathbf{E}^2 + \frac{\mathbf{B}^2}{\mu_0}\right)\mathrm{d}^3 r \simeq \hbar\omega_a a^\dagger a, \tag{5.18}$$

where V_a is the quantization volume of the cavity and ω_c is the resonant cavity-mode frequency. The magnetic field $\mathbf{B}$, assumed to be along the x-axis, would also coherently interact with the magnetization of the Kittel mode, leading to the Hamiltonian

$$H_{\text{coherent}} = -\int_{V_m} \mathbf{M}\cdot\mathbf{B}\ \mathrm{d}^3 r = -\frac{\hbar\gamma_e S_x}{V_m}\int_{V_m} B_x(\mathbf{r})\mathrm{d}^{\mathbf{3}}\mathbf{r} \tag{5.19}$$

where $S_x = \dfrac{S_+ + S_-}{2} \simeq \sqrt{\dfrac{S}{2}}(m + m^\dagger)$ and $B_x(\mathbf{r}) = i\sqrt{\dfrac{\mu_0\hbar\omega_a}{2V_a}}u(\mathbf{r})a + \text{h.c.}$ are both quantized operators. The integral is taken over the volume of the YIG since the magnetization is confined only within this volume. The parameter V_a symbolizes the volume of the cavity and $u(\mathbf{r})$ designates the relevant mode function normalized as $\int_{V_a}|u(\mathbf{r})|\mathrm{d}^3 r = V_a$. Substituting these expressions into (5.17), we find

$$H_{\text{coherent}} = -i\frac{\hbar\gamma_e}{4}\sqrt{\frac{5\rho\mu_0\hbar\omega_a}{V_a V_m}}\left(\eta a + \eta^* a^\dagger\right)\left(m + m^\dagger\right) \tag{5.20}$$

with the constant η defined as $\eta = \int_{V_m} u(\mathbf{r})\mathrm{d}^3\mathbf{r}$[‡]. Under the RWA, this expression reduces to $H_{\text{coherent}} = \hbar(gam^\dagger + g^* a^\dagger m)$, with the coupling constant $g = -i\frac{\gamma_e}{4}\sqrt{\frac{5\rho\mu_0\hbar\omega_a}{V_a V_m}}\eta$. In any case, we can always absorb the phase factor associated with g into a redefined magnon operator and treat g as a real variable, which simplifies (5.20) as

$$H_{\text{coherent}} = \hbar g(am^\dagger + a^\dagger m) \tag{5.21}$$

This kind of interaction is referred to as coherent coupling between a and m since it is established through the direct exchange of energy between magnons and photons. It is easy to see that the total excitation number $\hat{N}_a + \hat{N}_m = a^\dagger a + m^\dagger m$ is preserved by this coupling, as $[a^\dagger a + m^\dagger m, H_{\text{coherent}}] = 0$ and therefore, energy is transferred back and forth between the cavity and the magnon modes in an oscillatory fashion. These oscillations are known very well as Rabi oscillations. Stated alternatively, there exists an oscillatory coherence between the singly-excited-magnon state and the singly-excited-cavity state. So the nature of this Hamiltonian is exactly similar to the Jaynes-Cummings model of a 2LA interacting with an EM field.

Effect of a coherent microwave drive with magnetic field along $\hat{y}$ direction: We next consider the scenario when the Kittel mode is driven externally by a classical driving field $\mathbf{B}_d(t) = \mathcal{B}_d \cos(\omega_d t)\hat{y} = \frac{\mathcal{B}_d}{2}(e^{i\omega_d t} + e^{-i\omega_d t})\hat{y}$. The interaction Hamiltonian would be given by

$$H_d = -\int \mathbf{M}\cdot\mathbf{B}_d \,\mathrm{d}^3 r = \frac{i\hbar\gamma_e\mathcal{B}_d}{4}\sqrt{5\rho V_m}\left(e^{i\omega_d t} + e^{-i\omega_d t}\right)(m - m^\dagger), \tag{5.22}$$

which, on account of the RWA, yields

$$H_d = i\hbar\Omega(me^{i\omega_d t} - m^\dagger e^{-i\omega_d t}), \tag{5.23}$$

[‡]More generally, for a spatially non-uniform mode, this would be the overlap-integral between the magnetization and field mode functions.

where $\Omega = \gamma_e \mathcal{B}_d \frac{\sqrt{5\rho V_m}}{4}$ is the associated Rabi frequency. We would, however, like to connect this to the input power of the driving field. For this, we need to calculate the Poynting vector pertaining to the drive. The time-averaged magnitude of this Poynting vector can be expressed in SI units as $\frac{c\mathcal{B}_d^2}{2\mu_0}$, where c stands for the speed of light. Since this is just the power imparted per unit area of the target, the input power would be given approximately by $D_p \simeq \frac{c\mathcal{B}_d^2}{2\mu_0}.\frac{\pi d^2}{4}$, where d is the diameter of the YIG sphere. This allows us to rewrite the Rabi frequency in terms of the incident power and the system parameters:

$$\Omega = \frac{\gamma_e}{2}\sqrt{\frac{5\mu_0 \rho d D_{\mathrm{p}}}{3c}}. \tag{5.24}$$

So finally, when we combine all the contributions, we find the full Hamiltonian of the cavity-magnonic composite system as

$$H_{\mathrm{eff}}/\hbar = \omega_a a^\dagger a + \omega_m m^\dagger m + +U(m^{\dagger 2} m^2) + g(a^\dagger m + a m^\dagger) + i\hbar\Omega\left(m^\dagger e^{-i\omega_{\mathrm{d}} t} - m e^{i\omega_{\mathrm{d}} t}\right). \tag{5.25}$$

Dissipatively coupled cavity-magnon system: Here, we would like to address the following: what if, instead of placing the YIG inside a resonator, we couple the YIG and the resonator to a shared waveguide and keep a spatial separation between the two elements? This the precise setup that was illustrated in Fig. 5.4 and was based on the experimental model proposed by Wang *et al.* - an integrated apparatus comprising a bulk YIG sphere, coupled dissipatively to a single-mode cavity through an interposing fiber waveguide. In the experiment, they kept the spatial separation between the cavity and the YIG adequately large, so as to minimize any direct interaction between the two. Additionally, a protective shield was used around the YIG which further mitigated the chances of coherent couplings. The Hamiltonian of this model is exactly the same as before, with only g *now set equal to zero*. The dissipative effect of the waveguide has to be incorporated at the level of a master equation, as argued before. In the rotating frame of the drive frequency, this

results in the following mean-value equations

$$\begin{pmatrix} \dot{a} \\ \dot{b} \end{pmatrix} = -iH \begin{pmatrix} a \\ b \end{pmatrix} + 2U(b^{\dagger}b)N \begin{pmatrix} a \\ b \end{pmatrix} + \Omega \begin{pmatrix} 0 \\ 1 \end{pmatrix}, \tag{5.26}$$

where $H = \begin{pmatrix} \Delta_a - i(\gamma_a + \Gamma) & -i\Gamma \\ -i\Gamma & \Delta_b - i(\gamma_b + \Gamma) \end{pmatrix}$, $N = \begin{pmatrix} 0 & 0 \\ 0 & 1 \end{pmatrix}$, and the notation $\langle . \rangle$ has been dropped for conciseness. In dealing with the nonlinear term, we have taken recourse to the mean-field approximation $\langle \mathcal{X}_1 \mathcal{X}_2 \rangle = \langle \mathcal{X}_1 \rangle \langle \mathcal{X}_2 \rangle$ for any two operators $\mathcal{X}_1$ and $\mathcal{X}_2$. When one ignores the effect U, then under pertinent choices of the system parameters, i.e., $\gamma_a = \gamma_b = \gamma_0$ and $\Delta_a = -\Delta_b = \dfrac{\delta}{2}$, an effective anti-PT symmetric Hamiltonian as derived in Eq. 5.11 can be used to describe the system. Anti-PT symmetry was first experimentally demonstrated in a cavity-magnonic setting by C. M. Hu's group [48]. Throughout the next two chapters, we would focus *primarily on anti-PT symmetric systems*, and base our numerical analyses on *cavity-magnonic setups*, which are finding considerable attention in the experimental optics and solid-state community. But before we move on to explore the significance of such systems, we briefly allude to an alternative method of generating dissipative coupling, which is mediated between two non-interacting magnon modes by a bad-quality cavity, i.e., having a high leakage rate.

5.4 Dissipative coupling and anti-PT symmetry in a poor cavity

We have just shown that dissipative coupling between a cavity and a magnetic sample by coupling them evanescently to a waveguide can lead to anti-PT symmetry. Here, we delineate an alternate protocol for bringing about the same symmetry in a cavity QED framework. In this model, we envisage a hybrid cavity-magnonic system, with two macroscopic YIG samples placed inside a microwave cavity, as illustrated in Fig. 5.5. We consider the spatially uniform Kittel mode of either YIG as being dispersively coupled to the intracavity photons of a neighboring frequency. To simplify our analysis, we assume the YIG samples to be identical in all respects. The Hamiltonian

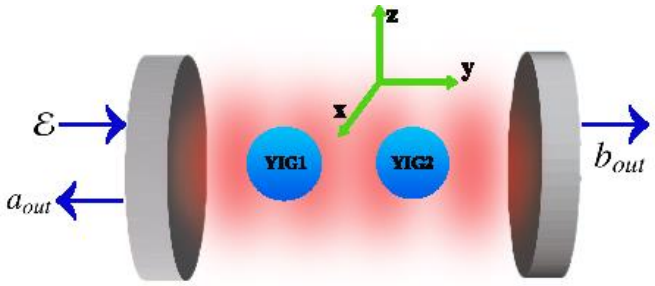

Figure 5.5: Schematic of two YIGs coherently coupled to a single-mode microwave cavity. The static magnetic field exciting the Kittel mode in both the YIGs are aligned along the z-axis. The intracavity field mode is propagating along the y-axis, with the corresponding magnetic field directed along the x-axis.

of the hybrid magnon-cavity system is then provided by

$$H/\hbar = \omega_a a^\dagger a + \sum_{i=1}^{2} \left[\omega m_i^\dagger m_i + g(m_i^\dagger a + m_i a^\dagger)\right] \tag{5.27}$$

The parameter $g_i = \dfrac{\sqrt{5}}{2}\gamma_e\sqrt{\rho V_m}B_{\text{vac}}$ quantifies the coherent magnon-cavity coupling, with $B_{\text{vac}} = \sqrt{\dfrac{\mu_0\hbar\omega_a}{2V_a}}$ denoting the magnetic field amplitude of vacuum. In the frame rotating at frequency ω_a, the Heisenberg equations of motion can be cast in the form $\dot{X} = -i\mathcal{H}X$, where where $X = (\langle a\rangle \quad \langle m_1\rangle \quad \langle m_2\rangle)^T$, and the effective non-Hermitian Hamiltonian describing the system dynamics is provided by

$$\mathcal{H} = \begin{pmatrix} -i\kappa & g_1 & g_2 \\ g_1 & s - i\gamma_1 & 0 \\ g_2 & 0 & -s - i\gamma_2 \end{pmatrix}. \tag{5.28}$$

Here, we have set $\omega_a = (\omega_{m_1} + \omega_{m_2})/2$ (thus, the magnons are antisymmetrically detuned relative to the cavity frequency) and defined $s = (\omega_{m_1} - \omega_{m_2})/2$. The parameters κ and γ_i denote the rates of dissipation appearing in the master equation. The normal modes of the hybridized system are referred to as polaritons. For convenience, we now assume that the coupling strengths

are identical, i.e., $g_1 = g_2 = g$ and so are the magnon damping rates, i.e., $\gamma_1 = \gamma_2 = \gamma$. When the cavity is weakly coupled to the magnon modes ($g \ll \kappa$) and the photons decay over a much shorter time scale than the magnons ($\gamma \ll \kappa$), we can observe signatures of level crossing between the magnon-like polaritons. To see this, we consider the characteristic equation for H by neglecting the effect of γ in reference to κ:

$$(\lambda + i\kappa)(\lambda^2 - s^2) - 2g^2\lambda = 0. \tag{5.29}$$

Since the eigenvalues in the absence of g equal $\lambda_0 = -i\kappa$, and $\lambda_\pm = \pm s$, it can be argued that the perturbative correction to each of them for sufficiently small g would go as $\mathcal{O}(g^2)$. This consideration pins down the approximate form of λ_0 to be $-i\kappa[1 - 2g^2/(s^2 + \kappa^2)]$. Next, in view of the fact that both s and g are small compared to κ, we approximate $\lambda_\pm + i\kappa \approx i\kappa$, which permits the reduction of the cubic equation into a quadratic one $\lambda_\pm^2 + 2\Gamma\lambda_\pm i - s^2 \approx 0$, where $\Gamma = g^2/\kappa$. This yields the remaining eigenvalues

$$\lambda_\pm = -i\Gamma \pm i\sqrt{\Gamma^2 - s^2}. \tag{5.30}$$

The forms of $\lambda_\pm$ are strongly redolent of the eigenspectrum of an anti-PT symmetric system, with EPs located at $s = \Gamma$. We can extract spectroscopic information about the system by applying an external probe, which renders an empirical tool to observe this level crossing[§]. The onset of level crossing in this regime points to a hidden dissipative interaction between the magnon modes [147]. This is proved rigorously in Appendix C.

5.5 Summary

Non-Hermitian effective Hamiltonians are useful in describing open quantum systems which exchange energy with their surroundings. We have introduced two exotic symmetries in non-

[§]Details on the derivation can be found out in our paper (Phys. Rev. B. **105**, 214418 (2022)) and are beyond the scope of this thesis.

Hermitian systems, *PT-symmetry* and *anti-PT symmetry*, with a special focus on the latter. Anti-PT symmetry can be realized in various optical systems of interest, with a reservoir-mediated *purely dissipative coupling* forming the mainstay of this symmetry. Guided by recent experiments on cavity magnonics, we have pick these systems as a useful and emergent test bed for probing dissipative couplings. We have presented a detailed, first-principle description for analyzing magnon-photon interactions in the quantum mechanical formalism. We have also brought to light the feasibility of engineering dissipative coupling between two magnons coupled to a single-mode cavity, by manipulating the relaxation rates and the magnon-photon coupling strengths. Specifically, this feature transpires in the bad-cavity regime of cavity QED.

6. SENSING OF ANHARMONICITIES THROUGH ANTI-PT SYMMETRY*

In the modern world with proliferating technological advances, sensing is of fundamental importance, with far-reaching applications [156–162] across various scientific disciplines, with adoptions as particle sensors, motion sensors, and more. Both semiclassical and quantum phenomena provide us with a wide range of techniques to attain remarkable efficacy in sensing operations. In recent times, there has been a widespread interest in exploiting EPs for enhanced sensing. The square-root singularity of an EP reinforces the sensitivity in eigenmode splitting to weak perturbations [111–113, 163–167]. Some recent experiments include the demonstration of enhanced sensitivity in optical microcavities near EPs [111] and the observation of higher-order EPs in a coupled-cavity arrangement [112]. While this is a truly remarkable development and has acquired a lot of traction, these methodologies are customized to sense only linear perturbations. One would like to examine the possibilities of newer sensing techniques, which could be tapped for the detection of anharmonic perturbations. However, many systems like transmon qubits and magnons have intrinsic anharmonicities which are too small to detect and consequently, ignored. We took the first step in the direction of sensing nonlinear perturbations in driven dissipative systems, by exploiting the phenomenon of VIC [168].

Dissipatively coupled systems have the novel property that the vacuum field inside a shared reservoir induces coherence between two modes. The phenomenon of vacuum induced coherence (VIC) has been the subject of intense activity [169–181] with applications ranging from heat engines [173] and nuclear gamma ray transmission [178] to photosynthesis [179] and molecular isomerization in vision [181]. When optimally strong, under *anti-PT symmetric conditions*, the VIC produces a long-lived eigenmode, thereby stirring up a strong response to an external pump. The response is starkly sensitive to the strength of anharmonicity, which underscores its sensing

*A major portion of this chapter is reprinted with permission from *Enhanced Sensing of Weak Anharmonicities through Coherences in Dissipatively Coupled Anti-PT Symmetric Systems* by J. M. P. Nair, D. Mukhopadhyay, and G. S. Agarwal, Phys. Rev. Lett. **126**, 180401 (2021), published by the American Physical Society. Sec. 6.3 is reprinted with permission from Phys. Rev. Res. **4**, 013131 (2022). Respective collaborations with J. M. P. Nair and J. Wang are acknowledged.

capabilities. This is achieved in anti-PT symmetric systems. Our sensing methodology operates near the quasi-real singularity of an anti-PT symmetric system where VIC creates a divergent linear response. Any intrinsic anharmonicity serves to regularize this response. More importantly, the steady-state response is starkly sensitive to the strength of anharmonicity, which underscores its sensing capabilities. Contextualized in a cavity-magnonic setting, our simulations illustrate the efficient detection of magnonic anharmonicity through the application of a maser pump at a minuscule power of $D_p = 1$ W. Note that under most circumstances, weak nonlinearities of the order of nHZ would require immense drive power to be detected in experiments. However, a dissipatively coupled system affords a prodigious response in the magnetization of the YIG which goes up spectacularly with the weakening strength of nonlinearity. That this response is strongly sensitive to variations in the strength of anhamonicity underpins the utility of our scheme in sensing applications. This new mechanism is applicable generally to a large class of systems encountered across various scientific disciplines. Examples include quantum emitters coupled to metamaterials [169–171], optomechanical systems [98], superconducting transmon qubits in a microwave transmission line [182], and many more.

The chapter is organized as follows. In section 6.1, we briefly recapitulate the mechanism for sensing weak linear perturbations around an EP. We subsequently discuss, in Sec. 6.2, the role of VIC in an anti-PT symmetric system by enhancing sensitivity to perturbations around the VIC point. Following this, we highlight its potential in sensing linear perturbations in Sec. 6.3, an weak anharmonicities in 6.4. Results from numerical simulations are shown in the specific context of cavity magnonics. For driven nonlinear systems, new VIC-like effects emerge, which we bring out in Sec. 6.5. The main results are summed up and presented in 6.6.

6.1 Sensing of linear perturbations at EP

Singularities in a physical system are extremely critical points which wield tremendous influence on the characteristics of the system, particularly related to phase transition. Owing to the pronounced impact of singularities, the behavior of a system is of a fundamentally different nature

compared to the neighboring points. This property is directly responsible for creating opportunities for ultrasensitive measurements around a singular point, as borne out by a range of recent theoretical and experimental works. An interesting category of sensors deployed in physics is based on the detection of splittings in the resonant frequencies or energy levels to external perturbations. Examples would be nanomechanical mass sensors [156], magnetic field sensors [161] and optical gyroscopes [162]. A degeneracy of resonant modes can function as the cardinal element of a sensor because any tiny perturbation to the system serves to break the multiplicity of eigenfrequencies. The role of a sensor is then to probe the splitting effect. Conventionally, for closed, conservative systems, a minute perturbation of strength ε leads to spectral splitting in the resonance frequencies linearly proportional to ε, which admittedly is itself comparably weak[†]. This behavior drastically changes for open systems which are non-conservative. Since these systems are described by an effective non-Hermitian Hamiltonian, the corresponding degeneracies appear as EPs, where not only the eigenvalues coincide but so do the corresponding eigenvalues. For example, if a system prepared at an EP is subjected to a perturbation of strength ε then the resulting energy splitting is typically proportional to $\varepsilon^{1/2}$ (see Fig. 6.1(a,b)). In other words, for a sufficiently small ε, the strength of the spectral splitting is enhanced compared to the strength of the perturbing influence. This feature owes its origin to the branch-point singularity at an EP, and lends enhanced sensitivity to feeble perturbations. The exciting potential of EP-based sensors was first brought to the fore through the ingenuity of J. Wiersig, when he theoretically analyzed its application to single-particle detection in microcavity sensors. We briefly review the underlying theory here.

Let us consider a 2×2 matrix $M(\mu)$ as a function as a function of a tunable (and generally complex) parameter μ. To keep the analysis general, we do not specify the elements of the matrix. Now, upon solving the characteristic polynomial equation, the eigenvalues of $M(\mu)$ can be expressed in the form

$$\lambda_{\pm}(\mu) = \eta \pm \sqrt{(\mu - \mu_{+})(\mu - \mu_{-})}, \tag{6.1}$$

[†]Degeneracy points in Hermitian are also known as DPs, as was defined in Sec. 5.2 of Chapter 5.

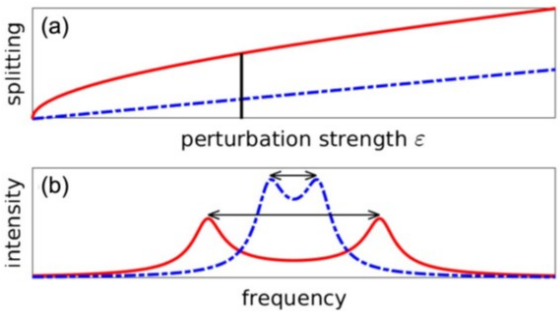

Figure 6.1: Normal-mode splitting (a) and (b) intensity-peak-shift in response to a weak perturbation. Blue curve corresponds to the performance at a DP (hermitian degeneracy) while red curve at an EP. (Adapted from *Photon. Res.* ***8****, 1457-1467 (2020)*, published as open access by the Optica Publishing Group.)

where $\eta = \frac{1}{2}\operatorname{Tr} M$ and $\mu_\pm$ represent two well-separated EPs of the system. Then $\lambda_\pm(\mu)$ have branch-point singularities at $\mu = \mu_\pm$. At any of these EPs, the eigenvalues become degenerate, i.e., $\lambda(\mu_\pm) = \eta$. Let us now consider the splitting defined by $\delta\Omega(\mu) = 2\operatorname{Re}(\lambda_+(\mu) - \lambda_-(\mu)) = 2\sqrt{(\mu-\mu_+)(\mu-\mu_-)}$. For a tiny perturbation at the EP μ_+, i.e., $\mu = \mu_+ + \delta\mu$, the splitting can be written, up to leading order in the perturbation parameter, as

$$\delta\Omega\Big|_{\mu=\mu+} \simeq 2\sqrt{\delta\mu}\sqrt{\mu_+ - \mu_-} \tag{6.2}$$

Thus, the sensitivity around the EP can be encoded as

$$\frac{\delta\Omega(\mu)}{\delta\mu}\Big|_{\mu=\mu_+} \simeq \frac{\sqrt{\mu_+ - \mu_-}}{\sqrt{\delta\mu}} \propto \frac{1}{\sqrt{\delta\mu}} \tag{6.3}$$

showing that the derivative function diverges at the EP. In contrast, if the system did not have a square-root singularity at μ_+, the corresponding derivative function would be a constant, independent of the perturbation. Consequently, applying the same idea to the effective Hamiltonian of an open systems affords a sensing scheme for detecting weak perturbations that induce a splitting in the eigenmodes. As ridiculously simple an idea this might sound, the fact that this was conceived only a few years back shows how nature has a habit of concealing elegant ideas in plain sight. In a

fairly recent paper, however, Wiersig himself has acknowledged the indelible impact of quantum-limited intensity noise on EP-based sensing protocols [183]. Nevertheless, the sensing scheme is already a success story, and research on this subject continues to burgeon.

6.2 VIC and the emergence of a long-lived mode

The concept of VIC was briefly introduced in the previous chapter. Here, we provide a mathematical analysis showing how VIC can be advantageous to the sensing of perturbations in anti-PT symmetric systems. Unlike the EP, the singularity used in this sensing scheme is not one that is inherent to the splitting of spectral frequencies. Rather, our sensing mechanism exploits the vanishing spectral linewidth of an eigenmode, which makes the linear response function strongly peaked at the corresponding resonance. We shall demonstrate the great utility of this key property to the sensing of extremely weak nonlinearities which are, otherwise, difficult to detect. We start off by considering the general model for a two-mode anharmonic system, which is pertinent to a wide range of physical systems. This is characterized by a Hamiltonian

$$\mathcal{H}_{ab}/\hbar = \omega_a a^\dagger a + \omega_b b^\dagger b + g(ab^\dagger + a^\dagger b) + U(b^{\dagger 2} b^2) - i\Omega(be^{-i\omega_d t} - b^\dagger e^{i\omega_d t}), \tag{6.4}$$

where ω_a and ω_b denote the respective resonance frequencies of the uncoupled modes a and b, and g constitutes the coherent hermitian coupling between them. The meanings of the various parameters were introduced in the preceding chapter. If the two modes are coupled dissipatively, $g = 0$, and the mean value equations for a and b are obtained in the rotating frame of the drive as

$$\begin{pmatrix} \dot{a} \\ \dot{b} \end{pmatrix} = -iH \begin{pmatrix} a \\ b \end{pmatrix} + 2U(b^\dagger b)N \begin{pmatrix} a \\ b \end{pmatrix} + \Omega \begin{pmatrix} 0 \\ 1 \end{pmatrix}, \tag{6.5}$$

where $H = \begin{pmatrix} \Delta_a - i(\gamma_a + \Gamma) & -i\Gamma \\ -i\Gamma & \Delta_b - i(\gamma_b + \Gamma) \end{pmatrix}$, and $N = \begin{pmatrix} 0 & 0 \\ 0 & 1 \end{pmatrix}$. This assumes the spatial separation between the two modes satisfies $kL = n\pi$. Before proceeding with a generalized treatment, let us first deconstruct the linear dynamics, i.e., when $U = 0$. Subject to the fulfillment of the stability criterion, *viz.* $\gamma > \Gamma$, so that both eigenmodes decay in time, the steady state of the system can solved by setting $\dot{a} = \dot{b} = 0$. We assume that $\Delta_a = -\Delta_b = \dfrac{\delta}{2}$, $\gamma_a = \gamma_b = \gamma_0$ so as to satisfy anti-PT symmetry. For these parameters, the system reduces to a steady state $\lim_{t\to\infty} \langle a(t) \rangle = \alpha_0$, $\lim_{t\to\infty} \langle b(t) \rangle = \beta_0$ in the long-time limit, yielding the solutions

$$\begin{aligned} \alpha_0 &= -i\frac{H_{22}}{\det H}\Omega = -\frac{\gamma - i\Delta}{\Gamma^2 - \Delta^2 - \gamma^2}\Omega, \\ \beta_0 &= i\frac{H_{21}}{\det H}\Omega = \frac{\Gamma}{\Gamma^2 - \Delta^2 - \gamma^2}\Omega, \end{aligned} \tag{6.6}$$

with $\gamma = \gamma_0 + \Gamma$ epitomizing the total relaxation rate of each individual mode. It follows from these expressions that the PT unbroken phase brings in a real singularity in the linear response at $= 0$ in the limit $\Gamma \to \gamma$. This is evidenced by the resonant inhibition in the imaginary part of λ_+, as marked by the point X in Fig. 5.1(b), Chapter 5. We have referred to this as the VIC point in our system. This can be understood from a thorough analysis in terms of the eigenmodes of the system. In this limit, the two eigenvalues reduce to $\lambda_+ = 0$ and $\lambda_- = -2i\Gamma$. The former represents a non-dissipative dark mode. Denoting the corresponding eigenfunctions as ψ_+ and ψ_-, we find that the first eigenfunction never decays in time while the other eigenfunction is rapidly flushed out over a timescale of $\sim \dfrac{1}{2\Gamma}$. The transient dynamics is then dominated by the ψ_+-mode. What about the steady-state behavior *near the VIC point*, i.e. as $\delta \to 0$, $\Gamma \to \gamma$? If a system starts out in the initial state $\psi(0) = \begin{pmatrix} a(0) \\ b(0) \end{pmatrix} = c_+\psi_+ + c_-\psi_-$, where $c_\pm$ are complex amplitudes, in the

long-time limit, the system evolves into

$$\begin{aligned}\lim_{t\to\infty}\psi(t) &= c_+\lim_{t\to\infty}\underbrace{e^{-i\lambda_+ t}\psi_+}_{\text{decays very slowly}} + c_-\lim_{t\to\infty}\underbrace{e^{-i\lambda_- t}\psi_-}_{\text{rapidly decays away}} + \Omega\lim_{t\to\infty}\int_0^t e^{-iH(t-t')}\mathrm{d}t'\begin{pmatrix}0\\1\end{pmatrix}\\ &= -i\Omega H^{-1}\begin{pmatrix}0\\1\end{pmatrix},\\ &\to\infty. \end{aligned} \tag{6.7}$$

where the penultimate inequality follows from expanding the exponential on the third term in a Taylor series, yielding

$$\int_0^t e^{-iH(t-t')}\mathrm{d}t' = iH^{-1}\Big[e^{-iH(t-t')}-1\Big], \tag{6.8}$$

and eventually taking the limit $t\to\infty$[‡]. The final equality in (6.7) follows from the relation $\det H\to 0$ as the VIC point is approached, since $\det H=\lambda_+\lambda_-$, and $\lambda_+\to 0$. However, it ought to be borne in mind that all these results pertain to the frame of the carrier frequency. Since the eigenvalues in the original frame are related to those in the rotated frame by simple shift of frequencies, the VIC point in the original frame can be identified generally by the condition $\mathrm{Im}(\lambda_+^{(\text{original})})=0$, where $\lambda_+^{(\text{original})}$ now refers to the non-decaying eigenmode calculated in the original frame.

6.3 Application of VIC to the sensing of linear perturbations

Before we explicate the sensitivity in nonlinear systems, we consider the application of VIC to sensing ordinary weak perturbations. In realistic scenarios, there would always be some discord with the watertight conditions of anti-PT symmetry, no matter how small the error can be made. In

[‡]Note that the limit of $e^{-iH(t-t')}$ can be rigorously derived by appealing to its biorthogonal decomposition, which is a generalization of orthonormal decomposition relevant to non-Hermitian systems. Since the eigenvalues have decaying character, it follows that this function vanishes in the long-time limit.

Sec. 6.2, we derived the mode amplitudes ensuing in the steady state of the linear system. Since the amplitudes are proportional to Ω and sensitive to the system parameters (Δ, γ, Γ), the application of a probe field yields nonzero values of the derivatives $\dfrac{\partial(\alpha_0, \beta_0)}{\partial(\Delta, \gamma, \Gamma)}$. This gives us a way of sensing any small perturbations to these parameters. Let us consider, for instance, the particular case when one of the frequency detunings is zero but there is only a small mismatch in the magnitudes of the two detunings, i.e., $H_{11} = -i\gamma$ and $H_{22} = -s - i\gamma$, where s is a small parameter. One could get an estimate of this mismatch by measuring the complex amplitudes

$$\alpha_0(s) = -\frac{\gamma - is}{\Gamma^2 + is\gamma - \gamma^2}\Omega, \quad \beta_0(s) = \frac{\Gamma}{\Gamma^2 + is\gamma - \gamma^2}\Omega. \tag{6.9}$$

The pertinent sensitivities could, then, be obtained in terms of

$$\frac{\partial\alpha_0(s)}{\partial s} = \frac{i\Gamma^2}{(\Gamma^2 + is\gamma - \gamma^2)^2}\Omega, \quad \frac{\partial\beta_0(s)}{\partial s} = \frac{-i\Gamma\gamma}{(\Gamma^2 + is\gamma - \gamma^2)^2}\Omega. \tag{6.10}$$

Supposing that $\gamma = (1 + \xi)\Gamma$ for $\xi \ll 1$, both the derivatives would scale as $\dfrac{1}{s^2}$, if $\xi \ll \dfrac{s}{\Gamma}$. This would imply an augmented sensing capability around this point. Alternatively, there could be some weak dispersive coupling between a and b, which modifies the off-diagonal terms in H into $H_{12} = H_{21} = g - i\Gamma$, where $g \ll \Gamma$. An example of this case from integrated photonics would be a string of two dipolar emitters embedded onto a waveguide and separated by a distance that is scale-wise similar to the resonant wavelength. Following the same approach as above, we can compute the corresponding sensitivities as

$$\frac{\partial\alpha_0(g)}{\partial g} = 2i\frac{(\Gamma + ig)(\gamma - i\Delta)}{[(\Gamma + ig)^2 - \Delta^2 - \gamma^2]^2}\Omega, \quad \frac{\partial\beta_0(g)}{\partial g} = -i\frac{(\Gamma + ig)^2 + \Delta^2 + \gamma^2}{[(\Gamma + ig)^2 - \Delta^2 - \gamma^2]^2}\Omega. \tag{6.11}$$

Once again, for $\xi \ll \dfrac{g}{\Gamma}$, the derivatives scale as $\dfrac{1}{g^2}$ in the limit $\Delta \to 0$.

6.4 Sensitivity in the nonlinear response of a cavity-magnonic system

Next, we illustrate the importance of the VIC point in the context of the nonlinear response observed in the system [168]. It is found that the nonlinear behavior depends on the intrinsic symmetry properties of the matrix H. Specifically, the extraordinary response achievable in anti-PT symmetric models yields a convenient protocol for the fine-grained estimation of weak anharmonicity. We now consider a full treatment of Eq. (6.5) by factoring in the effect of U. In the rotating frame, upon setting $g = 0$ and choosing $\gamma_a = \gamma_b = \gamma_0$, this leads to the modified steady-state relations:

$$\begin{aligned} -(i\delta/2 + \gamma_0 + \Gamma)a - \Gamma b = 0, \\ -(-i\delta/2 + \gamma_0 + \Gamma)b - 2iU|b|^2 b - \Gamma a + \Omega = 0. \end{aligned} \tag{6.12}$$

Defining $\gamma = \gamma_0 + \Gamma$ and eliminating a, the intensity $x = |b|^2$ is found to satisfy a cubic relation

$$\frac{\beta^2}{\gamma^2 + (\delta/2)^2} x - \frac{2U\beta\delta}{\gamma^2 + (\delta/2)^2} x^2 + 4U^2 x^3 = I, \tag{6.13}$$

where $\beta = \Gamma^2 - \gamma^2 - (\delta/2)^2$ and $I = \Omega^2$. Eq. (6.13) can entail a bistable response under the condition $U\delta < 0$ and $\delta^2 > 12\gamma^2$. However, we operate at *adequately low drive powers to ward off bistable signature*[§]. Now, in the limit $\gamma_0 \to 0$ and $\delta \to 0$, β becomes vanishingly small, and the first two terms in Eq. (6.13) recede in importance, for a given Rabi frequency Ω. Consequently, in the neighborhood of $\delta = 0$, the response becomes highly sensitive to variations in U. To be more precise, for sufficiently low values of the detuning, the response mimics the functional dependence $x \simeq \left(\frac{I}{4U^2}\right)^{1/3}$. A tenfold decrease in U, therefore, scales up the peak intensity of b by a factor of 4.64. In this context, it is useful to strike a correspondence with the sensitivity in eigenmode splitting around an EP. For two-mode systems, where the EP is characterized by a square root singularity, this splitting $\delta\omega$ scales as the square root of the perturbation parameter $\delta\mu$ implying a

[§]The bistable regime has been explored elsewhere, in the collaborative work of Ref. [154], which has been left out of this thesis.

sensitivity that goes as $\left|\frac{\delta\omega}{\delta\mu}\right| \propto |\delta\mu|^{-1/2}$. However, in our setup, the sensitivity to U in the response is encoded as

$$\left|\frac{\delta x}{\delta U}\right| \propto |U|^{-5/3}, \tag{6.14}$$

where the constant U itself is very small. The importance of the above result in the context of sensing is hereby legitimized for dissipatively coupled cavity-magnonic systems. We consider an integrated apparatus comprising a microwave cavity and a YIG sphere, both interfacing with a 1D waveguide, as was depicted in Fig. 5.4 of Chapter . In order to excite the weak Kerr nonlinearity of the YIG sphere, a microwave laser is used to drive the spatially uniform Kittel mode. The full Hamiltonian in presence of the external drive can be cast exactly in the form of Eq. (6.4), with b superseded by the magnonic operator m.

As discussed earlier, the mediating effect of the waveguide is reflected as a dissipative coupling between the two modes, which instills VIC into the system. With the anti-PT symmetric choices $\Delta_a = -\Delta_m = \delta/2$, $\gamma_a = \gamma_b = \gamma_0$, and the redefinition $\gamma_0 + \Gamma = \gamma$, we recover Eq. (6.13) in the steady state, with the obvious substitution $b \to m$ and $x = |m|^2$ denoting the spin current response. We now expound the utility of engineering a lossless system in sensing weak Kerr nonlinearity. To that end, we zero in on the parameter subspace $\Gamma = \gamma = 2\pi \times 10$ MHz. Since $\beta = -\delta^2/4$, the contributions from the first two terms in Eq. (6.13) taper off as the resonance condition is approached. As outlined earlier, we find that for all practical purposes, the nonlinear response can be approximated as $x \simeq \left(\frac{I}{4U^2}\right)^{1/3}$ in the region $\delta/2\pi < 1$ MHz, which demonstrates its stark sensitivity to U. A lower nonlinearity begets a higher response, as manifested in Fig. 6.2(a), where plots of x against δ are studied at differing strengths of the nonlinearity. Even at $D_p = 1\ \mu W$, we observe a significant enhancement in the induced spin current of the YIG around $\delta = 0$. The result is a natural upshot of the VIC-induced divergent response in an anti-PT symmetric system in the linear regime. Quite conveniently, the inclusion of nonlinearity dispels the seemingly absurd problem of a real singularity noticed in the linear case. If $\Gamma < \gamma$, a strong quenching in the response

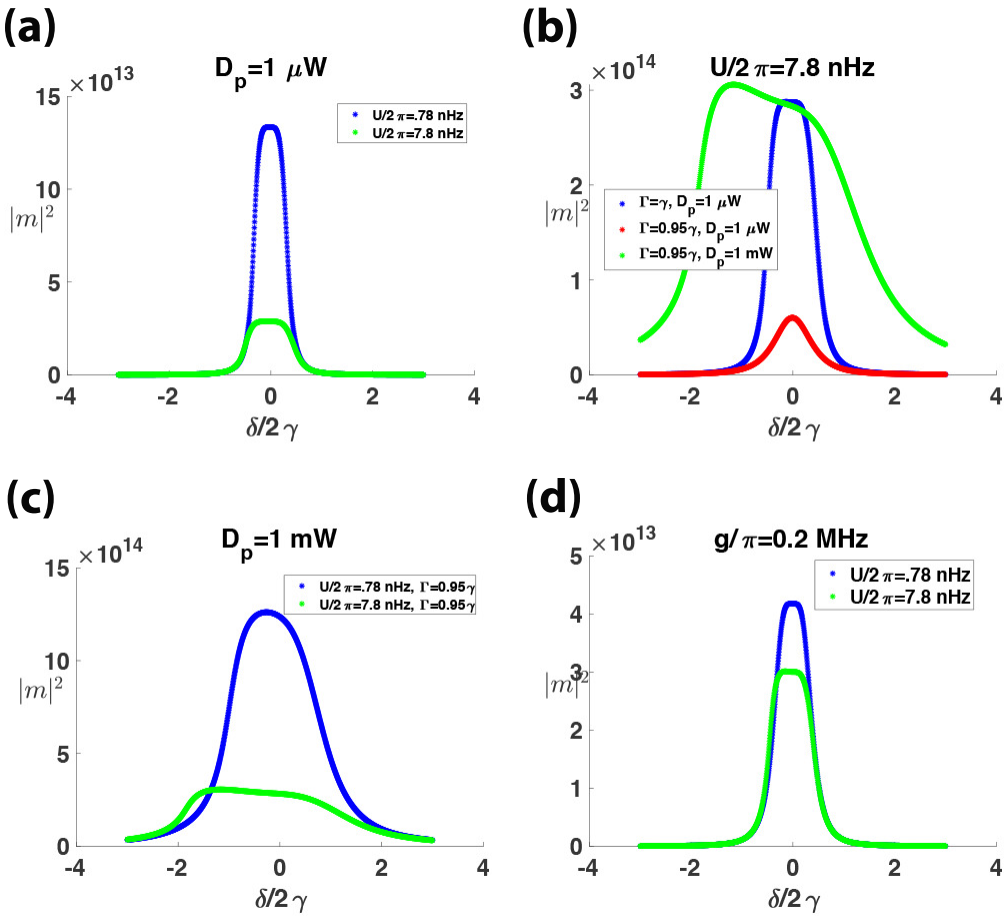

Figure 6.2: a) The spin current plotted against δ at two different nonlinearities; b) spin currents away from the VIC condition, compared against the lossless scenario, at different drive powers- for ease of comparison, the blue and red curves have been scaled up by 10; c) contrasting responses observed at a drive power of $1\ mW$ for two different strengths of nonlinearity; d) sensitivity for a nonzero coherent coupling g at $D_p = 1\ \mu$W.

is observed, as depicted in Fig. 6.2(b). The sensitivity to variations in U also incurs deleterious consequences. Nevertheless, we can counteract this decline by boosting the drive power. A drive power close to $1\ mW$ can bring back the augmented response and the pronounced sensitivity to U (figure 6.2(c)). By the same token, the introduction of coherent coupling g between the two modes prompts a decline in the sensitivity. The real singularity pertaining to a purely dissipative linear model is now replaced by a complex one, i.e., with a finite linewidth, bringing down the sharpness of the resonance and similarly, the sensitivity. Here, a tenfold depreciation in U barely generates an enhancement factor of 1.39 in the response, as illustrated in figure 6.2(d). This is to be contrasted with the $g = 0$ case in figure 6.2(a), where the magnification factor is 4.64 for an otherwise identical set of parameters. Propitiously, systems with zero coherent coupling (or purely dissipative coupling) were engineered in recent experiments [48, 99, 184]. This mechanism can, thus, serve as an efficient tool to sense small anharmonicities present in a system.

6.5 Anharmonicity-induced new coherences

The sensing protocol delineated in the last section hinges on the anti-PT symmetric character and the eigenmodes of H, which largely control the dynamics at low drive powers. At larger drive powers ($\sim 0.1\ W$), the nonlinear correction in Eq. (6.5) becomes important. This phenomenon can be understood by studying the modified spectroscopic character of the system in response to a weak probe field. The nonlinear effects can be encapsulated as time-varying fluctuations to the steady-state values, *viz.* $a(t) = a + \delta a(t)$, $b(t) = b + \delta b(t)$. The fluctuations $\delta a(t)$ and $\delta b(t)$ are presumed to be general, albeit small in relation to a_0 and b_0. This permits the dismissal of higher-order effects in these variations. Consequently, we have a simplification in the term $(b^\dagger b)b$ which appears in the dynamical equation for mode b in Eq. (6.5):

$$[b(t)^\dagger b(t)]b(t) \approx |b|^2 b + 2|b|^2 \delta b(t) + b^2 \delta b^\dagger(t). \tag{6.15}$$

This demonstrates that the variables $\delta b(t)$ and $\delta b^\dagger(t)$ get interconnected due to the anharmonicity. The inter-coupling is, of course, too weak to bear on any observable effects at smaller drive powers. However, higher drive powers $\sim 0.01W$ makes this coupling paramount. The dynamics of the fluctuations $\delta\xi = \begin{pmatrix} \delta a(t) & \delta b(t) & \delta a^\dagger(t) & \delta b^\dagger(t) \end{pmatrix}^T$ reduce to a linear dynamical model, $\left[\frac{\mathrm{d}}{\mathrm{d}t} + i\mathcal{H}_{NL}\right]\delta\xi(t) = \mathcal{E}_{in}(t)$, with

$$\mathcal{H}_{NL} = \begin{pmatrix} -\frac{\delta}{2} - i\gamma & -i\Gamma & 0 & 0 \\ -i\Gamma & \tilde{\Delta} - i\gamma & 0 & 2Ub_0^2 \\ 0 & 0 & \frac{\delta}{2} - i\gamma & -i\Gamma \\ 0 & -2Ub_0^{*2} & -i\Gamma & -\tilde{\Delta} - 2i\gamma \end{pmatrix}, \tag{6.16}$$

$\mathcal{E}_{in}(t) = \varepsilon\begin{pmatrix} e^{-i\delta_p t} & e^{-i\delta_p t} & e^{i\delta_p t} & e^{i\delta_p t} \end{pmatrix}^T$ where $\tilde{\Delta} = \frac{\delta}{2} + 4U|b|^2$. The eigenvalues of this matrix, for the cavity-magnon setting, appear in Fig. 6.3(a,b). Strong anharmonicity alters the coherence properties of the system, as reinforced by the extreme linewidth narrowing observed now around $\frac{\delta}{2\gamma} = -3.2$ in Fig. 6.3(b). Such effects were systematically explored in [154], where we discovered observable anomalies in the transmission signal due to new coherences. These anomalies can be traced to exotic properties of the eigenvalues, particularly when the imaginary parts of any of these eigenvalues become small. The nonlinearity spawns a long-lived eigenmode with ultrasmall linewidth leading to anomalous transmission effects like pump-to-probe energy transfer, similar to the Mollow gain effect [41], and enhanced sensitivity in waveguide transmission. We anticipate that this could have potential applications in futuristic signal-processing networks using driven nonlinear devices.

As a final remark, we also note that the nonlinear corrections at more intense pump powers stem from the matrix elements $2Ub^2$ and $-2Ub^{*2}$ in Eq. (6.16). This implies that the higher-dimensional eigensystem attains precedence over the linear model only when the product $U|b|^2$ becomes comparable to Γ. However, in the event that $U|b|^2 \ll \Gamma$, the nonlinearity acts merely as a perturbation. It is precisely in this weakly anharmonic regime that our sensing proposal holds

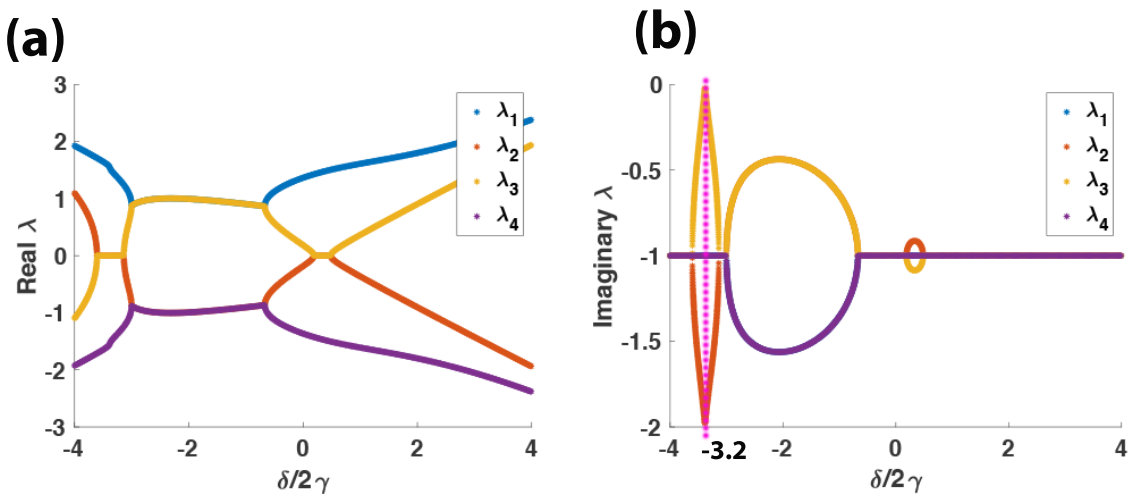

Figure 6.3: a) Real and b) imaginary parts of the eigenvalues of H_{NL} at a drive power of $0.1\ W$. The vertical dotted line running through the point $\delta/(2\gamma) = -3.2$ shows a new VIC point induced by the system's anharmonic excitation. At such a point, the transmission signal can become really strong, aided by pump-to-probe energy transfer.

relevance.

6.6 Summary

In summary, we have proposed a dissipative test bed that shows enhanced sensitivity to Kerr nonlinearity of the mode, hence qualifying it as a prototypical agency to gauge the strength of anharmonic perturbations under optimal conditions.Our scheme is distinct from the one popularly used for the detection of linear perturbations around an EP. The sensitivity to anharmonicities in our model can be traced down to the existence of a remarkably long-lived eigenmode of the linear system, characterized by a vanishing linewidth. The physical origin of this peculiar behavior lies in an effective coupling induced between the cavity and the magnon modes in the presence of a shared ancillary reservoir. Optimal results vis-à-vis the estimation of nonlinearity are obtained when VIC strongly dominates, i.e., when spontaneous emissions from the modes to the surrounding environments become negligible in comparison to the waveguide-mediated coupling. To provide numerical estimates, our analysis has been tailored to demonstrate a pronounced sen-

sitivity in the context of magnonic excitations. Nonetheless, the essence of our assessment would be applicable to any two-mode nonlinear system. Moreover, our scheme can also be used to sense linear perturbative effects. Finally, we have shown that higher drive powers engender new domains of VIC-like points on account of strongly anharmonic responses. The precise implications of these new VICs have been explored by us as part of a separate project [154], and have only been glossed over in Sec 6.5.

7. APPLICATION OF ANTI-PT SYMMETRY TO ENHANCED TRANSDUCTION BETWEEN MICROWAVE AND OPTICAL FIELDS*

Superconducting qubits are widely recognized as one of the prime candidates for processing quantum information. The qubits operate at low temperatures in the microwave regime. Concurrently, for communication of quantum information, optical nanofibers are utilized on account of their low-loss transmission, long-time memory, and low thermal occupancy. A coherent and reversible conversion between microwave and optical fields is thereby instrumental to achieving robust, long-distance quantum communication through superconducting quantum processors. Such an interface can effectively leverage the strengths of optical signals, which include , while simultaneously facilitating control over superconducting circuits which deploy microwave signals. One would thus like to engineer efficient quantum transducers, which are devices that execute the desired conversion between two kinds of signals. To that end, hybrid micro/nano-scale systems have being been designed which combine different degrees of freedom to accomplish this conversion in an optimal fashion. Of these, the most commonly pursued routes are ones that exploit either light coupling to mechanical modes (optomechanics), electrons coupling to collective vibrations in a nanotube (electromechanics). A conversion efficiency close to 10% between microwave signals of a few GHz into optical domain was demonstrated in an experiment [185] using optomechanical systems. In general, a variety of systems have been explored, including not only optomechanical systems [185–188], but cold atoms [189, 190], spins [191, 192], trapped ions [193, 194], and electro-optic systems [195, 196]. Fairly recently, when magnons in a magnetic material were experimentally coupled to both superconducting qubits [140] and parametrically to optical photons [197–199], magnons also entered the fray as potential wavelength converters. However, while much progress has been made with regard to optomechanical and electro-optomechanical setups, the transduction has not been accomplished with a desirable efficiency in cavity magnonics.

*Largely reprinted with permission from *Anti-PT symmetry enhanced interconversion between microwave and optical fields* by D. Mukhopadhyay, J. M. P. Nair, and G. S. Agarwal, Phys. Rev. B **105**, 064405 (2022), published by the American Physical Society. Collaboration with J. M. P. Nair is acknowledged.

A few years ago, Hisatomi *et al.* demonstrated bidirectional conversion between microwave and optical waves in a hybrid cavity-magnonic setup, where a microwave cavity was coherently coupled to the Kittel mode in a YIG sample through the Purcell effect. The mechanism for conversion was premised on a triliniear Faraday interaction between two orthogonally polarized optical modes and a Kittel mode [200]. Subsequently, Ihn *et al.* generalized this result to the multimode case by accounting for both the Kittel mode and a higher-order space-varying magnetostatic mode [201]. The primary challenge posed by these setups is the weakness of the parametric interaction between the optical modes and the magnonic frequencies, as this is a weak, second-order nonlinear effect. Lately, we set forth a conversion model comprising a *dissipatively coupled cavity-magnonic system* and implementing *much stronger* transduction between microwave and optical signals [50]. Based on the same principle, the converter draws its potential from the *anti-PT symmetry* of the configuration. By harnessing the effect of strong VIC, we found that anti-PT symmetry allowed improvements in the conversion efficiency by a few orders of magnitude relative to the non-symmetric regime. While coherently coupled systems were found to achieve an efficiency of $\eta^{(c.c)} \sim 10^{-5}$ [200], our setup affords a theoretical efficiency of around 2.5×10^{-3} in the vicinity of the VIC point. Since the nonlinear Faraday interaction driving the conversion is quite weak, such an improvement over preexisting protocols is quite intriguing. In addition, our work also highlighted an inherent asymmetry between the efficiencies of the two opposite pathways of conversion. Even though the Faraday coupling between the magnon mode and the optical fields is perfectly symmetrical, a fundamental asymmetry emerges between the efficiencies of microwave-to-optical and optical-to-microwave conversion. This asymmetry stems, in part, from the phase sensitivity of the output fields, and also, from the fact that optical fields are entirely decoupled from the microwave cavity while the YIG interacts with both kinds of fields. It could be appreciated that while it is generally challenging to engineer non-reciprocity [202–205] in physical systems, such an attribute is naturally built into waveguide-integrated photonic devices.

The structure of this chapter is summarized as follows. Following a concise review of nonlinear three-wave mixing in Sec. 7.1, we overview the magneto-optic Faraday effect in Sec 7.2 that is

responsible for transduction in our setup. The theoretical formulation underpinning the conversion model is introduced in Sec. 7.3, subsequent to which we explain the two possible schemes vis-à-vis the microwave-to-optical transduction mechanism in Secs. 7.4 and 7.5. In Sec 7.6, we derive the efficiency of the reverse conversion, *viz.* optical to microwave, and demonstrate the nonreciprocity of the two conversion pathways. Finally, we summarize the key results in 7.7.

7.1 Nonlinear three-wave mixing

Nonlinear three-wave interactions constitute the bedrock of several exotic nonlinear optical phenomena, including stimulated Raman and Brillouin scattering [206], first observed by Woodbury *et al.* [207] and later explained by Garmire *et al* [208], and Bloembergen and Shen [209, 210], employing a coupled-wave formalism. Quantum mechanically, such an interaction can be understood as the energy-conserving conversion of an incident pump quantum into two daughter quanta and vice versa.

Nonlinear optical phenomena are "nonlinear" in the sense that they occur when the response of a material system to an applied optical field $E(t)$ depends in a nonlinear manner on the strength of the applied optical field. Three-wave mixing is a second-order nonlinear effect originating from the second-order contribution to the nonlinear polarization, $P^{(2)}(t) = \epsilon_0 \chi^{(2)} E(t)$, where $\chi^{(2)}$ is the second-order susceptibility of the medium of propagation, assumed isotropic. When an overall oscillating (scalar) electric field $E(t) = \mathcal{E}_1 e^{-i\omega_1 t} + \mathcal{E}_2 e^{-i\omega_2 t}$ ($\omega_1 > \omega_2$) is applied to a nonlinear crystal with nonzero $\chi^{(2)}$, the resulting polarization contains contributions from various components that oscillate at frequencies $\omega_1 + \omega_2$, $\omega_1 - \omega_2$, $2\omega_1$, and $2\omega_2$, along with a static DC component. In conformity with Maxwell's equations, the induced polarization, in turn, generates oscillating waves at the above frequencies. The physical processes pertaining to the production of the frequencies $\omega_1 + \omega_2$ and $\omega_1 - \omega_2$ are referred to as sum-frequency generation and difference-frequency generation respectively. However, such exchanges do not require all fields to be optical or lie in overlapping frequency domains. For instance, such three-mode interactions have been widely investigated in the context of the interconversion between optical and microwave fields,

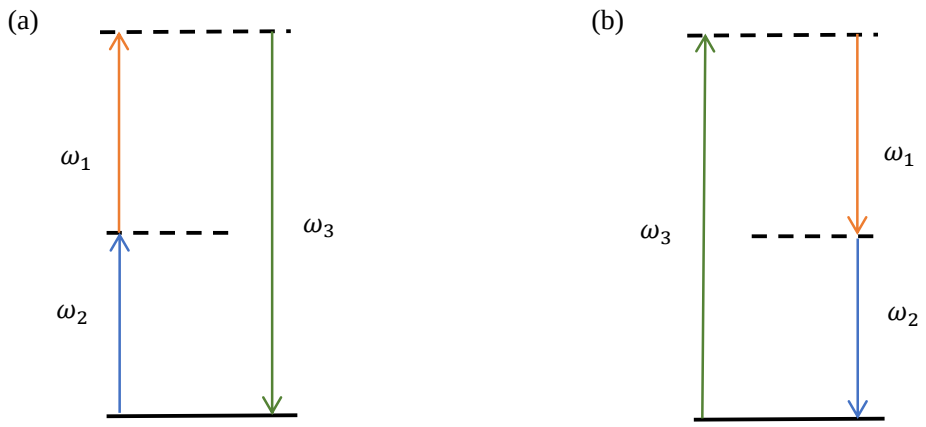

Figure 7.1: Visualization of (a) Sum-frequency generation and (b) Difference-frequency generation. Energy conservation implies $\omega_1 + \omega_2 = \omega_3$.

both of which are pivotal to an efficient information processing network. Since optical frequencies lie in the THz domain and microwave frequencies are of GHz scale, it is possible, in principle, to find a microwave frequency ω_μ and two optical frequencies Ω and Ω_0 ($\Omega > \Omega_0$) satisfying $\Omega = \Omega_0 + \omega_\mu$. Consequently, by launching one optical photon at Ω_0 and a microwave photon at ω_μ into a nonlinear $\chi^{(2)}$-medium, one can produce an optical photon at the "sum-frequency" Ω. The converse procedure can be initiated by making incident the higher-frequency photon at Ω. The process of difference-frequency generation is also termed as parametric amplification as it leads to the amplification of the lower-frequency input wave. These processes are illustrated in Fig. 7.1(a,b).

Two of the most well-known scattering processes that involves three-wave mixing interaction are Raman scattering and Brillouin scattering. While the former describes scattering of light off optical phonons, the latter refers to light scattering from acoustic phonons. In a laboratory ambience, three-wave mixing is typically achieved using a birefringent crystalline material, where the refractive index depends on the polarization and the direction of the light that passes through the medium. Birefringence is the phenomenon wherein the refractive index of propagating radiation field depends on its direction of polarization. In a magnetic sample, the Faraday effect naturally

engenders birefringence, leading to a trilinear optomagnonic interaction. This is what we discuss next.

7.2 Optomagnonics and the magneto-optic Faraday Effect

Since the magnon spin dynamics plays out in the GHz regime, we have already seen that it is possible to generate strong, linear magnon-photon couplings in the microwave regime via the resonant tuning of frequencies. This is why one magnon can be converted into a photon and vice versa. However, the coupling between magnons and photons in the optical regime is fundamentally different from that in the microwave regime, since single-photon absorptions are non-resonant with the excitation frequency of magnons. Therefore, only two-photon resonant phenomena can be observed in the optical regime. As we discussed earlier, such processes ensue from the nonlinear three-wave mixing amongst photons in non-overlapping frequency domains. The corresponding coupling is known as parametric coupling and the mechanism by which this is achieved in a magnetic system is the Faraday effect [211]. This effect is caused by left- and right-circularly polarized waves propagating at slightly different speeds, a property known as circular birefringence. Since a linear polarization can be decomposed into the superposition of two equal-amplitude circularly polarized components of opposite handedness and different phase, the effect of a relative phase shift, induced by the Faraday effect, is to rotate the orientation of a wave's linear polarization. This produces an optomagnonic interaction involving the magnetization of the material and two orthogonally polarized modes of light [212, 213]. The effect of three-wave mixing due to the Faraday effect in a YIG sample was independently demonstrated by Osada *et al.* [197], X. Zhang *et al.* [198], and Haigh *et al.* [199]. As an example, in [197], a 500 μm YIG sphere was evanescently coupled to an optical fiber to produce optical sidebands in the output signal which were displaced by the magnonic excitation frequency. YIG has a large Verdet constant of $\mathcal{V} = 3.8$ rad/cm corresponding to a 1550 nm optical field, and is therefore, suitable for observing the nonlinear Faraday effect. We next spell out a simple derivation of the quantized Faraday Hamiltonian, following Ref. [200].

Suppose that linearly polarized light, with polarization vector along the z axis, and propagating along the x axis is incident on a ferromagnetic sample with a length L, which is magnetized along the z axis under a bias magnetic field. Consistent with the principle of the Faraday effect, the magnetization oscillation perpendicular to the z axis is incorporated to the polarization oscillations. The resulting optomagnonic interaction $\mathcal{H}_{\text{int}}$ takes the form

$$\mathcal{H}_{\text{int}} = \int_0^T \hbar G \, M_x(t) s_x(t) Ac, \tag{7.1}$$

where G is a coupling parameter related to the Verdet constant, $T = \dfrac{L}{v}$ is the interaction time, with v being the speed of light in the material, and A is the cross section of the light beam. $M(t)$ is the *magnetization density* induced in the sample, which can be quantized in terms of the magnon mode operators as

$$M_x(t) = \frac{\sqrt{N}}{V}\Big[m(t) + m^\dagger(t)\Big], \tag{7.2}$$

with V being the volume of the YIG and $N = \rho V$ being the total number of spins in the sample. The operator $s_x(t)$ is related to the $x-$component of the Stokes operator of light and has the expression

$$s_x(t) = \frac{1}{2A}\Big[b_R^\dagger(t) b_R(t) - b_L(t) b_L^\dagger(t)\Big], \tag{7.3}$$

where $b_R(t)$ and $b_L(t)$ are respectively the annihilation operators for the right-circularly and left-circularly polarized light modes propagating along the $x-$axis.

Now assume that a strong laser field in the z-polarized mode impinges on the YIG, for which the annihilation operator $b_z(t)$ can be treated classically, i.e.,

$$b_z(t) \simeq \sqrt{\frac{P_0}{\hbar\Omega_0}} e^{-i\Omega_0 t}, \tag{7.4}$$

with P_0 being the input power in the mode and Ω_0 being its angular frequency. Let $b_y(t)$ represent the annihilation operator for the mode with linear polarization along the y axis. Then the circularly polarized modes $b_R(t)$ and $b_L(t)$, can be written as

$$b_R(t) = \frac{1}{\sqrt{2}}\Big[b_y(t) + ib_z(t)\Big] \quad \text{and} \quad b_L(t) = \frac{1}{\sqrt{2}}\Big[b_y(t) - ib_z(t)\Big] \tag{7.5}$$

respectively. Substituting these into Eq. (7.1), we obtain

$$\mathcal{H}_{\text{int}} = \frac{i\hbar G\sqrt{N}c}{4V}\cdot\sqrt{\frac{P_0}{\hbar\Omega_0}}\int_0^T \Big[m(t) + m^\dagger(t)\Big]\Big[b_y^\dagger(t)e^{-i\Omega_0 t} - b_y(t)e^{i\Omega_0 t}\Big]\,\mathrm{d}t \tag{7.6}$$

Upon assuming that the interaction time T is shorter than the oscillatory timescale of the magnon dynamics, $1/\omega_m$, the operators $m(t)$ and $b_y(t)$ can be treated as constants during the interaction, in the frame rotating at the laser frequency Ω_0. Then the Hamiltonian $\mathcal{H}_{\text{int}}$ in Eq. (7.6) reduces to

$$\mathcal{H}_{\text{int}} = -i\hbar\sqrt{\kappa_o}(m + m^\dagger)[b_y e^{i\Omega_0 t} - b_y^\dagger e^{-i\Omega_0 t}] \tag{7.7}$$

where the integration is performed to get $\int_0^T cdt = cT = L$. The light-magnon coupling rate κ_0 is defined as $\kappa_0 = \dfrac{\rho G^2 L^2}{16V}\dfrac{P_0}{\hbar\Omega_0}$, where $G = \dfrac{4\mathcal{V}}{\rho}$, $\mathcal{V}$ is the Verdet constant, and ρ is the spin density of the sample. With the rotating-wave approximation, the above Hamiltonian reduces to either the parametric-amplification-type Hamiltonian given by

$$\mathcal{H}_{\text{P.A.}} = -i\hbar\sqrt{\kappa_0}(mb_y e^{i\Omega_0 t} - m^\dagger b_y^\dagger e^{-i\Omega_0 t}) \tag{7.8}$$

which is effective only around $\Omega = \Omega_0 - \omega_m$, or the beamsplitter-type Hamiltonian given by

$$\mathcal{H}_{\text{B.S.}} = i\hbar\sqrt{\kappa_0}(mb_y^\dagger e^{-i\Omega_0 t} - m^\dagger b_y e^{i\Omega_0 t}) \tag{7.9}$$

which is effective only around $\Omega = \Omega_0 + \omega_m$. Eq. (7.8) describes Stokes scattering while (7.9) is the underlying Hamiltonian for the anti-Stokes scattering process.

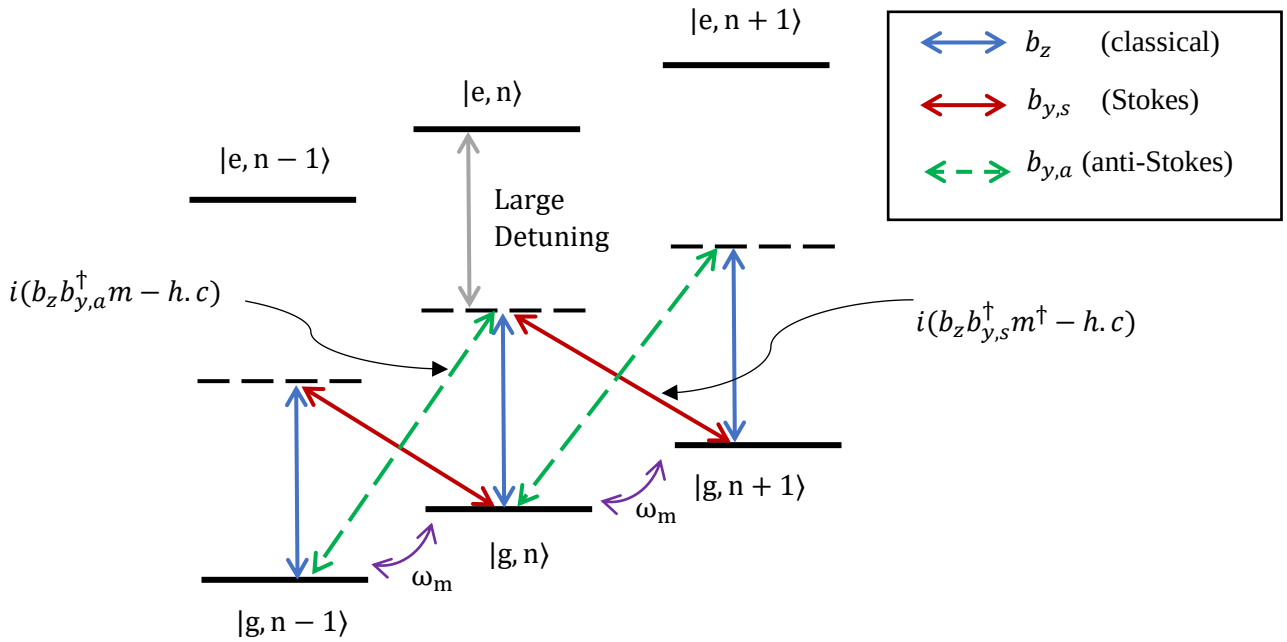

Figure 7.2: Energy levels of the magnetic system showing the allowed two-photon transitions relevant to the trilinear optomagnonic interaction. The states $|g\rangle$,$|e\rangle$ specify the electronic states while $|n\rangle$ represents the magnon Fock state within either one of these manifolds. By driving the system with an optical field detuned far below the $|g\rangle \leftrightarrow |e\rangle$ transition, a threeway interaction is whipped up between the magnon and the optical fields. The inset maps the relevant optical modes to the energy transitions within the ground-state manifold. The mode b_z is taken to be a large coherent field. The problem then reduces to the interconversion between a magnon excitation and another optical mode which is frequency-shifted relative to Ω_0 by an amount ω_m. The modes $b_{y,s}$ and $b_{y,a}$ denote red-detuned and blue-detuned optical fields respectively, with the corresponding frequencies given by $\Omega_0 - \omega_m$ and $\Omega_0 + \omega_m$. The Stokes-shifted mode $b_{y,s}$ is produced through the interaction $\mathcal{H}_{\text{P.A.}} \simeq i\hbar\sqrt{\kappa_0}(b_z b_{y,s}^\dagger m^\dagger - h.c)$, whereas the anti-Stokes component is generated via $\mathcal{H}_{\text{B.S.}} = i\hbar\sqrt{\kappa_0}(b_z b_{y,a}^\dagger m - h.c)$ (compare Eqs. (7.8), (7.9)). (Redrawn from *Phys. Rev. B 93, 174427 (2016)*.)

Explanation from the Energy-level diagram: Fig. 7.2 illustrates the energy levels in a YIG sample, appropriate to the magneto-optic Faraday effect and its inverse phenomenon, the *inverse Faraday effect*. The states $|g\rangle$ and $|e\rangle$ pertain to the electronic ground and excited states of the material, with $|n-1\rangle$, $|n\rangle$ and $|n+1\rangle$ representing the magnon Fock states within the manifold of a given electronic state. Electronic transitions between these two manifolds represent the charge-transfer transition ${}^6\mathrm{S}(3d^5 2p^6) \leftrightarrow {}^6\mathrm{P}(3d^6 2p^5)$. The associated wavelength of this transition is 440 nm. Thus, by applying optical fields far detuned below this transition frequency, it is possible to induce *two-photon resonant phenomena* involving magnon excitations. For example, the wavelength of the incident coherent field in Ref. [200] was 1550 nm. Owing to the large detuning, a system starting out in the electronic ground state can only make virtual transitions to the excited state. Now, there are two ways to induce two-photon transitions. As shown in the figure, by applying a large classical field b_z (frequency Ω_0), the system in an initial state $|g, n\rangle$ can emit a photon into the mode $b_{y,a}$ (frequency $\Omega_0 + \omega_m$) and settles eventually into $|g, n-1\rangle$, simultaneously annihilating a magnon excitation in the process. Effectively, a magnon gets converted into an optical photon of frequency $\Omega_0 + \omega_m$. Likewise, the system in the initial state $|g, n\rangle$, having absorbed a photon from the b_z-field, may as well relax into the final state $|g, n+1\rangle$ by concurrently emitting a photon into the mode $b_{y,s}$ (frequency $\Omega_0 - \omega_m$) and creating a magnon. An optical photon is thereby converted into a magnon excitation.

7.3 Model for transduction

We consider a hybrid cavity-magnonic model in which a rectangular microwave cavity and a YIG interacts dissipatively via a one-dimensional (1D) microwave transmission line. Unlike the previously explored scenario where the YIG was wedged inside the cavity resonator to enhance the coherent coupling between them through the Purcell effect [200, 201], the interposing waveguide here acts as the mediator of a long-range coupling between the two. For the purpose of the conversion process, the YIG sphere is evanescently coupled to an ancillary optical fiber withal. The

transduction mechanism could be initiated by the application of a microwave drive at a frequency ω_μ, duly complemented by an intense laser drive at a frequency Ω_0 sent along optical fiber targeting the YIG sample. The converse mechanism of optical-to-microwave transfer proceeds via the administration of two orthogonally polarized optical inputs at frequencies Ω and Ω_0 respectively, such that the frequency discord $|\Omega - \Omega_0|$ is closely resonant with a Kittel mode frequency, which lies in the microwave regime.

System Hamiltonian: At the outset, we overview a first-principle description of the exchange dynamics enabling the mode conversions. In the most general case, the full Hamiltonian $\mathcal{H} = \mathcal{H}_s + \mathcal{H}_{\text{micro}} + \mathcal{H}_{\text{optical}}$ of the driven cavity-YIG system would comprise of the following contributions:

$$\begin{aligned}
\mathcal{H}_s =& \hbar\omega_a a^\dagger a - \hbar\gamma_e B_0 S_z, \\
\mathcal{H}_{\text{micro}} =& \mathcal{H}^{(a)}_{\text{micro}} + \mathcal{H}^{(m)}_{\text{micro}}, \\
\mathcal{H}_{\text{optical}} =& -i\hbar\sqrt{\kappa_o}(m + m^\dagger)[b_y e^{i\Omega_0 t} - b_y^\dagger e^{-i\Omega_0 t}].
\end{aligned} \tag{7.10}$$

Here, $\mathcal{H}_s$ represents the free Hamiltonian of the cavity-YIG composite, where a ($a^\dagger$) denotes the annihilation (creation) operator of the cavity, B_0 the applied bias magnetic field and S_z the collective spin operator of the YIG along the z direction, and γ_e is the gyromagnetic ratio. Employing the Holstein-Primakoff transformation, the Hamiltonian of the magnons reduce to $\hbar\omega_m m^\dagger m$, with $\omega_m = \gamma_e B_0$. The Hamiltonian $\mathcal{H}_{\text{micro}}$ captures the typical interplay between incident microwave photons and the cavity-YIG network, with the first term $\mathcal{H}^{(a)}_{\text{micro}}$ encapsulating the coupling of the microwave drive to the cavity. The second term

$$\mathcal{H}^{(m)}_{\text{micro}} = -\hbar\gamma_e \vec{S}.\vec{B}_{\text{micro}} \tag{7.11}$$

characterizes the exchange interaction between the Kittel mode in the YIG and the local AC microwave field $\vec{B}_{\text{micro}}$. The specific expressions for $\mathcal{H}^{(a)}_{\text{micro}}$ and $\mathcal{H}^{(m)}_{\text{micro}}$ would be introduced in due course based on contextual considerations about the incident fields. In addition, two linearly po-

larized optical field modes selectively couple to the ferromagnetic material which is magnetized along the z direction, producing the trilinear Faraday interaction $\mathcal{H}_{\text{optical}}$. This interaction generates optical sidebands displaced by $\omega_m = \gamma_e B_0$ on either flank of the Ω_0-band, and thereby, converting those incident microwave photons into optical photons. By the same token, the application of two orthogonally polarized optical beams stimulates the production of a microwave field oscillating at a frequency equaling the difference between the two optical frequencies, a phenomenon commonly known as the inverse Faraday effect. These two phenomena constitute the physical foundation of the conversion scheme.

The dissipative non-Hermitian coupling between the cavity and the YIG has to be formalized at the level of a master equation for the system by treating the common waveguide as a thermal bath. Note that in writing the exact form of the Faraday interaction $\mathcal{H}_{\text{optical}}$, the phase acquired by the optical wave vis-à-vis its transit from the cavity to the YIG has been absorbed in the definition of the $y-$polarized optical mode b_y. In principle, there could be two possible schemes of effecting the microwave-to-optical conversion: (i) by guiding the microwave drive field along the microwave fiber, or (ii) by directly shining a maser on the YIG. In the following two sections, we develop explicit results for the two schemes separately.

7.4 Microwave-to-Optical Conversion: Input through waveguide

Apropos of the microwave-to-optical conversion process, the magnons in mode m are driven by a classical microwave drive frequency ω_μ, while concurrently interfacing with an optical waveguide that delivers and channels the optical component b_y. In Fig. 7.3, which conveys a particular modality of exciting the system, the input microwave drive is launched through the bottom fiber. An alternative means would involve directly impinging a maser on the YIG sample, which we would discuss as a separate scheme. The Faraday interaction $\mathcal{H}_{\text{optical}}$, prompted by the pump laser b_z at the frequency Ω_0 sent along the optical channel, entails the Stokes and anti-Stokes sidebands relative to Ω_0 in the optical spectrum. The indirect coupling Γ engineered between the cavity and the magnons through the interceding transmission line consolidates the coupling of the YIG to the

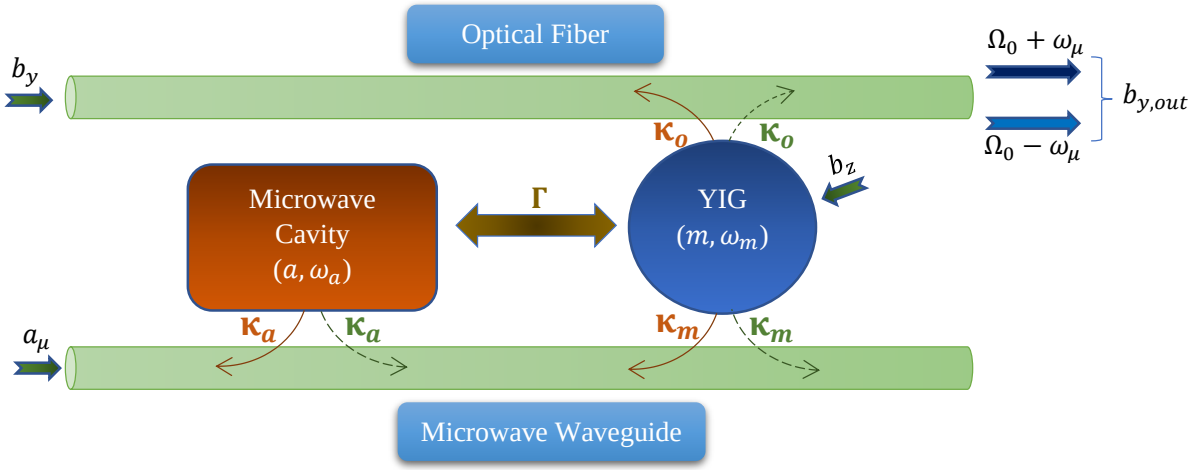

Figure 7.3: First scheme for microwave-to-optical conversion. The bottom microwave waveguide couples to both the cavity and the YIG sphere, whereas the itinerant vacuum mode b_y in the top fiber, polarized along y-axis, addresses the collective magnonic excitation. A microwave signal a_μ is launched through the bottom channel, in conjunction with an intense optical laser drive b_z, polarized along the z-axis and shone on the YIG. This induces both the Stokes and the anti-Stokes optical sidebands at the output port of the optical fiber.

microwave photons via the Purcell effect. The sideband outputs can be empirically reconstructed from the amplified, beat-down, heterodyne signal between the carrier and the side modes.

When the microwave field is launched through the transmission line, the magnons encounter a phase-translated input relative to the intracavity field, which promptly simplifies the components in $\mathcal{H}_{\text{micro}}$ to

$$\begin{aligned}\mathcal{H}^{(a)}_{\text{micro}} &= -i\hbar\sqrt{\kappa_a}[a^\dagger a_\mu e^{-i\omega_\mu t} - a a^\dagger_\mu e^{i\omega_\mu t}],\\ \mathcal{H}^{(m)}_{\text{micro}} &= -i\hbar\sqrt{\kappa_m}[m^\dagger a_\mu e^{-i(\omega_\mu t-\phi)} - m a^\dagger_\mu e^{i(\omega_\mu t-\phi)}],\end{aligned} \tag{7.12}$$

where κ_a and κ_m symbolize the leakage rates of the cavity and the magnons respectively into the interfacing microwave line, and a_μ is the microwave drive.

Stokes process: It is convenient to redefine the system variables as $\tilde{a} = ae^{i\omega_\mu t}$, $\tilde{m} = me^{i\omega_\mu t}$,

and, depending on whether we consider the Stokes or anti-Stokes process, $\tilde{b}_y = b_y e^{i(\Omega_0-\omega_\mu)t}$ or $\tilde{b}_y = b_y e^{i(\Omega_0+\omega_\mu)t}$. The operation dispels the explicit time-dependence in $\mathcal{H}$, when the fast-oscillating terms are expunged. The first process pertains to a parametric-amplification type process, whereas the second is associated with a beam-splitter type interaction, both of which are familiar from the literature. For the Stokes process, the Hamiltonian morphs into

$$\begin{aligned} H_{s.w.} = {} & \Delta_a \tilde{a}^\dagger \tilde{a} + \Delta_m \tilde{m}^\dagger \tilde{m} - (\Omega_0 - \omega_\mu)\tilde{b}_y^\dagger \tilde{b}_y - i\sqrt{2\kappa_a}[\tilde{a}^\dagger a_\mu - \tilde{a} a_\mu^\dagger] - i\sqrt{2\kappa_m}[\tilde{m}^\dagger a_\mu - \tilde{m} a_\mu^\dagger] \\ & - i\sqrt{2\kappa_o}(\tilde{m}\tilde{b}_y - \tilde{m}^\dagger \tilde{b}_y^\dagger), \end{aligned} \tag{7.13}$$

in which we have introduced the detuning parameters $\Delta_a = \omega_a - \omega_\mu$ and $\Delta_m = \omega_m - \omega_\mu$. We now solve the Langevin equations to the lowest order in the optomagnonic coupling rate $\sqrt{\kappa_0}$. For notational simplicity, we shall drop the tildes over the mode variables.

Pursuant to the master equation derived in Appendix B, the mean-value dynamics of the cavity and the magnon modes reduces to

$$\begin{aligned} \dot{a} &= -(i\Delta_a + \gamma_a)a - \Gamma e^{i\phi} m - \sqrt{\kappa_a} a_\mu, \\ \dot{m} &= -(i\Delta_m + \gamma_m)m - \Gamma e^{i\phi} a - \sqrt{\kappa_m} a_\mu e^{i\phi} + \sqrt{\kappa_o} b_y^\dagger. \end{aligned} \tag{7.14}$$

where $\gamma_a = \kappa_a + \tilde{\kappa}_a$ and $\gamma_m = \kappa_m + \tilde{\kappa}_m$ encompass the dissipative effects, and the expectation-value notations have been suppressed under the semiclassical approximation. The decay rate $\tilde{\kappa}_a$ ($\tilde{\kappa}_m$) stands for the intrinsic damping of the cavity (magnon) mode into the non-waveguide modes. Based on the input-output formulation, the output Stokes wave would be accorded by the relation

$$b_{y,\text{out}} = -\sqrt{\kappa_o} m^\dagger, \tag{7.15}$$

since the input mode b_y, in this case, can be taken to be the thermal vacuum. Eq. (7.14) can be

condensed into the form

$$\dot{X} = -i\mathcal{M}X - \mathcal{F} - \sqrt{\kappa_o}\mathcal{G}, \tag{7.16}$$

where $X = (a \;\; m)^T$, $\mathcal{F} = a_\mu(\sqrt{\kappa_a} \;\; \sqrt{\kappa_m}e^{i\phi})^T$, $\mathcal{G} = (0 \;\; b_y^\dagger)^T$, and $\mathcal{M} = \begin{pmatrix} \Delta_a - i\gamma_a & -i\Gamma e^{i\phi} \\ -i\Gamma e^{i\phi} & \Delta_m - i\gamma_m \end{pmatrix}$. If $b_{y,\text{out}}$ has to be solved to the lowest (here, linear) order in $\sqrt{\kappa_0}$, it follows that the long-time solution to X could be obtained by dropping the final term in (7.16), leading to

$$X = i\mathcal{M}^{-1}\mathcal{F}. \tag{7.17}$$

Hence, the solutions to the intracavity field and the magnonic oscillation stand as

$$\begin{aligned} a &= \frac{ia_\mu[\sqrt{\kappa_a}(\Delta_m - i\gamma_m) + i\sqrt{\kappa_m}e^{2i\phi}\Gamma]}{(\Delta_a - i\gamma_a)(\Delta_m - i\gamma_m) + \Gamma^2 e^{2i\phi}}, \\ m &= \frac{ia_\mu e^{i\phi}[i\sqrt{\kappa_a}\Gamma + \sqrt{\kappa_m}(\Delta_a - i\gamma_a)]}{(\Delta_a - i\gamma_a)(\Delta_m - i\gamma_m) + \Gamma^2 e^{2i\phi}}. \end{aligned} \tag{7.18}$$

By virtue of Eq. (7.15), we educe the Stokes conversion efficiency to be

$$\eta_s^{(d.c)} = \left|\frac{b_{y,\text{out}}}{a_\mu}\right| = \left|\frac{i\Gamma\sqrt{\kappa_o\kappa_a} + (\Delta_a - i\gamma_a)\sqrt{\kappa_o\kappa_m}}{(\Delta_a - i\gamma_a)(\Delta_m - i\gamma_m) + \Gamma^2 e^{2i\phi}}\right|, \tag{7.19}$$

For comparison, we recall the efficiency factor in a coherent environment, where a (double-sided) microwave cavity addresses the magnons in the YIG by means of a Hermitian coupling $J(a^\dagger m + am^\dagger)$. In that case, $\mathcal{M}$ is replaced by $\begin{pmatrix} \Delta_a - i\gamma_a & J \\ J & \Delta_m - i\gamma_m \end{pmatrix}$ and $\mathcal{F}$ by $a_\mu(\sqrt{\kappa_a} \;\; 0)^T$, when the microwave cavity is driven [200]. Then, the same input-output relation would yield a conversion efficiency

$$\eta_s^{(c.c)} = \left|\frac{b_{y,\text{out}}}{a_\mu}\right| = \left|\frac{J\sqrt{\kappa_o\kappa_a}}{(\Delta_a - i\gamma_a)(\Delta_m - i\gamma_m) - J^2}\right|. \tag{7.20}$$

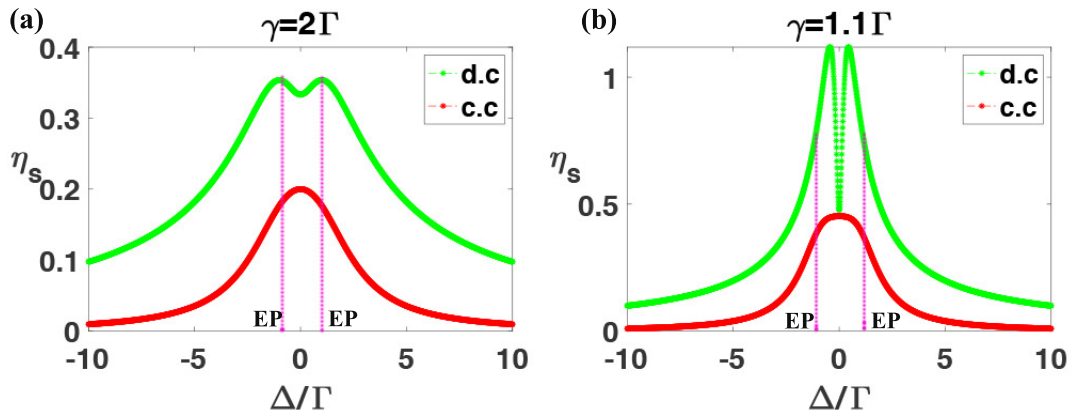

Figure 7.4: Stokes conversion efficiencies for the microwave-to-optical conversion pertaining to scheme 1, are plotted under anti-PT symmetric conditions and comparable couplings $\Gamma = J$ in both dissipative and coherent setups. In (a), we impose $\gamma = 2\Gamma$ and in (b), we consider $\gamma = 1.1\Gamma$. The EPs are identified via the dotted vertical lines. The regions between the vertical lines denote the symmetry-broken phases. The absolute efficiencies in both (a) and (b) have been scaled up by a factor of $S = 1.4 \times 10^5$, for $\Gamma \approx \pi \times 25$ MHz and $\kappa_0 \approx \pi \times 0.3$ mHz.

Since the solution to X determines the Stokes sideband of the optical spectra, its efficiency of conversion from the microwave input pivots on the symmetry properties of $\mathcal{M}$. For anti-PT symmetry, we require the constraints $\Delta_a = -\Delta_m = \Delta$, $\gamma_a = \gamma_m = \gamma$ and $\phi = n\pi$, with n being a natural number. Figures 7.4(a,b) plot the conversion factors for both dissipatively coupled and dispersively coupled systems for comparable system parameters and similar coupling strengths ($\Gamma \approx J$), under the constraint of anti-PT symmetry. It is interesting to note the broadband nature of the profiles for anti-PT symmetry.

While the order of magnitude does not change dramatically by switching to a dissipative configuration, it does turn out that dissipative couplings can predominantly outstrip the efficiency of coherent setups under anti-PT conditions. From Eqs. (7.19) and (7.200), the figure of merit quantified as an advantage gained through anti-PT symmetry in dissipative environments can be simplified as

$$\frac{\eta_s^{(d.c)}}{\eta_s^{(c.c)}} = \left[\frac{\{\Delta^2 + (\gamma - \Gamma)^2\}\{\Delta^2 + \gamma^2 + \Gamma^2\}}{\Gamma^2\{\Delta^2 + \gamma^2 - \Gamma^2\}}\right]^{1/2}, \tag{7.21}$$

where $\kappa_a \approx \kappa_m$ and $\Gamma \approx J$ has been assumed. For large dampings or frequency detunings in the range $\Delta \geq \Gamma$, the expression above exceeds 1, demonstrating the superiority of these couplings. In the complementary regime, the situation is not so cut and dry, and numerical means become the imperative.

Anti-Stokes output: The anti-Stokes process is described by the transformed Hamiltonian

$$\begin{aligned} H_{a.s.w.} = {} & \Delta_a \tilde{a}^\dagger \tilde{a} + \Delta_m \tilde{m}^\dagger \tilde{m} - (\Omega_0 + \omega_\mu)\tilde{b}_y^\dagger \tilde{b}_y - i\sqrt{\kappa_a}[\tilde{a}^\dagger a_\mu - \tilde{a} a_\mu^\dagger] - i\sqrt{\kappa_m}[\tilde{m}^\dagger a_\mu - \tilde{m} a_\mu^\dagger] \\ & - i\sqrt{\kappa_o}(\tilde{m}^\dagger \tilde{b}_y - \tilde{m}\tilde{b}_y^\dagger), \end{aligned} \tag{7.22}$$

to which the equations of motion are obtained as

$$\begin{aligned} \dot{a} &= -(i\Delta_a + \gamma_a)a - \Gamma e^{i\phi} m - \sqrt{\kappa_a} a_\mu, \\ \dot{m} &= -(i\Delta_m + \gamma_m)m - \Gamma e^{i\phi} a - \sqrt{\kappa_m} a_\mu e^{i\phi} - \sqrt{\kappa_o} b_y, \end{aligned} \tag{7.23}$$

where, once again, we have suppressed the tildes. An identical calculation for the anti-Stokes process yields the same efficiency factor as above, i.e.,

$$\eta_{as}^{(d.c)} = \left|\frac{b_{y,\text{out}}}{a_\mu}\right| = \left|\frac{i\Gamma\sqrt{\kappa_o \kappa_a} + (\Delta_a - i\gamma_a)\sqrt{\kappa_o \kappa_m}}{(\Delta_a - i\gamma_a)(\Delta_m - i\gamma_m) + \Gamma^2 e^{2i\phi}}\right|, \tag{7.24}$$

The relevant input-output relation employed in this case is $b_{y,\text{out}} = -\sqrt{\kappa_o} m$. Thus, the input microwave photons of frequency ω_μ, upon interacting with the optical wave of frequency Ω_0, are converted into output traveling light modes with frequencies $\Omega_0 - \omega_\mu$ and $\Omega_0 + \omega_\mu$ pertaining to the Stokes and anti-Stokes bands respectively. The two processes are therefore, equivalent to

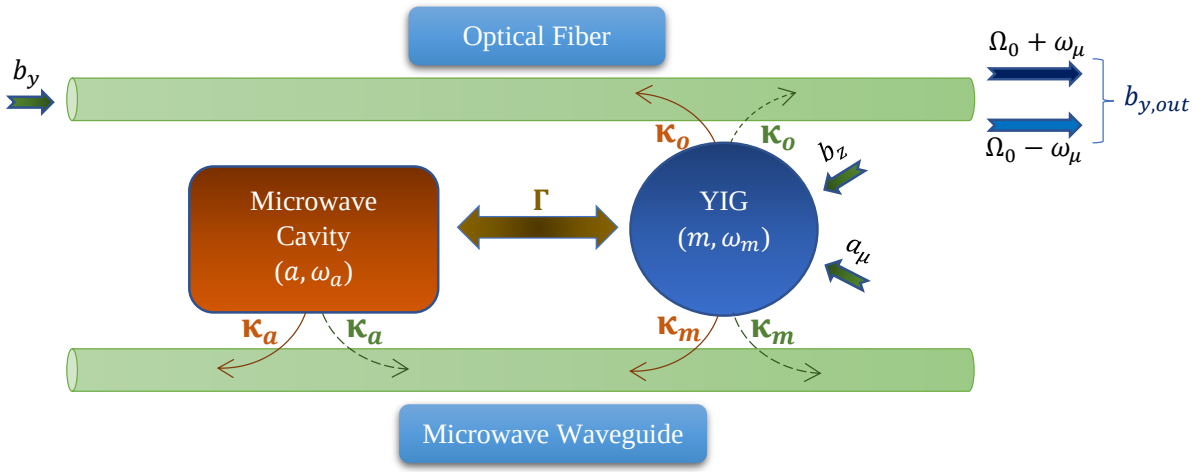

Figure 7.5: Second scheme for microwave-to-optical conversion. The microwave input as well as the laser drive are targeted on the YIG sphere, generating the optical sidebands.

the difference-frequency generation and sum-frequency generation respectively, which were introduced in Sec. 7.1.

7.5 Microwave-to-Optical Conversion: Direct excitation of magnons

This protocol of selectively driving the YIG sphere, as demonstrated in Fig. 7.5, can exploit a spectral singularity of dissipatively interacting systems in drawing out an enhanced steady-state response in the hybrid system. We know that the VIC, when optimally strong, can push one of the poles in the linear response to the real axis, under anti-PT symmetric conditions. With the corresponding linewidth suffering a stark suppression, the resonant response shoots up, only to be regularized by intrinsic anharmonicites present in any of the modes. This is the same feature that was cashed in for the sensing of weak perturbations in Chapter 6. Here, we throw light on the feasibility of ramping up the efficiency of our conversion model by operating in the neighborhood of this singularity. With this constraint, it is easy to see that the poles in Eq. (7.19) approach zero as $\Delta \to 0$ and $\Gamma \to \gamma$. This is possible under the circumstance when extraneous decoherence is strongly overshadowed by the coherence produced by the shared reservoir. However, around

this point, the numerator also becomes small, precluding sizable enhancements in the output fields procreated via scheme 1. To mitigate the pernicious role of the numerator, we can merely resort to shining a maser beam on the YIG sample. While the microwave-YIG interaction becomes

$$\mathcal{H}_{\text{micro}}^{(m)} = -i\hbar\sqrt{2\kappa_m}[m^\dagger a_\mu e^{-i(\omega_\mu t-\phi)} - m a_\mu^\dagger e^{i(\omega_\mu t-\phi)}], \tag{7.25}$$

the cavity gets decoupled from any external driving fields. Therefore, the term $\mathcal{H}_{\text{micro}}^{(a)}$ drops out. The Langevin equations for the mode amplitudes corresponding to the Stokes process would, then, be remodeled as

$$\begin{aligned}
\dot{a} &= -(i\Delta_a + \gamma_a)a - \Gamma e^{i\phi} m, \\
\dot{m} &= -(i\Delta_m + \gamma_m)m - \Gamma e^{i\phi} a - \sqrt{2\kappa_m} a_\mu e^{i\phi} + \sqrt{\kappa_o} b_y^\dagger.
\end{aligned} \tag{7.26}$$

The input-output relation pertaining to the optical mode b_y remains intact, which yields the Stokes efficiency factor to be

$$\eta_s^{(d.c)} = \left|\frac{b_{y,\text{out}}}{a_\mu}\right| = \frac{\sqrt{2\kappa_o\kappa_m(\Delta_a^2+\gamma_a^2)}}{|(\Delta_a - i\gamma_a)(\Delta_m - i\gamma_m) + \Gamma^2 e^{2i\phi}|} \tag{7.27}$$

To bring out the significance of the anti-PT symmetry, we look at the behavior of the above expression under this constraint, i.e., $\Delta_a = -\Delta_m = \Delta$, $\gamma_1 = \gamma_2 = \gamma$ and $\phi = n\pi$. The efficiency is plotted in Fig. 7.6, which unveils a spike around the origin $\Delta/\kappa = 0$. When γ is only slightly larger than Γ, such that $\gamma = \Gamma(1+\varepsilon)$ for $\varepsilon \ll 1$, the above expression reduces, in the limit $\Delta/\Gamma \to 0$, to

$$\eta_s^{(d.c)} \approx (\varepsilon/2)^{-1}(\kappa_o/\kappa_a)^{1/2}. \tag{7.28}$$

Consequently, the smallness of ε has a direct bearing on the scaling up of the figure of merit characterizing the conversion scheme. For instance, when ε becomes one-tenth, there is about a tenfold

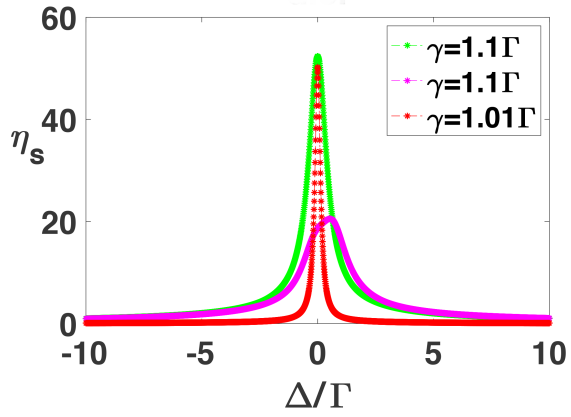

Figure 7.6: Stokes conversion efficiencies for the scheme 2 with the chosen parameters $\gamma = 1.1\Gamma$ (i.e., $\varepsilon = 0.1$) and $\gamma = 1.01\kappa$ (i.e., $\varepsilon = 0.01$), under anti-PT symmetry. The graph with the lowest peak corresponds to a non-anti-PT-symmetric system with $\Delta_a = \Delta, \Delta_m = -\Delta + 0.5\Gamma, \gamma = 1.1\Gamma$. The absolute efficiencies have been scaled up by $S(\varepsilon = 0.1) = 1.4 \times 10^5$ and $S(\varepsilon = 0.01) = 1.4 \times 10^4$. The two graphs in the anti-PT symmetric case have peaks in close proximity of each other, which vindicates the proportionality in Eq. (15).

amplification observed in the optical output. This is evident from the comparative plot in Fig. 7.6, since the deviations of γ from Γ are respectively one and two orders of magnitude smaller than Γ. In the same figure, we also contrast the symmetric system with a non-symmetric one satisfying $\Delta_a = \Delta$, $\Delta_m = -\Delta + 0.5\Gamma$ and $\gamma = 1.1\Gamma$. A substantial reduction in the peak conversion efficiency - by about a factor of 2.5 - is observed near the origin in the non-symmetric case, testifying to the role of anti-PT symmetrIC VIC point in boosting the conversion potential. This property can also be justified from the perspective of bright and dark states pertaining to radiating and non-radiating modes of the system. On defining two linearly independent modes $c_\pm = 1/\sqrt{2}(a \pm m)$, we find that the mode c_- evolves as $\dot{c}_- = -\varepsilon\Gamma c_- - i\Delta c_+ - \sqrt{\kappa_m}a_\mu + \sqrt{\kappa_0}b_y^\dagger$. Thus, the mode c_- acts as a long-lived mode, akin to a dark state, as ε becomes small. The other mode c_+ decays significantly faster at the rate of 2Γ. The emergence of a dark state explains the coherent buildup in the output signal around the singularity $\varepsilon = 0$.

Theoretical enhancement relative to the experiment in Ref. [200]: To provide some perspec-

tives on the kind of enhancement we observe in our scheme, we recall the experimental parameters from the seminal work of Hisatomi *et al.*. By tuning the microwave-YIG resonance frequency to approximately $2\pi \times 9.5$ GHz, they created strong hybridization between the magnon mode and the input microwave field with a coherent coupling strength of $g \simeq 2\pi \times 63$ MHz. By impinging a 1550 nm laser (with a frequency of 200 THz) at an incident power of $P_0 = 0.015$ W, they were able to generate sidebands displaced by the magnon frequency. Harnessing a high spin density of $\rho = 2.1 \times 10^{28}\, m^{-3}$ and the diameter of YIG as $d = 0.75$ mm, they could engineer an optomagnonic coupling rate of $\kappa_0 \simeq 2\pi \times 0.25$ mHz. This supported a microwave-to-optical conversion efficiency of roughly $\eta^{(c.c)} \simeq 10^{-5}$. For a comparable dissipative coupling strength of $\Gamma \approx g$, our scheme of operating near the VIC point ($\gamma = 1.01\Gamma$) yields a theoretical efficiency of $\eta^{(d.c)} \simeq 2.5 \times 10^{-3}$. Working slightly away from the VIC point, with $\gamma = 1.1\Gamma$, this roughly becomes 2.6×10^{-4}, around one-tenth of the previous value. The second scheme of directly irradiating the magnetic sample, therefore, proffers enhancements in the conversion efficiency by around $1 - 2$ orders of magnitude.

7.6 Optical-to-Microwave conversion: Asymmetrical efficiencies

The reverse procedure of light getting transformed into microwave photons is made feasible by the inverse Faraday effect. The initial conditions are now translated into injecting two copropagating phase-coherent laser inputs (b_y and b_z) along the optical transmission line, with the relevant frequencies in the optical domain and separated by a microwave frequency. If the difference frequency coincides with a Kittel mode frequency, the resonance imparts an oscillatory magnetization to the magnons in the YIG, which, in turn, elicit traveling microwave photons at this difference frequency. With the plane-wave ansatz $b_y = \sqrt{\dfrac{P}{\hbar\Omega}} e^{-i\Omega t}$, where P is the drive power, we can derive the induced microwave output at frequency $\omega_+ = \Omega_0 - \Omega$ (Stokes scattering) or $\omega_- = \Omega - \Omega_0$ (anti-Stokes scattering), depending on whichever is positive, by solving the dynamical equations in time domain. For this process, we can rotate the variables as $m \to m e^{i\omega_\mu t}$ and $a \to a e^{i\omega_\mu t}$, and

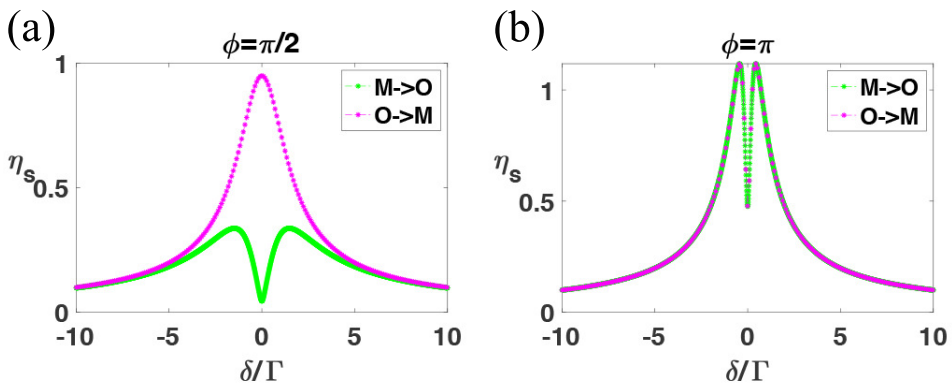

Figure 7.7: Nonreciprocal Stokes' conversion efficiencies (M: Microwave, O: Optical) pertaining to the scheme 1, for the system parameters $\Delta_a = -\Delta_m = \delta$ (for M→O) and $\delta_a^{(+)} = -\delta_m^{(+)} = \delta$ (for O→M), plotted against δ for two sets of the phase separation ϕ. We choose $\gamma_a = \gamma_m = 1.1\Gamma$. The conversion is, however, reciprocal when ϕ is an integer multiple of π. The M→O graphs refer to Eq. (7.19), and the O→M graphs refer to Eq. (7.32).

define the input amplitude $\beta = \sqrt{\dfrac{P}{\hbar\Omega}}$. Then, the evolution equations would be

$$\begin{aligned} \dot{a} &= -(i\delta_a^{(\pm)} + \gamma_1)a - \Gamma e^{i\phi} m, \\ \dot{m} &= -(i\delta_m^{(\pm)} + \gamma_2)m - \Gamma e^{i\phi} a \pm \sqrt{\kappa_o}\beta, \end{aligned} \tag{7.29}$$

where the detunings $\delta_a^{(\pm)} = \omega_a - \omega_\pm$ and $\delta_m^{(\pm)} = \omega_m - \omega_\pm$ have been introduced, and the rapid oscillations neglected. Since no classical microwave drive needs to be applied, the corresponding interaction term has been dropped. It is now a simple exercise to evaluate the scattered microwave field in the long-time limit. Clearly, the long-time solutions $X_\pm$ would correspond to fresh microwave oscillations at ω_+ or ω_-, as the case may be, as an artifact of the nonlinear mixing between the two optical beams and the driven magnons. Eq. (7.29) yields the solutions

$$X_\pm = \mp i\sqrt{\kappa_0}\beta\mathcal{H}^{-1}\begin{pmatrix} 0 \\ 1 \end{pmatrix}. \tag{7.30}$$

Invoking the input-output relation for the field transmitted across the microwave waveguide,

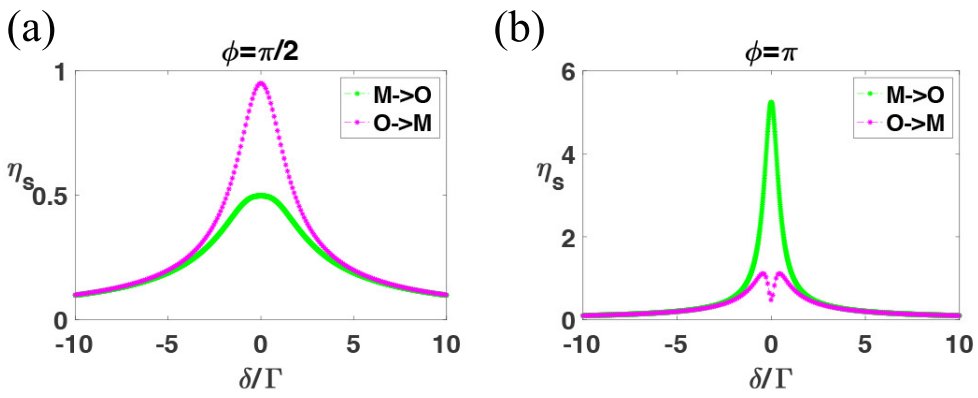

Figure 7.8: Nonreciprocity in the Stokes' conversion efficiencies (M: Microwave, O: Optical) pertaining to scheme 2, for the system parameters $\Delta_a = -\Delta_m = \delta$ (for M→O) and $\delta_a^{(+)} = -\delta_m^{(+)} = \delta$ (for O→M). We use the same damping parameters as in Fig. 5. The M→O graphs refer to Eq. (7.27), and the O→M graphs to Eq. (7.32).

we find that

$$\begin{aligned} a_{\text{out}}^{\pm} &= -(\sqrt{\kappa_a}e^{i\phi}a_{\pm} + \sqrt{\kappa_m}m_{\pm}) \\ &= \mp i\beta\left[\frac{i\Gamma e^{2i\phi}\sqrt{\kappa_0\kappa_a} + \sqrt{\kappa_o\kappa_m}(\delta_a^{\pm} - i\gamma_1)}{(\delta_a^{\pm} - i\gamma_1)(\delta_m^{\pm} - i\gamma_2) + \Gamma^2 e^{i\phi}}\right]. \end{aligned} \tag{7.31}$$

This allows us to infer the conversion efficiencies for the two possible microwave bands,

$$\left|\frac{a_{\text{out}}^{\pm}}{\beta}\right| = \left|\frac{i\Gamma e^{2i\phi}\sqrt{\kappa_o\kappa_a} + (\delta_a^{\pm} - i\gamma_1)\sqrt{\kappa_o\kappa_m}}{(\delta_a^{\pm} - i\gamma_1)(\delta_m^{\pm} - i\gamma_2) + \Gamma^2 e^{2i\phi}}\right|. \tag{7.32}$$

where the upper sign refers to the Stokes band and the lower to the anti-Stokes generation.

Strikingly, there is a structural disparity between the expression in Eqs. (7.19) or (7.27), and that in Eq. (7.32), indicating nonreciprocal transductions. In the case of scheme 1, for $\phi = n\pi$, the microwave-to-optical conversion efficiency and vice versa resemble each other up to a reinterpretation of the detunings. However, there is a palpable quantitative asymmetry in the two mechanisms pertaining to an arbitrary phase for an otherwise commensurate set of system parameters, as demonstrated in Fig. 7.7(a,b). The discrepancy between the two efficiency factors is even more evident in scheme 2, whereby the two conversion processes ensue with starkly disparate efficien-

cies, regardless of the choice of phase. We illustrate this effect in Fig. 7.8(a,b). Fundamental to the nonreciprocity in either scheme is the factor that microwave fields are directly or indirectly linked up with both the cavity and the YIG, whereas the optical fields interact purely with the YIG. In addition, the phase-sensitive asymmetry pertinent to scheme 1 can be traced down to the existence of the reservoir-mediated phase-coupling between the cavity and the YIG, that is a characteristic of dissipatively coupled systems. This is veritably distinct from the symmetric nature of conversion observed in coherently coupled setups, where both the conversion mechanisms unfold with equal efficiencies. Note that this nonreciprocity in the conversion mechanisms exists in spite of the symmetrical interaction between the two optical modes and the magnons, as embodied in $\mathcal{H}_{\text{optical}}$.

7.7 Summary

In conclusion, we have demonstrated the efficient interconversion between optical and microwave fields in the context of a dissipatively coupled optomagnonic setup. Dissipatively coupled systems with anti-PT symmetry perform significantly better than coherent settings for comparable system parameters, although both are based on the nonlinear Faraday effect. We have explicated two disparate schemes for the microwave-to-optical conversion, one of which involves injecting the microwave field through the shared waveguide and the other where the ferromagnetic sample is directly subject to an external pump. While the two schemes showcase improved conversion efficiencies compared to the coherently coupled systems, the second scheme in particular, which directly drives the magnetic sample, manifests remarkable improvements when the dissipative coupling dominates the extraneous dissipations. Very close to the VIC point, i.e., $\gamma = 1.01\Gamma$, the efficiency was found to be almost 2.5×10^{-3}. This superior conversion efficiency stems from the emergence of a long-lived dark mode near the VIC point, and consequently, the linear response suffers a tremendous boost. This efficiency could be further improved, in principle, by integrating an optical cavity to the converter. Alternatively, magnetic materials with even larger Verdet constants, such as chromium tribromide, can be used in place of YIG, which would naturally enhance the optomagnonic coupling rate κ_0. Efforts along these lines have already started to show promise

[214]. Finally, we have shown that the transduction protocols achieved via strong phase-sensitive dissipative couplings feature strong nonreciprocity, with stark discrepancies in the efficiencies of microwave to optical conversion and vice versa.

8. CONCLUDING REMARKS AND FUTURE OUTLOOK

To conclude, this thesis has been focused primarily on the theoretical study of waveguide-integrated photonics and driven dissipative quantum systems, both of which have received widespread attention from the experimental community. With the sheer amount of progress being made in waveguide-QED, waveguide-integrated circuits continue to expand the frontiers of research in purely optics-based quantum computing [4, 85, 215–221]. The Fano-like interference between multiple emission pathways in the photonic interaction with an array of spatially separated emitters makes the photon transport strongly nonreciprocal and sensitive to the spatial separation. Although experimental investigations on photon transport in these setups have picked up speed over the last two decades, it is imperative to make continual upgrades to bridge the chasm between theory and experiment. With the tremendous success of superconducting artificial atoms as robust, low-decoherence quantum emitters, the future in this field certainly looks promising.

Hybrid quantum systems coupled to a waveguide channel render a conspicuous light-matter interface to carry out some of the most vital information processing tasks in an optimal manner. This includes, but is not restricted to, converting microwave signals to light and vice versa - one crucial sector that we have explored in our research. The manipulation of coherent coupling between systems has long been a cornerstone of quantum optics and information processing. It is fairly recent that the hallmarks and the immense potential of waveguide-mediated couplings are starting to find widespread recognition. The dissipative interaction mediated between distant emitters enables one to not only entangle these emitters but also to explore EP-induced phase transition and topological phenomena [102–104], without resorting to extrinsic gain as is usually the case with directly coupled systems. Considering the pronounced relevance of magnon-based systems, we have examined some of the key functionalities of dissipative coupling and anti-PT symmetry by placing them in the specific context of such systems. However, one thing we have made sure in many of our analyses is to emphasize on the generality of our models, whenever feasible. To exemplify this point, our sensing scheme for detecting anharmonicities was formulated in an abso-

lutely general context, apropos of a large class of quantum systems. The same is true for a related work on nonlinear systems (albeit, not considered in this thesis) where we established the role of dissipative coupling in lowering the pumping threshold for bistability [154]. That said, it is to be acknowledged that cavity magnonics has emerged as a new, fertile testing ground for examining some of the deeply held concepts in quantum optics and assessing the limits of quantum signatures in macroscopic systems.

As a prospective project, we are now considering, for instance, the quantum effects of squeezing in amplifying magnon-photon and effective magnon-magnon couplings. Specifically, a parametric drive is found to draw out a much greater response in the spin current from the magnon modes. Quite generally speaking, quantum control of magnon states would be an important idea to pursue in the foreseeable future. On the subject of waveguide QED, new interest has cropped up in chiral waveguides, in which the emitters relax with differential emission rates into the two oppositely propagating field modes. The directional dependence of atomic emission provides an entirely different setup for manipulating photon scattering. Preliminary calculations have shown that these setups usher in vastly different transport properties. A chiral system shifts the condition for Fano-minimum and reintroduces high transmission in a region of high reflectivity observed in the non-chiral system. In the simple case of two identical 2LAs, chirality brings in a transmission peak on resonance when $kL = n\pi$. This is in striking discord with the non-chiral system of identical emitters addressed in Chapter 3 of this thesis, where we had demonstrated superradiance in the reflection for $kL = n\pi$. Since chirality acts as an independent parameter strongly modifying the transport, it can be deployed as an optical switch. Therefore, the controllability of chiral characteristics and the feasibility of unidirectional emission, i.e., when the atoms emit into a *single direction*, merit further investigation. It would also be interesting to transcend the single-excitation regime into the two-photon and multiphoton regimes. Not only does the associated Hilbert space in these regimes feature higher complexity, the photons themselves have the possibility of getting correlated [222, 223]. The incidence of a second photon stimulates relaxation of the excited atom to its ground state, leading to enhancement of emission from the atom [224]. This stimulated emission

owes its origin *largely* to an effective *photon-photon correlation* induced by the emitter. In addition to scattering states, the physics of correlated few-photon transport supports an additional category of states, known as *multiphoton bound states* [222, 223, 225]. Signatures of photon-photon correlation in the multiphoton regime would offer novel quantum insights accessible neither within the single-photon manifold nor in the semiclassical limit of large photon numbers. In Ref. [222], an asymptotic analysis (i.e., far away from the scattering source) of the two-photon scattering eigenstate for a single 2LA in a waveguide reported intriguing photon-correlation properties: the transmitted photons are *bunched*, while the reflected photons are *antibunched*. Going ahead, it would be worthwhile to examine these photon-correlated states from an information-theoretic viewpoint. Finally, it would also be interesting to extend our analysis of photon transport to the context of infinite periodic lattices, dimer lattices and disordered systems, in general. Periodic geometries are particularly interesting to explore since a given lattice periodicity gets mapped into a distinctive spectral profile with a collective decay rate depending on the scale of the system. Such a treatment allows tracing the spectral signature of crystalline structures down to their periodicity. In the same vein, spectroscopic lineshapes of defective lattices should afford definite insights into the nature of disorder in the system. Using absorption/emission spectra as the penetration probes of internal configurations has long been one of the holy grails of optics. Therefore, a coherent analysis of photon dispersion and transport properties in these prototypical systems should facilitate a better understanding of the collective effects emerging in complex, many-body systems with crystalline features.

REFERENCES

[1] Galan Moody *et al*. 2022 roadmap on integrated quantum photonics. *Journal of Physics: Photonics*, 4(1):012501, jan 2022.

[2] Herbert Walther, Benjamin T H Varcoe, Berthold-Georg Englert, and Thomas Becker. Cavity quantum electrodynamics. *Reports on Progress in Physics*, 69(5):1325–1382, apr 2006.

[3] Andreas Reiserer and Gerhard Rempe. Cavity-based quantum networks with single atoms and optical photons. *Rev. Mod. Phys.*, 87:1379–1418, Dec 2015.

[4] Io-Chun Hoi, C. M. Wilson, Göran Johansson, Tauno Palomaki, Borja Peropadre, and Per Delsing. Demonstration of a single-photon router in the microwave regime. *Phys. Rev. Lett.*, 107:073601, Aug 2011.

[5] M. Arcari, I. Söllner, A. Javadi, S. Lindskov Hansen, S. Mahmoodian, J. Liu, H. Thyrrestrup, E. H. Lee, J. D. Song, S. Stobbe, and P. Lodahl. Near-unity coupling efficiency of a quantum emitter to a photonic crystal waveguide. *Phys. Rev. Lett.*, 113:093603, Aug 2014.

[6] Meng Khoon Tey, Zilong Chen, Syed Abdullah Aljunid, Brenda Chng, Florian Huber, Gleb Maslennikov, and Christian Kurtsiefer. Strong interaction between light and a single trapped atom without the need for a cavity. *Nature Physics*, 4(12):924–927, 2008.

[7] Fam Le Kien, S. Dutta Gupta, V. I. Balykin, and K. Hakuta. Spontaneous emission of a cesium atom near a nanofiber: Efficient coupling of light to guided modes. *Phys. Rev. A*, 72:032509, Sep 2005.

[8] Dibyendu Roy, C. M. Wilson, and Ofer Firstenberg. Colloquium: Strongly interacting photons in one-dimensional continuum. *Rev. Mod. Phys.*, 89:021001, May 2017.

[9] J. T. Shen and Shanhui Fan. Coherent photon transport from spontaneous emission in one-dimensional waveguides. *Opt. Lett.*, 30(15):2001–2003, Aug 2005.

[10] Lan Zhou, Z. R. Gong, Yu-xi Liu, C. P. Sun, and Franco Nori. Controllable scattering of a single photon inside a one-dimensional resonator waveguide. *Phys. Rev. Lett.*, 101:100501,

Sep 2008.

[11] Jie-Qiao Liao, Jin-Feng Huang, Yu-xi Liu, Le-Man Kuang, and C. P. Sun. Quantum switch for single-photon transport in a coupled superconducting transmission-line-resonator array. *Phys. Rev. A*, 80:014301, Jul 2009.

[12] D Witthaut and A S Sørensen. Photon scattering by a three-level emitter in a one-dimensional waveguide. *New Journal of Physics*, 12(4):043052, apr 2010.

[13] Nam-Chol Kim, Jian-Bo Li, Zhong-Jian Yang, Zhong-Hua Hao, and Qu-Quan Wang. Switching of a single propagating plasmon by two quantum dots system. *Applied Physics Letters*, 97(6):061110, 2010.

[14] Nam-Chol Kim, Myong-Chol Ko, and Qu-Quan Wang. Single plasmon switching with n quantum dots system coupled to one-dimensional waveguide. *Plasmonics*, 10(3):611–615, Jun 2015.

[15] Mu-Tian Cheng, Xiao-San Ma, Meng-Ting Ding, Ya-Qin Luo, and Guang-Xing Zhao. Single-photon transport in one-dimensional coupled-resonator waveguide with local and nonlocal coupling to a nanocavity containing a two-level system. *Phys. Rev. A*, 85:053840, May 2012.

[16] Zeyang Liao, Xiaodong Zeng, Shi-Yao Zhu, and M. Suhail Zubairy. Single-photon transport through an atomic chain coupled to a one-dimensional nanophotonic waveguide. *Phys. Rev. A*, 92:023806, Aug 2015.

[17] Wei-Bin Yan and Heng Fan. Control of single-photon transport in a one-dimensional waveguide by a single photon. *Phys. Rev. A*, 90:053807, Nov 2014.

[18] Cong-Hua Yan and L. F. Wei. Photonic switches with ideal switching contrasts for waveguide photons. *Phys. Rev. A*, 94:053816, Nov 2016.

[19] T. S. Tsoi and C. K. Law. Quantum interference effects of a single photon interacting with an atomic chain inside a one-dimensional waveguide. *Phys. Rev. A*, 78:063832, Dec 2008.

[20] T. S. Tsoi and C. K. Law. Single-photon scattering on Λ-type three-level atoms in a one-dimensional waveguide. *Phys. Rev. A*, 80:033823, Sep 2009.

[21] D. F. Kornovan, M. I. Petrov, and I. V. Iorsh. Transport and collective radiance in a basic quantum chiral optical model. *Phys. Rev. B*, 96:115162, Sep 2017.

[22] Jung-Tsung Shen and Shanhui Fan. Theory of single-photon transport in a single-mode waveguide. i. coupling to a cavity containing a two-level atom. *Phys. Rev. A*, 79:023837, Feb 2009.

[23] Jung-Tsung Shen and Shanhui Fan. Theory of single-photon transport in a single-mode waveguide. ii. coupling to a whispering-gallery resonator containing a two-level atom. *Phys. Rev. A*, 79:023838, Feb 2009.

[24] Dibyendu Roy. Two-photon scattering by a driven three-level emitter in a one-dimensional waveguide and electromagnetically induced transparency. *Phys. Rev. Lett.*, 106:053601, Feb 2011.

[25] Paolo Longo, Peter Schmitteckert, and Kurt Busch. Few-photon transport in low-dimensional systems: Interaction-induced radiation trapping. *Phys. Rev. Lett.*, 104:023602, Jan 2010.

[26] Huaixiu Zheng, Daniel J. Gauthier, and Harold U. Baranger. Cavity-free photon blockade induced by many-body bound states. *Phys. Rev. Lett.*, 107:223601, Nov 2011.

[27] Yao-Lung L. Fang and Harold U. Baranger. Waveguide qed: Power spectra and correlations of two photons scattered off multiple distant qubits and a mirror. *Phys. Rev. A*, 91:053845, May 2015.

[28] Matthew Bradford, Kenechukwu C. Obi, and Jung-Tsung Shen. Efficient single-photon frequency conversion using a sagnac interferometer. *Phys. Rev. Lett.*, 108:103902, Mar 2012.

[29] Lukas Neumeier, Martin Leib, and Michael J. Hartmann. Single-photon transistor in circuit quantum electrodynamics. *Phys. Rev. Lett.*, 111:063601, Aug 2013.

[30] Lan Zhou, Li-Ping Yang, Yong Li, and C. P. Sun. Quantum routing of single photons with a cyclic three-level system. *Phys. Rev. Lett.*, 111:103604, Sep 2013.

[31] Xingmin Li and L. F. Wei. Designable single-photon quantum routings with atomic mirrors.

Phys. Rev. A, 92:063836, Dec 2015.

[32] Mu-Tian Cheng, Xiao-San Ma, Jia-Yan Zhang, and Bing Wang. Single photon transport in two waveguides chirally coupled by a quantum emitter. *Opt. Express*, 24(17):19988–19993, Aug 2016.

[33] E. Sanchez-Burillo, D. Zueco, J. J. Garcia-Ripoll, and L. Martin-Moreno. Scattering in the ultrastrong regime: Nonlinear optics with one photon. *Phys. Rev. Lett.*, 113:263604, Dec 2014.

[34] S. Derouault and M. A. Bouchene. One-photon wave packet interacting with two separated atoms in a one-dimensional waveguide: Influence of virtual photons. *Phys. Rev. A*, 90:023828, Aug 2014.

[35] Ya. S. Greenberg and A. A. Shtygashev. Non-hermitian hamiltonian approach to the microwave transmission through a one-dimensional qubit chain. *Phys. Rev. A*, 92:063835, Dec 2015.

[36] Mu-Tian Cheng and Yan-Yan Song. Fano resonance analysis in a pair of semiconductor quantum dots coupling to a metal nanowire. *Opt. Lett.*, 37(5):978–980, Mar 2012.

[37] Mu-Tian Cheng, Jingping Xu, and Girish S. Agarwal. Waveguide transport mediated by strong coupling with atoms. *Phys. Rev. A*, 95:053807, May 2017.

[38] William Konyk and Julio Gea-Banacloche. One- and two-photon scattering by two atoms in a waveguide. *Phys. Rev. A*, 96:063826, Dec 2017.

[39] Debsuvra Mukhopadhyay and Girish S. Agarwal. Multiple fano interferences due to waveguide-mediated phase coupling between atoms. *Phys. Rev. A*, 100:013812, Jul 2019.

[40] Debsuvra Mukhopadhyay and Girish S. Agarwal. Transparency in a chain of disparate quantum emitters strongly coupled to a waveguide. *Phys. Rev. A*, 101:063814, Jun 2020.

[41] Yao Zhou, Zihao Chen, and Jung-Tsung Shen. Single-photon superradiant emission rate scaling for atoms trapped in a photonic waveguide. *Phys. Rev. A*, 95:043832, Apr 2017.

[42] Andrew Addison Houck, DI Schuster, JM Gambetta, JA Schreier, BR Johnson, JM Chow, L Frunzio, J Majer, MH Devoret, SM Girvin, et al. Generating single microwave photons in

a circuit. *Nature*, 449(7160):328–331, 2007.

[43] NL Petrov, AB Fedotov, and AM Zheltikov. High-brightness photon pairs and strongly antibunching heralded single photons from a highly nonlinear optical fiber. *Optics Communications*, 450:304–307, 2019.

[44] Li Ge and Hakan E. Türeci. Antisymmetric $\mathcal{PT}$-photonic structures with balanced positive- and negative-index materials. *Phys. Rev. A*, 88:053810, Nov 2013.

[45] Peng Peng, Wanxia Cao, Ce Shen, Weizhi Qu, Jianming Wen, Liang Jiang, and Yanhong Xiao. Anti-parity–time symmetry with flying atoms. *Nature Physics*, 12(12):1139–1145, Dec 2016.

[46] Fan Yang, Yong-Chun Liu, and Li You. Anti-$\mathcal{PT}$ symmetry in dissipatively coupled optical systems. *Phys. Rev. A*, 96:053845, Nov 2017.

[47] Youngsun Choi, Choloong Hahn, Jae Woong Yoon, and Seok Ho Song. Observation of an anti-pt-symmetric exceptional point and energy-difference conserving dynamics in electrical circuit resonators. *Nature Communications*, 9(1):2182, Jun 2018.

[48] Y. Yang, Yi-Pu Wang, J. W. Rao, Y. S. Gui, B. M. Yao, W. Lu, and C.-M. Hu. Unconventional singularity in anti-parity-time symmetric cavity magnonics. *Phys. Rev. Lett.*, 125:147202, Oct 2020.

[49] Huilai Zhang, Ran Huang, Sheng-Dian Zhang, Ying Li, Cheng-Wei Qiu, Franco Nori, and Hui Jing. Breaking anti-pt symmetry by spinning a resonator. *Nano Letters*, 20(10):7594–7599, 2020.

[50] Debsuvra Mukhopadhyay, Jayakrishnan M. P. Nair, and Girish S. Agarwal. Anti-$\mathcal{PT}$ symmetry enhanced interconversion between microwave and optical fields. *Phys. Rev. B*, 105:064405, Feb 2022.

[51] Julian Kelly, Rami Barends, Austin G Fowler, Anthony Megrant, Evan Jeffrey, Theodore C White, Daniel Sank, Josh Y Mutus, Brooks Campbell, Yu Chen, et al. State preservation by repetitive error detection in a superconducting quantum circuit. *Nature*, 519(7541):66–69, 2015.

[52] Frank Arute, Kunal Arya, Ryan Babbush, Dave Bacon, Joseph C Bardin, Rami Barends, Rupak Biswas, Sergio Boixo, Fernando GSL Brandao, David A Buell, et al. Quantum supremacy using a programmable superconducting processor. *Nature*, 574(7779):505–510, 2019.

[53] Rupert Ursin, F Tiefenbacher, T Schmitt-Manderbach, H Weier, Thomas Scheidl, M Lindenthal, B Blauensteiner, T Jennewein, J Perdigues, P Trojek, et al. Entanglement-based quantum communication over 144 km. *Nature physics*, 3(7):481–486, 2007.

[54] Mirko Pittaluga, Mariella Minder, Marco Lucamarini, Mirko Sanzaro, Robert I Woodward, Ming-Jun Li, Zhiliang Yuan, and Andrew J Shields. 600-km repeater-like quantum communications with dual-band stabilization. *Nature Photonics*, 15(7):530–535, 2021.

[55] A. J. Leggett, S. Chakravarty, A. T. Dorsey, Matthew P. A. Fisher, Anupam Garg, and W. Zwerger. Dynamics of the dissipative two-state system. *Rev. Mod. Phys.*, 59:1–85, Jan 1987.

[56] Girish S. Agarwal. *Quantum Optics*. Cambridge University Press, 2012.

[57] R.G. Newton. *Scattering Theory of Waves and Particles*. International series in pure and applied physics. McGraw-Hill, 1966.

[58] Peter Lodahl, Sahand Mahmoodian, Søren Stobbe, Arno Rauschenbeutel, Philipp Schneeweiss, Jürgen Volz, Hannes Pichler, and Peter Zoller. Chiral quantum optics. *Nature*, 541(7638):473–480, Jan 2017.

[59] Itay Shomroni, Serge Rosenblum, Yulia Lovsky, Orel Bechler, Gabriel Guendelman, and Barak Dayan. All-optical routing of single photons by a one-atom switch controlled by a single photon. *Science*, 345(6199):903–906, 2014.

[60] Michael Scheucher, Adèle Hilico, Elisa Will, Jürgen Volz, and Arno Rauschenbeutel. Quantum optical circulator controlled by a single chirally coupled atom. *Science*, 354(6319):1577–1580, 2016.

[61] Stephen Hughes and Girish S. Agarwal. Anisotropy-induced quantum interference and population trapping between orthogonal quantum dot exciton states in semiconductor cavity

systems. *Phys. Rev. Lett.*, 118:063601, Feb 2017.

[62] Andreas Albrecht, Tommaso Caneva, and Darrick E Chang. Changing optical band structure with single photons. *New Journal of Physics*, 19(11):115002, nov 2017.

[63] A. Goban, C.-L. Hung, J. D. Hood, S.-P. Yu, J. A. Muniz, O. Painter, and H. J. Kimble. Superradiance for atoms trapped along a photonic crystal waveguide. *Phys. Rev. Lett.*, 115:063601, Aug 2015.

[64] Neil V. Corzo, Baptiste Gouraud, Aveek Chandra, Akihisa Goban, Alexandra S. Sheremet, Dmitriy V. Kupriyanov, and Julien Laurat. Large bragg reflection from one-dimensional chains of trapped atoms near a nanoscale waveguide. *Phys. Rev. Lett.*, 117:133603, Sep 2016.

[65] H. L. Sørensen, J.-B. Béguin, K. W. Kluge, I. Iakoupov, A. S. Sørensen, J. H. Müller, E. S. Polzik, and J. Appel. Coherent backscattering of light off one-dimensional atomic strings. *Phys. Rev. Lett.*, 117:133604, Sep 2016.

[66] Clément Sayrin, Christian Junge, Rudolf Mitsch, Bernhard Albrecht, Danny O'Shea, Philipp Schneeweiss, Jürgen Volz, and Arno Rauschenbeutel. Nanophotonic optical isolator controlled by the internal state of cold atoms. *Phys. Rev. X*, 5:041036, Dec 2015.

[67] Zeyang Liao, Xiaodong Zeng, Shi-Yao Zhu, and M. Suhail Zubairy. Single-photon transport through an atomic chain coupled to a one-dimensional nanophotonic waveguide. *Phys. Rev. A*, 92:023806, Aug 2015.

[68] Huaixiu Zheng and Harold U. Baranger. Persistent quantum beats and long-distance entanglement from waveguide-mediated interactions. *Phys. Rev. Lett.*, 110:113601, Mar 2013.

[69] Guang-Yin Chen, Neill Lambert, Chung-Hsien Chou, Yueh-Nan Chen, and Franco Nori. Surface plasmons in a metal nanowire coupled to colloidal quantum dots: Scattering properties and quantum entanglement. *Phys. Rev. B*, 84:045310, Jul 2011.

[70] C. Gonzalez-Ballestero, Esteban Moreno, and F. J. Garcia-Vidal. Generation, manipulation, and detection of two-qubit entanglement in waveguide qed. *Phys. Rev. A*, 89:042328, Apr 2014.

[71] Paolo Facchi, M. S. Kim, Saverio Pascazio, Francesco V. Pepe, Domenico Pomarico, and Tommaso Tufarelli. Bound states and entanglement generation in waveguide quantum electrodynamics. *Phys. Rev. A*, 94:043839, Oct 2016.

[72] Imran M. Mirza and John C. Schotland. Multiqubit entanglement in bidirectional-chiral-waveguide qed. *Phys. Rev. A*, 94:012302, Jul 2016.

[73] Xingmin Li and L.F. Wei. Probing a single dipolar interaction between a pair of two-level quantum system by scatterings of single photons in an aside waveguide. *Optics Communications*, 366:163–167, 2016.

[74] D. E. Chang, A. S. Sørensen, P. R. Hemmer, and M. D. Lukin. Quantum optics with surface plasmons. *Phys. Rev. Lett.*, 97:053002, Aug 2006.

[75] V. S. C. Manga Rao and S. Hughes. Single quantum-dot purcell factor and β factor in a photonic crystal waveguide. *Phys. Rev. B*, 75:205437, May 2007.

[76] G. Lecamp, P. Lalanne, and J. P. Hugonin. Very large spontaneous-emission β factors in photonic-crystal waveguides. *Phys. Rev. Lett.*, 99:023902, Jul 2007.

[77] A. V. Akimov, A. Mukherjee, C. L. Yu, D. E. Chang, A. S. Zibrov, P. R. Hemmer, H. Park, and M. D. Lukin. Generation of single optical plasmons in metallic nanowires coupled to quantum dots. *Nature*, 450(7168):402–406, Nov 2007.

[78] Hong Wei, Daniel Ratchford, Xiaoqin (Elaine) Li, Hongxing Xu, and Chih-Kang Shih. Propagating surface plasmon induced photon emission from quantum dots. *Nano Letters*, 9(12):4168–4171, 2009. PMID: 19821597.

[79] Alexander Huck, Shailesh Kumar, Abdul Shakoor, and Ulrik L. Andersen. Controlled coupling of a single nitrogen-vacancy center to a silver nanowire. *Phys. Rev. Lett.*, 106:096801, Feb 2011.

[80] Thomas M. Babinec, Birgit J. M. Hausmann, Mughees Khan, Yinan Zhang, Jeronimo R. Maze, Philip R. Hemmer, and Marko Lončar. A diamond nanowire single-photon source. *Nature Nanotechnology*, 5(3):195–199, Mar 2010.

[81] Julien Claudon, Joël Bleuse, Nitin Singh Malik, Maela Bazin, Périne Jaffrennou, Niels

Gregersen, Christophe Sauvan, Philippe Lalanne, and Jean-Michel Gérard. A highly efficient single-photon source based on a quantum dot in a photonic nanowire. *Nature Photonics*, 4(3):174–177, Mar 2010.

[82] O. Astafiev, A. M. Zagoskin, A. A. Abdumalikov, Yu. A. Pashkin, T. Yamamoto, K. Inomata, Y. Nakamura, and J. S. Tsai. Resonance fluorescence of a single artificial atom. *Science*, 327(5967):840–843, 2010.

[83] Ramachandrarao Yalla, Mark Sadgrove, Kali P. Nayak, and Kohzo Hakuta. Cavity quantum electrodynamics on a nanofiber using a composite photonic crystal cavity. *Phys. Rev. Lett.*, 113:143601, Sep 2014.

[84] A. Javadi, I. Söllner, M. Arcari, S. Lindskov Hansen, L. Midolo, S. Mahmoodian, G. Kiršanskė, T. Pregnolato, E. H. Lee, J. D. Song, S. Stobbe, and P. Lodahl. Single-photon non-linear optics with a quantum dot in a waveguide. *Nature Communications*, 6(1):8655, Oct 2015.

[85] A. Sipahigil, R. E. Evans, D. D. Sukachev, M. J. Burek, J. Borregaard, M. K. Bhaskar, C. T. Nguyen, J. L. Pacheco, H. A. Atikian, C. Meuwly, R. M. Camacho, F. Jelezko, E. Bielejec, H. Park, M. Lončar, and M. D. Lukin. An integrated diamond nanophotonics platform for quantum-optical networks. *Science*, 354(6314):847–850, 2016.

[86] U. Fano. Effects of configuration interaction on intensities and phase shifts. *Phys. Rev.*, 124:1866–1878, Dec 1961.

[87] Andrey E. Miroshnichenko, Sergej Flach, and Yuri S. Kivshar. Fano resonances in nanoscale structures. *Rev. Mod. Phys.*, 82:2257–2298, Aug 2010.

[88] E. Paspalakis and P. L. Knight. Electromagnetically induced transparency and controlled group velocity in a multilevel system. *Phys. Rev. A*, 66:015802, Jul 2002.

[89] E. C. Diniz, H. S. Borges, and C. J. Villas-Boas. Multiple transparency windows and fano interferences induced by dipole-dipole couplings. *Phys. Rev. A*, 97:043848, Apr 2018.

[90] Rohan D. Kekatpure, Edward S. Barnard, Wenshan Cai, and Mark L. Brongersma. Phase-coupled plasmon-induced transparency. *Phys. Rev. Lett.*, 104:243902, Jun 2010.

[91] Zhiwei Guo, Haitao Jiang, Yunhui Li, Hong Chen, and G. S. Agarwal. Enhancement of electromagnetically induced transparency in metamaterials using long range coupling mediated by a hyperbolic material. *Opt. Express*, 26(2):627–641, Jan 2018.

[92] A. Wallraff, D. I. Schuster, A. Blais, L. Frunzio, R.-. S. Huang, J. Majer, S. Kumar, S. M. Girvin, and R. J. Schoelkopf. Strong coupling of a single photon to a superconducting qubit using circuit quantum electrodynamics. *Nature*, 431(7005):162–167, Sep 2004.

[93] Arjan F. van Loo, Arkady Fedorov, Kevin Lalumière, Barry C. Sanders, Alexandre Blais, and Andreas Wallraff. Photon-mediated interactions between distant artificial atoms. *Science*, 342(6165):1494–1496, 2013.

[94] L. Scarpelli, B. Lang, F. Masia, D. M. Beggs, E. A. Muljarov, A. B. Young, R. Oulton, M. Kamp, S. Höfling, C. Schneider, and W. Langbein. 99% beta factor and directional coupling of quantum dots to fast light in photonic crystal waveguides determined by spectral imaging. *Phys. Rev. B*, 100:035311, Jul 2019.

[95] K.-J. Boller, A. Imamoğlu, and S. E. Harris. Observation of electromagnetically induced transparency. *Phys. Rev. Lett.*, 66:2593–2596, May 1991.

[96] Michael Fleischhauer, Atac Imamoglu, and Jonathan P. Marangos. Electromagnetically induced transparency: Optics in coherent media. *Rev. Mod. Phys.*, 77:633–673, Jul 2005.

[97] W D Heiss. The physics of exceptional points. *Journal of Physics A: Mathematical and Theoretical*, 45(44):444016, oct 2012.

[98] N. R. Bernier, L. D. Tóth, A. K. Feofanov, and T. J. Kippenberg. Level attraction in a microwave optomechanical circuit. *Phys. Rev. A*, 98:023841, Aug 2018.

[99] M. Harder, Y. Yang, B. M. Yao, C. H. Yu, J. W. Rao, Y. S. Gui, R. L. Stamps, and C.-M. Hu. Level attraction due to dissipative magnon-photon coupling. *Phys. Rev. Lett.*, 121:137203, Sep 2018.

[100] Carl M. Bender, Mariagiovanna Gianfreda, Şahin K. Özdemir, Bo Peng, and Lan Yang. Twofold transition in $\mathcal{PT}$-symmetric coupled oscillators. *Phys. Rev. A*, 88:062111, Dec 2013.

[101] M. Brandstetter, M. Liertzer, C. Deutsch, P. Klang, J. Schöberl, H. E. Türeci, G. Strasser, K. Unterrainer, and S. Rotter. Reversing the pump dependence of a laser at an exceptional point. *Nature Communications*, 5(1):4034, Jun 2014.

[102] C. Dembowski, H.-D. Gräf, H. L. Harney, A. Heine, W. D. Heiss, H. Rehfeld, and A. Richter. Experimental observation of the topological structure of exceptional points. *Phys. Rev. Lett.*, 86:787–790, Jan 2001.

[103] Jörg Doppler, Alexei A. Mailybaev, Julian Böhm, Ulrich Kuhl, Adrian Girschik, Florian Libisch, Thomas J. Milburn, Peter Rabl, Nimrod Moiseyev, and Stefan Rotter. Dynamically encircling an exceptional point for asymmetric mode switching. *Nature*, 537(7618):76–79, Sep 2016.

[104] H. Xu, D. Mason, Luyao Jiang, and J. G. E. Harris. Topological energy transfer in an optomechanical system with exceptional points. *Nature*, 537(7618):80–83, Sep 2016.

[105] Girish S Agarwal and Debsuvra Mukhopadhyay. Coupling quantum antennas to fibers and waveguides. *arXiv preprint arXiv:2111.03200*, 2021.

[106] E.L. Ivchenko, A.I. Nesvizhskii, and S. Jorda. Resonant bragg reflection from quantum-well structures. *Superlattices and Microstructures*, 16(1):17–20, 1994.

[107] E. L. Ivchenko and A. N. Poddubny. Resonant diffraction of electromagnetic waves from solids (a review). *Physics of the Solid State*, 55(5):905–923, May 2013.

[108] Carl M. Bender and Stefan Boettcher. Real spectra in non-hermitian hamiltonians having PT symmetry. *Phys. Rev. Lett.*, 80:5243–5246, Jun 1998.

[109] Carl M Bender. Making sense of non-hermitian hamiltonians. *Reports on Progress in Physics*, 70(6):947–1018, may 2007.

[110] Ali Mostafazadeh. Pseudo-hermitian representation of quantum mechanics. *International Journal of Geometric Methods in Modern Physics*, 07(07):1191–1306, 2010.

[111] Weijian Chen, Şahin Kaya Özdemir, Guangming Zhao, Jan Wiersig, and Lan Yang. Exceptional points enhance sensing in an optical microcavity. *Nature*, 548(7666):192–196, Aug 2017.

[112] Hossein Hodaei, Absar U. Hassan, Steffen Wittek, Hipolito Garcia-Gracia, Ramy El-Ganainy, Demetrios N. Christodoulides, and Mercedeh Khajavikhan. Enhanced sensitivity at higher-order exceptional points. *Nature*, 548(7666):187–191, Aug 2017.

[113] Mohammad-Ali Miri and Andrea Alù. Exceptional points in optics and photonics. *Science*, 363(6422):eaar7709, 2019.

[114] Christian E. Rüter, Konstantinos G. Makris, Ramy El-Ganainy, Demetrios N. Christodoulides, Mordechai Segev, and Detlef Kip. Observation of parity–time symmetry in optics. *Nature Physics*, 6(3):192–195, Mar 2010.

[115] Alois Regensburger, Christoph Bersch, Mohammad-Ali Miri, Georgy Onishchukov, Demetrios N. Christodoulides, and Ulf Peschel. Parity–time synthetic photonic lattices. *Nature*, 488(7410):167–171, Aug 2012.

[116] Bo Peng, Şahin Kaya Özdemir, Fuchuan Lei, Faraz Monifi, Mariagiovanna Gianfreda, Gui Lu Long, Shanhui Fan, Franco Nori, Carl M. Bender, and Lan Yang. Parity–time-symmetric whispering-gallery microcavities. *Nature Physics*, 10(5):394–398, May 2014.

[117] Liang Feng, Maurice Ayache, Jingqing Huang, Ye-Long Xu, Ming-Hui Lu, Yan-Feng Chen, Yeshaiahu Fainman, and Axel Scherer. Nonreciprocal light propagation in a silicon photonic circuit. *Science*, 333(6043):729–733, 2011.

[118] Stefano Longhi. $\mathcal{PT}$-symmetric laser absorber. *Phys. Rev. A*, 82:031801, Sep 2010.

[119] Y. D. Chong, Li Ge, and A. Douglas Stone. $\mathcal{PT}$-symmetry breaking and laser-absorber modes in optical scattering systems. *Phys. Rev. Lett.*, 106:093902, Mar 2011.

[120] Alexander Cerjan, Aaswath Raman, and Shanhui Fan. Exceptional contours and band structure design in parity-time symmetric photonic crystals. *Phys. Rev. Lett.*, 116:203902, May 2016.

[121] Zhong-Peng Liu, Jing Zhang, Şahin Kaya Özdemir, Bo Peng, Hui Jing, Xin-You Lü, Chun-Wen Li, Lan Yang, Franco Nori, and Yu-xi Liu. Metrology with $\mathcal{PT}$-symmetric cavities: Enhanced sensitivity near the $\mathcal{PT}$-phase transition. *Phys. Rev. Lett.*, 117:110802, Sep 2016.

[122] Vassilios Yannopapas. Topological photonic bands in two-dimensional networks of meta-

material elements. *New Journal of Physics*, 14(11):113017, nov 2012.

[123] Vassilios Yannopapas. Spontaneous $\mathcal{PT}$-symmetry breaking in complex frequency band structures. *Phys. Rev. A*, 89:013808, Jan 2014.

[124] Jin-Hui Wu, M. Artoni, and G. C. La Rocca. Non-hermitian degeneracies and unidirectional reflectionless atomic lattices. *Phys. Rev. Lett.*, 113:123004, Sep 2014.

[125] Diana A. Antonosyan, Alexander S. Solntsev, and Andrey A. Sukhorukov. Parity-time anti-symmetric parametric amplifier. *Opt. Lett.*, 40(20):4575–4578, Oct 2015.

[126] Xin Wang and Jin-Hui Wu. Optical $\mathcal{PT}$-symmetry and $\mathcal{PT}$-antisymmetry in coherently driven atomic lattices. *Optics express*, 24(4):4289–4298, 2016.

[127] You-Lin Chuang, Ziauddin, and Ray-Kuang Lee. Realization of simultaneously parity-time-symmetric and parity-time-antisymmetric susceptibilities along the longitudinal direction in atomic systems with all optical controls. *Opt. Express*, 26(17):21969–21978, Aug 2018.

[128] Yue Jiang, Yefeng Mei, Ying Zuo, Yanhua Zhai, Jensen Li, Jianming Wen, and Shengwang Du. Anti-parity-time symmetric optical four-wave mixing in cold atoms. *Phys. Rev. Lett.*, 123:193604, Nov 2019.

[129] Vladimir V. Konotop and Dmitry A. Zezyulin. Odd-time reversal $\mathcal{PT}$ symmetry induced by an anti-$\mathcal{PT}$-symmetric medium. *Phys. Rev. Lett.*, 120:123902, Mar 2018.

[130] Ying Li, Yu-Gui Peng, Lei Han, Mohammad-Ali Miri, Wei Li, Meng Xiao, Xue-Feng Zhu, Jianlin Zhao, Andrea Alù, Shanhui Fan, et al. Anti-parity-time symmetry in diffusive systems. *Science*, 364(6436):170–173, 2019.

[131] Jingwei Wen, Guoqing Qin, Chao Zheng, Shijie Wei, Xiangyu Kong, Tao Xin, and Guilu Long. Observation of information flow in the anti-PT symmetric system with nuclear spins. *npj Quantum Information*, 6(1):28, Mar 2020.

[132] C. Kittel. *Quantum Theory of Solids*. Wiley, 1987.

[133] Charles Kittel. On the theory of ferromagnetic resonance absorption. *Phys. Rev.*, 73:155–161, Jan 1948.

[134] Andrii V. Chumak, Alexander A. Serga, and Burkard Hillebrands. Magnon transistor for

all-magnon data processing. *Nature Communications*, 5(1):4700, Aug 2014.

[135] A. V. Chumak, V. I. Vasyuchka, A. A. Serga, and B. Hillebrands. Magnon spintronics. *Nature Physics*, 11(6):453–461, Jun 2015.

[136] Yutaka Tabuchi, Seiichiro Ishino, Toyofumi Ishikawa, Rekishu Yamazaki, Koji Usami, and Yasunobu Nakamura. Hybridizing ferromagnetic magnons and microwave photons in the quantum limit. *Phys. Rev. Lett.*, 113:083603, Aug 2014.

[137] Xufeng Zhang, Chang-Ling Zou, Liang Jiang, and Hong X. Tang. Strongly coupled magnons and cavity microwave photons. *Phys. Rev. Lett.*, 113:156401, Oct 2014.

[138] Jie Li, Shi-Yao Zhu, and G. S. Agarwal. Magnon-photon-phonon entanglement in cavity magnomechanics. *Phys. Rev. Lett.*, 121:203601, Nov 2018.

[139] Zhedong Zhang, Marlan O. Scully, and Girish S. Agarwal. Quantum entanglement between two magnon modes via kerr nonlinearity driven far from equilibrium. *Phys. Rev. Research*, 1:023021, Sep 2019.

[140] Yutaka Tabuchi, Seiichiro Ishino, Atsushi Noguchi, Toyofumi Ishikawa, Rekishu Yamazaki, Koji Usami, and Yasunobu Nakamura. Coherent coupling between a ferromagnetic magnon and a superconducting qubit. *Science*, 349(6246):405–408, 2015.

[141] J. Bourhill, N. Kostylev, M. Goryachev, D. L. Creedon, and M. E. Tobar. Ultrahigh cooperativity interactions between magnons and resonant photons in a yig sphere. *Phys. Rev. B*, 93:144420, Apr 2016.

[142] Biswanath Bhoi, Bosung Kim, Seung-Hun Jang, Junhoe Kim, Jaehak Yang, Young-Jun Cho, and Sang-Koog Kim. Abnormal anticrossing effect in photon-magnon coupling. *Phys. Rev. B*, 99:134426, Apr 2019.

[143] Y. Yang, J.W. Rao, Y.S. Gui, B.M. Yao, W. Lu, and C.-M. Hu. Control of the magnon-photon level attraction in a planar cavity. *Phys. Rev. Applied*, 11:054023, May 2019.

[144] J W Rao, C H Yu, Y T Zhao, Y S Gui, X L Fan, D S Xue, and C-M Hu. Level attraction and level repulsion of magnon coupled with a cavity anti-resonance. *New Journal of Physics*, 21(6):065001, jun 2019.

[145] Peng-Chao Xu, J. W. Rao, Y. S. Gui, Xiaofeng Jin, and C.-M. Hu. Cavity-mediated dissipative coupling of distant magnetic moments: Theory and experiment. *Phys. Rev. B*, 100:094415, Sep 2019.

[146] Weichao Yu, Jiongjie Wang, H. Y. Yuan, and Jiang Xiao. Prediction of attractive level crossing via a dissipative mode. *Phys. Rev. Lett.*, 123:227201, Nov 2019.

[147] Jayakrishnan MP Nair, Debsuvra Mukhopadhyay, and Girish S Agarwal. Cavity mediated level attraction and repulsion between magnons. *arXiv preprint arXiv:2201.05685*, 2022.

[148] Jie Li, Shi-Yao Zhu, and G. S. Agarwal. Squeezed states of magnons and phonons in cavity magnomechanics. *Phys. Rev. A*, 99:021801, Feb 2019.

[149] Jie Li and Shi-Yao Zhu. Entangling two magnon modes via magnetostrictive interaction. *New Journal of Physics*, 21(8):085001, aug 2019.

[150] Yi-Pu Wang, Guo-Qiang Zhang, Dengke Zhang, Tie-Fu Li, C.-M. Hu, and J. Q. You. Bistability of cavity magnon polaritons. *Phys. Rev. Lett.*, 120:057202, Jan 2018.

[151] Jayakrishnan M. P. Nair, Zhedong Zhang, Marlan O. Scully, and Girish S. Agarwal. Nonlinear spin currents. *Phys. Rev. B*, 102:104415, Sep 2020.

[152] Lihui Bai, Michael Harder, Paul Hyde, Zhaohui Zhang, Can-Ming Hu, Y. P. Chen, and John Q. Xiao. Cavity mediated manipulation of distant spin currents using a cavity-magnon-polariton. *Phys. Rev. Lett.*, 118:217201, May 2017.

[153] P. Hyde, B. M. Yao, Y. S. Gui, Guo-Qiang Zhang, J. Q. You, and C.-M. Hu. Direct measurement of foldover in cavity magnon-polariton systems. *Phys. Rev. B*, 98:174423, Nov 2018.

[154] Jayakrishnan M. P. Nair, Debsuvra Mukhopadhyay, and Girish S. Agarwal. Ultralow threshold bistability and generation of long-lived mode in a dissipatively coupled nonlinear system: Application to magnonics. *Phys. Rev. B*, 103:224401, Jun 2021.

[155] GuoQiang Zhang, YiPu Wang, and JianQiang You. Theory of the magnon kerr effect in cavity magnonics. *Science China Physics, Mechanics & Astronomy*, 62(8):987511, Mar 2019.

[156] Eduardo Gil-Santos, Daniel Ramos, Javier Martínez, Marta Fernández-Regúlez, Ricardo García, Álvaro San Paulo, Montserrat Calleja, and Javier Tamayo. Nanomechanical mass sensing and stiffness spectrometry based on two-dimensional vibrations of resonant nanowires. *Nature Nanotechnology*, 5(9):641–645, Sep 2010.

[157] Jiangang Zhu, Sahin Kaya Ozdemir, Yun-Feng Xiao, Lin Li, Lina He, Da-Ren Chen, and Lan Yang. On-chip single nanoparticle detection and sizing by mode splitting in an ultrahigh-q microresonator. *Nature Photonics*, 4(1):46–49, Jan 2010.

[158] Lina He, Şahin Kaya Özdemir, Jiangang Zhu, Woosung Kim, and Lan Yang. Detecting single viruses and nanoparticles using whispering gallery microlasers. *Nature Nanotechnology*, 6(7):428–432, Jul 2011.

[159] Frank Vollmer and Lan Yang. Review label-free detection with high-q microcavities: a review of biosensing mechanisms for integrated devices. *Nanophotonics*, 1(3-4):267–291, 2012.

[160] S. Forstner, S. Prams, J. Knittel, E. D. van Ooijen, J. D. Swaim, G. I. Harris, A. Szorkovszky, W. P. Bowen, and H. Rubinsztein-Dunlop. Cavity optomechanical magnetometer. *Phys. Rev. Lett.*, 108:120801, Mar 2012.

[161] L Rondin, J-P Tetienne, T Hingant, J-F Roch, P Maletinsky, and V Jacques. Magnetometry with nitrogen-vacancy defects in diamond. *Reports on Progress in Physics*, 77(5):056503, may 2014.

[162] W. W. Chow, J. Gea-Banacloche, L. M. Pedrotti, V. E. Sanders, W. Schleich, and M. O. Scully. The ring laser gyro. *Rev. Mod. Phys.*, 57:61–104, Jan 1985.

[163] Jan Wiersig. Enhancing the sensitivity of frequency and energy splitting detection by using exceptional points: Application to microcavity sensors for single-particle detection. *Phys. Rev. Lett.*, 112:203901, May 2014.

[164] Jan Wiersig. Sensors operating at exceptional points: General theory. *Phys. Rev. A*, 93:033809, Mar 2016.

[165] Xufeng Zhang, Kun Ding, Xianjing Zhou, Jing Xu, and Dafei Jin. Experimental observation

of an exceptional surface in synthetic dimensions with magnon polaritons. *Phys. Rev. Lett.*, 123:237202, Dec 2019.

[166] Chao Zeng, Yong Sun, Guo Li, Yunhui Li, Haitao Jiang, Yaping Yang, and Hong Chen. Enhanced sensitivity at high-order exceptional points in a passive wireless sensing system. *Opt. Express*, 27(20):27562–27572, Sep 2019.

[167] Zhicheng Xiao, Huanan Li, Tsampikos Kottos, and Andrea Alù. Enhanced sensing and nondegraded thermal noise performance based on $\mathcal{PT}$-symmetric electronic circuits with a sixth-order exceptional point. *Phys. Rev. Lett.*, 123:213901, Nov 2019.

[168] Jayakrishnan M. P. Nair, Debsuvra Mukhopadhyay, and G. S. Agarwal. Enhanced sensing of weak anharmonicities through coherences in dissipatively coupled anti-pt symmetric systems. *Phys. Rev. Lett.*, 126:180401, May 2021.

[169] G. S. Agarwal. Anisotropic vacuum-induced interference in decay channels. *Phys. Rev. Lett.*, 84:5500–5503, Jun 2000.

[170] Pankaj K. Jha, Xingjie Ni, Chihhui Wu, Yuan Wang, and Xiang Zhang. Metasurface-enabled remote quantum interference. *Phys. Rev. Lett.*, 115:025501, Jul 2015.

[171] Emmanuel Lassalle, Philippe Lalanne, Syed Aljunid, Patrice Genevet, Brian Stout, Thomas Durt, and David Wilkowski. Long-lifetime coherence in a quantum emitter induced by a metasurface. *Phys. Rev. A*, 101:013837, Jan 2020.

[172] Danil Kornovan, Mihail Petrov, and Ivan Iorsh. Noninverse dynamics of a quantum emitter coupled to a fully anisotropic environment. *Phys. Rev. A*, 100:033840, Sep 2019.

[173] Marlan O. Scully, Kimberly R. Chapin, Konstantin E. Dorfman, Moochan Barnabas Kim, and Anatoly Svidzinsky. Quantum heat engine power can be increased by noise-induced coherence. *Proceedings of the National Academy of Sciences*, 108(37):15097–15100, 2011.

[174] C. H. Keitel. Narrowing spontaneous emission without intensity reduction. *Phys. Rev. Lett.*, 83:1307–1310, Aug 1999.

[175] Peng Zhou and S. Swain. Quantum interference in resonance fluorescence for a driven v atom. *Phys. Rev. A*, 56:3011–3021, Oct 1997.

[176] E. Paspalakis and P. L. Knight. Phase control of spontaneous emission. *Phys. Rev. Lett.*, 81:293–296, Jul 1998.

[177] E. Paspalakis, C. H. Keitel, and P. L. Knight. Fluorescence control through multiple interference mechanisms. *Phys. Rev. A*, 58:4868–4877, Dec 1998.

[178] Kilian P. Heeg, Hans-Christian Wille, Kai Schlage, Tatyana Guryeva, Daniel Schumacher, Ingo Uschmann, Kai S. Schulze, Berit Marx, Tino Kämpfer, Gerhard G. Paulus, Ralf Röhlsberger, and Jörg Evers. Vacuum-assisted generation and control of atomic coherences at x-ray energies. *Phys. Rev. Lett.*, 111:073601, Aug 2013.

[179] Konstantin E. Dorfman, Dmitri V. Voronine, Shaul Mukamel, and Marlan O. Scully. Photosynthetic reaction center as a quantum heat engine. *Proceedings of the National Academy of Sciences*, 110(8):2746–2751, 2013.

[180] Marlan O. Scully. Quantum photocell: Using quantum coherence to reduce radiative recombination and increase efficiency. *Phys. Rev. Lett.*, 104:207701, May 2010.

[181] Amro Dodin and Paul Brumer. Light-induced processes in nature: Coherences in the establishment of the nonequilibrium steady state in model retinal isomerization. *The Journal of Chemical Physics*, 150(18):184304, 2019.

[182] Jens Koch, Terri M. Yu, Jay Gambetta, A. A. Houck, D. I. Schuster, J. Majer, Alexandre Blais, M. H. Devoret, S. M. Girvin, and R. J. Schoelkopf. Charge-insensitive qubit design derived from the cooper pair box. *Phys. Rev. A*, 76:042319, Oct 2007.

[183] Jan Wiersig. Prospects and fundamental limits in exceptional point-based sensing. *Nature Communications*, 11(1):2454, May 2020.

[184] J. W. Rao, Y. P. Wang, Y. Yang, T. Yu, Y. S. Gui, X. L. Fan, D. S. Xue, and C.-M. Hu. Interactions between a magnon mode and a cavity photon mode mediated by traveling photons. *Phys. Rev. B*, 101:064404, Feb 2020.

[185] R. W. Andrews, R. W. Peterson, T. P. Purdy, K. Cicak, R. W. Simmonds, C. A. Regal, and K. W. Lehnert. Bidirectional and efficient conversion between microwave and optical light. *Nature Physics*, 10(4):321–326, Apr 2014.

[186] G. S. Agarwal and Sudhanshu S. Jha. Multimode phonon cooling via three-wave parametric interactions with optical fields. *Phys. Rev. A*, 88:013815, Jul 2013.

[187] Kenan Qu and G. S. Agarwal. Phonon-mediated electromagnetically induced absorption in hybrid opto-electromechanical systems. *Phys. Rev. A*, 87:031802, Mar 2013.

[188] T. Bagci, A. Simonsen, S. Schmid, L. G. Villanueva, E. Zeuthen, J. Appel, J. M. Taylor, A. Sørensen, K. Usami, A. Schliesser, and E. S. Polzik. Optical detection of radio waves through a nanomechanical transducer. *Nature*, 507(7490):81–85, Mar 2014.

[189] M. Hafezi, Z. Kim, S. L. Rolston, L. A. Orozco, B. L. Lev, and J. M. Taylor. Atomic interface between microwave and optical photons. *Phys. Rev. A*, 85:020302, Feb 2012.

[190] J. Verdú, H. Zoubi, Ch. Koller, J. Majer, H. Ritsch, and J. Schmiedmayer. Strong magnetic coupling of an ultracold gas to a superconducting waveguide cavity. *Phys. Rev. Lett.*, 103:043603, Jul 2009.

[191] Atac Imamoğlu. Cavity qed based on collective magnetic dipole coupling: Spin ensembles as hybrid two-level systems. *Phys. Rev. Lett.*, 102:083602, Feb 2009.

[192] D. Marcos, M. Wubs, J. M. Taylor, R. Aguado, M. D. Lukin, and A. S. Sørensen. Coupling nitrogen-vacancy centers in diamond to superconducting flux qubits. *Phys. Rev. Lett.*, 105:210501, Nov 2010.

[193] Lewis A. Williamson, Yu-Hui Chen, and Jevon J. Longdell. Magneto-optic modulator with unit quantum efficiency. *Phys. Rev. Lett.*, 113:203601, Nov 2014.

[194] Xavier Fernandez-Gonzalvo, Yu-Hui Chen, Chunming Yin, Sven Rogge, and Jevon J. Longdell. Coherent frequency up-conversion of microwaves to the optical telecommunications band in an er:yso crystal. *Phys. Rev. A*, 92:062313, Dec 2015.

[195] Mankei Tsang. Cavity quantum electro-optics. *Phys. Rev. A*, 81:063837, Jun 2010.

[196] Mankei Tsang. Cavity quantum electro-optics. ii. input-output relations between traveling optical and microwave fields. *Phys. Rev. A*, 84:043845, Oct 2011.

[197] A. Osada, R. Hisatomi, A. Noguchi, Y. Tabuchi, R. Yamazaki, K. Usami, M. Sadgrove, R. Yalla, M. Nomura, and Y. Nakamura. Cavity optomagnonics with spin-orbit coupled

photons. *Phys. Rev. Lett.*, 116:223601, Jun 2016.

[198] Xufeng Zhang, Na Zhu, Chang-Ling Zou, and Hong X. Tang. Optomagnonic whispering gallery microresonators. *Phys. Rev. Lett.*, 117:123605, Sep 2016.

[199] J. A. Haigh, A. Nunnenkamp, A. J. Ramsay, and A. J. Ferguson. Triple-resonant brillouin light scattering in magneto-optical cavities. *Phys. Rev. Lett.*, 117:133602, Sep 2016.

[200] R. Hisatomi, A. Osada, Y. Tabuchi, T. Ishikawa, A. Noguchi, R. Yamazaki, K. Usami, and Y. Nakamura. Bidirectional conversion between microwave and light via ferromagnetic magnons. *Phys. Rev. B*, 93:174427, May 2016.

[201] Yong Sup Ihn, Su-Yong Lee, Dongkyu Kim, Sin Hyuk Yim, and Zaeill Kim. Coherent multimode conversion from microwave to optical wave via a magnon-cavity hybrid system. *Phys. Rev. B*, 102:064418, Aug 2020.

[202] A. Metelmann and A. A. Clerk. Nonreciprocal photon transmission and amplification via reservoir engineering. *Phys. Rev. X*, 5:021025, Jun 2015.

[203] Ewold Verhagen and Andrea Alù. Optomechanical nonreciprocity. *Nature Physics*, 13(10):922–924, Oct 2017.

[204] Hussein Nassar, Behrooz Yousefzadeh, Romain Fleury, Massimo Ruzzene, Andrea Alù, Chiara Daraio, Andrew N Norris, Guoliang Huang, and Michael R Haberman. Nonreciprocity in acoustic and elastic materials. *Nature Reviews Materials*, 5(9):667–685, 2020.

[205] Changqing Wang, Xuefeng Jiang, William R Sweeney, Chia Wei Hsu, Yiming Liu, Guangming Zhao, Bo Peng, Mengzhen Zhang, Liang Jiang, A Douglas Stone, et al. Induced transparency by interference or polarization. *Proceedings of the National Academy of Sciences*, 118(3), 2021.

[206] Robert W Boyd. *Nonlinear optics*. Academic press, 2020.

[207] EJ Woodbury and WK Ng. Ruby laser operation in near ir. *Proceedings of the Institute of Radio Engineers*, 50(11):2367, 1962.

[208] E. Garmire, F. Pandarese, and C. H. Townes. Coherently driven molecular vibrations and light modulation. *Phys. Rev. Lett.*, 11:160–163, Aug 1963.

[209] N. Bloembergen and Y. R. Shen. Coupling between vibrations and light waves in raman laser media. *Phys. Rev. Lett.*, 12:504–507, May 1964.

[210] Y. R. Shen and N. Bloembergen. Theory of stimulated brillouin and raman scattering. *Phys. Rev.*, 137:A1787–A1805, Mar 1965.

[211] Y. R. Shen and N. Bloembergen. Interaction between light waves and spin waves. *Phys. Rev.*, 143:372–384, Mar 1966.

[212] W. Happer and B. S. Mathur. Effective operator formalism in optical pumping. *Phys. Rev.*, 163:12–25, Nov 1967.

[213] Klemens Hammerer, Anders S. Sørensen, and Eugene S. Polzik. Quantum interface between light and atomic ensembles. *Rev. Mod. Phys.*, 82:1041–1093, Apr 2010.

[214] JF Dillon Jr, H Kamimura, and JP Remeika. Magneto-optical studies of chromium tribromide. *Journal of Applied Physics*, 34(4):1240–1245, 1963.

[215] Alexandre Blais, Ren-Shou Huang, Andreas Wallraff, S. M. Girvin, and R. J. Schoelkopf. Cavity quantum electrodynamics for superconducting electrical circuits: An architecture for quantum computation. *Phys. Rev. A*, 69:062320, Jun 2004.

[216] Huaixiu Zheng, Daniel J. Gauthier, and Harold U. Baranger. Waveguide-qed-based photonic quantum computation. *Phys. Rev. Lett.*, 111:090502, Aug 2013.

[217] Vanessa Paulisch, HJ Kimble, and Alejandro González-Tudela. Universal quantum computation in waveguide qed using decoherence free subspaces. *New Journal of Physics*, 18(4):043041, 2016.

[218] Anthony Laing, Alberto Peruzzo, Alberto Politi, Maria Rodas Verde, Matthaeus Halder, Timothy C Ralph, Mark G Thompson, and Jeremy L O'Brien. High-fidelity operation of quantum photonic circuits. *Applied Physics Letters*, 97(21):211109, 2010.

[219] Linda Sansoni, Fabio Sciarrino, Giuseppe Vallone, Paolo Mataloni, Andrea Crespi, Roberta Ramponi, and Roberto Osellame. Polarization entangled state measurement on a chip. *Phys. Rev. Lett.*, 105:200503, Nov 2010.

[220] Jianwei Wang, Stefano Paesani, Yunhong Ding, Raffaele Santagati, Paul Skrzypczyk,

Alexia Salavrakos, Jordi Tura, Remigiusz Augusiak, Laura Mančinska, Davide Bacco, et al. Multidimensional quantum entanglement with large-scale integrated optics. *Science*, 360(6386):285–291, 2018.

[221] Yu He, X. Ding, Z.-E. Su, H.-L. Huang, J. Qin, C. Wang, S. Unsleber, C. Chen, H. Wang, Y.-M. He, X.-L. Wang, W.-J. Zhang, S.-J. Chen, C. Schneider, M. Kamp, L.-X. You, Z. Wang, S. Höfling, Chao-Yang Lu, and Jian-Wei Pan. Time-bin-encoded boson sampling with a single-photon device. *Phys. Rev. Lett.*, 118:190501, May 2017.

[222] Jung-Tsung Shen and Shanhui Fan. Strongly correlated multiparticle transport in one dimension through a quantum impurity. *Phys. Rev. A*, 76:062709, Dec 2007.

[223] Huaixiu Zheng, Daniel J. Gauthier, and Harold U. Baranger. Waveguide qed: Many-body bound-state effects in coherent and fock-state scattering from a two-level system. *Phys. Rev. A*, 82:063816, Dec 2010.

[224] Eden Rephaeli and Shanhui Fan. Stimulated emission from a single excited atom in a waveguide. *Phys. Rev. Lett.*, 108:143602, Apr 2012.

[225] Io-Chun Hoi, Tauno Palomaki, Joel Lindkvist, Göran Johansson, Per Delsing, and C. M. Wilson. Generation of nonclassical microwave states using an artificial atom in 1d open space. *Phys. Rev. Lett.*, 108:263601, Jun 2012.

APPENDIX A

SINGLE-PHOTON TRANSPORT: WAVEGUIDE QED

In this appendix, we present some derivations related to the real-space formalism of single-photon transport in a 1D waveguide.

A.1 Real-space Hamiltonian of waveguide modes

The field energy is written in $k-$space as

$$\mathcal{H}_0^{(\text{field})} = \int \mathrm{d}k\, \hbar v_g k \Big(a_R^\dagger(k) a_R(k) - a_L(k)^\dagger a_L(k) \Big) \tag{A.1}$$

Substituting the Fourier decomposition of the mode operators embodied into Eq. (2.5), we obtain, for the contribution from the right-propagating modes

$$\begin{aligned}
\mathcal{H}_0^{(R)} &= \frac{1}{2\pi} \int \mathrm{d}k\, \hbar v_g k \int\int \mathrm{d}x\, \mathrm{d}x'\, a_R^\dagger(x) a_R(x') e^{ik(x-x')} \\
&= \frac{1}{2\pi} \int\int \mathrm{d}x\, \mathrm{d}x' \int \mathrm{d}k\, \hbar v_g k e^{ik(x-x')} a_R^\dagger(x) a_R(x') \\
&= \frac{i}{2\pi} \int\int \mathrm{d}x\, \mathrm{d}x' \int \mathrm{d}k\, \hbar v_g \frac{\partial}{\partial x'} \Big(e^{ik(x-x')} \Big) a_R^\dagger(x) a_R(x') \\
&= \frac{i\hbar v_g}{2\pi} \int\int \mathrm{d}x\, \mathrm{d}x'\, a_R^\dagger(x) a_R(x') \frac{\partial}{\partial x'} \Big(\int \mathrm{d}k\, e^{ik(x-x')} \Big) \\
&= i\hbar v_g \int \mathrm{d}x\, a_R^\dagger(x) \int \mathrm{d}x'\, a_R(x') \frac{\partial}{\partial x'} \delta(x-x') \\
&= -i\hbar v_g \int \mathrm{d}x\, a_R^\dagger(x) \int \mathrm{d}x'\, \delta(x-x') \frac{\partial}{\partial x'} a_R(x') \\
&= -i\hbar v_g \int \mathrm{d}x\, a_R^\dagger(x) \frac{\partial}{\partial x} a_R(x).
\end{aligned} \tag{A.2}$$

We have used the property $\lim_{x'\to\pm\infty} a_R(x') = 0$ and integrated by parts to get the penultimate step above, i.e., $\int \mathrm{d}x'\, a_R(x')\dfrac{\partial}{\partial x'}\delta(x-x') = -\int \mathrm{d}x'\, \delta(x-x')\dfrac{\partial}{\partial x'}a_R(x')$. A similar treatment yields

$$\mathcal{H}_0^{(L)} = i\hbar v_g \int \mathrm{d}x\, a_L^\dagger(x)\frac{\partial}{\partial x}a_L(x) \tag{A.3}$$

Combining (A.2) and (A.3) verifies Eq. 2.6.

A.2 Obtaining the single-atom reflection and transmission

On substituting the plane-wave solutions for $\psi_{R,k}$ and $\psi_{L,k}$ from (2.26) into their corresponding differential equations in (2.26), we find

$$\begin{aligned} -iv_g(t_k - 1) + \mathcal{J}c_k &= 0, \\ iv_g r_k + \mathcal{J}c_k &= 0. \end{aligned} \tag{A.4}$$

More precisely, one can integrate the differential equations $\left(-iv_g\dfrac{\partial}{\partial x} - v_g k\right)\psi_{R,k}(x) + \mathcal{J}c_k\delta(x) = 0$ and $\left(iv_g\dfrac{\partial}{\partial x} - v_g k\right)\psi_{L,k}(x) + \mathcal{J}c_k\delta(x) = 0$ from $x-\epsilon$ to $x+\epsilon$, and then take the limit $\epsilon \to 0$, while keeping $\epsilon > 0$. Such a limiting calculation yields $-iv_g\Big(\psi_{R,k}(0^+) - \psi_{R,k}(0^-)\Big) + \mathcal{J}c_k = 0$ and $iv_g\Big(\psi_{L,k}(0^+) - \psi_{L,k}(0^-)\Big) + \mathcal{J}c_k = 0$, where $f(0^\pm)$ define the limiting values

$$\lim_{\substack{\epsilon\to 0 \\ \epsilon>0}} f(\pm\epsilon).$$

Next, to solve the third equation in (2.25), we need the values of the wave functions at the location of the atom. However, the wave functions are discontinuous at these points. One therefore resorts

to a regularization procedure whereby they introduced the *regularized* functions

$$\tilde{\psi}_{R,k}(0) = \frac{1}{2}(\psi_{R,k}(0^+) + \psi_{R,k}(0^-)),$$
$$\tilde{\psi}_{L,k}(0) = \frac{1}{2}(\psi_{L,k}(0^+) + \psi_{L,k}(0^-)). \tag{A.5}$$

where the tilde-notation has been used to indicate regularized wave-functions which are continuous and well-defined at atomic location. Upon this redefinition, we obtain the values

$$\tilde{\psi}_{R,k}(0) = \frac{t_k + 1}{2},$$
$$\tilde{\psi}_{L,k}(0) = \frac{r_k}{2}. \tag{A.6}$$

Using these regularized forms in the final equation of (2.25), we find

$$c_k = \frac{\mathcal{J}(t_k + r_k + 1)}{2\Delta_k} \tag{A.7}$$

Solving (A.4) and (A.7) jointly leads to the expressions in Eq. (2.28).

A.3 Interaction Hamiltonian for arbitrary N

For $N > 1$, the coupling constant $\mathcal{J}_k$, originally introduced for a single atom at $x = 0$, would be superseded by the forms

$$\mathcal{J}_k^{(j)} = \left(\frac{\hbar\omega(k)}{2\varepsilon_0 V}\right)^{1/2} e^{ikx_j}\mathbf{p}_j \cdot \hat{e}_k, \tag{A.8}$$

where $\mathbf{p}_j$ is the dipole-moment vector of the jth atom. The phases carry information about the location of the different atoms. The corresponding interaction Hamiltonian in $k-$space goes as

$$\int \mathrm{d}k\, \hbar\mathcal{J}_k^{(j)}(a_k^\dagger \left|g\right\rangle_j \left\langle e\right| + a_k \left|e\right\rangle_j \left\langle g\right|) \tag{A.9}$$

Upon transitioning to real space, this becomes

$$\mathcal{H}_{\text{int}} = \int \mathrm{d}x\, \hbar \mathcal{J}^{(j)}(x) \left[\left(a_R^\dagger(x) + a_L^\dagger(x) \right) |g\rangle_j \langle e| + \left(a_R(x) + a_L(x) \right) |e\rangle_j \langle g| \right] \tag{A.10}$$

where we have, now, the Fourier transform of $\mathcal{J}_k^{(j)}$ defined via

$$\mathcal{J}_k^{(j)} = \frac{1}{\sqrt{2\pi}} \int_{-\infty}^{\infty} \mathrm{d}x\, \mathcal{J}^{(j)}(x) e^{ikx} \tag{A.11}$$

Now, the factor $\left(\dfrac{\hbar\omega(k)}{2\varepsilon_0 V} \right)^{1/2}$ is slowly varying, while the phase factors e^{ikx_j} represent fast oscillations. Furthermore, when one assumes the dipole-moment elements to be identical for all the atoms, it is posible to replace the function $\mathcal{J}_k^{(j)}$ by

$$\mathcal{J}_k^{(j)} \approx \frac{\mathcal{J}}{\sqrt{2\pi}} e^{ikx_j} \tag{A.12}$$

where $\mathcal{J}$ is essentially a constant. Substituting (A.12) into (A.11), we obtain

$$\mathcal{J}^{(j)}(x) = \mathcal{J}\delta(x - x_j) \tag{A.13}$$

Plugging these into (A.10) verifies the generalized real-space interaction Hamiltonian for a chain of N 2LAs expressed in (2.30).

A.4 Derivation of N-atom reflection and transmission

We next show how the system of equations in (2.33) leads to the simultaneous, linear equations in (2.36). Integrating the differential equations in (2.33) between $x_j - \epsilon$ and $x_j + \epsilon$, and letting

$\epsilon \to 0$ ($\epsilon > 0$) we obtain

$$-iv_g\Big(\psi_{R,k}(x_j^+) - \psi_{R,k}(x_j^-)\Big) + \mathcal{J}c_k = 0,$$
$$iv_g\Big(\psi_{L,k}(x_j^+) - \psi_{L,k}(x_j^-)\Big) + \mathcal{J}c_k = 0. \tag{A.14}$$

Invoking the plane-wave expressions listed in (2.34) and (2.35), we are led to the respective coupled equations

$$t_j e^{-ikL} - t_{j-1} + \frac{i\mathcal{J}c_k^{(j)}}{v_g} = 0, \tag{A.15}$$
$$r_{j+1}e^{ikL} - r_j - \frac{i\mathcal{J}c_k^{(j)}}{v_g} = 0. \tag{A.16}$$

In addition, when one uses the same regularization technique as employed for the case of a single atom, the following regularized values of the wave functions are obtained at the location of the jth atom:

$$\tilde{\psi}_{R,k}(x_j) = \frac{t_j e^{-ikL} + t_{j-1}}{2},$$
$$\tilde{\psi}_{L,k}(x_j) = \frac{r_{j+1}e^{ikL} + r_j}{2}, \tag{A.17}$$

Substituting these into the final equation in (2.33), leads, after a slight algebraic maneuver, into

$$t_{j-1} + r_j - \frac{\Delta_k^{(j)}c_k^{(j)}}{\mathcal{J}} = 0, \tag{A.18}$$

which reproduces the final equation in (2.36).

APPENDIX B

MASTER EQUATION OF A CHAIN OF DISSIPATIVELY COUPLED EMITTERS

We consider an system (S) of N harmonic oscillator modes interacting dissipatively through a shared one-dimensional bath (B) aligned along the x-axis. The model is similar to Fig. 2.3 in Chapter 2, with the 2LAs replaced by oscillators. We split the net Hamiltonian $\mathcal{H}$ into three contributions given by

$$\begin{aligned}
\mathcal{H}_S &= \hbar \sum_{\lambda=1}^{N} \omega_\lambda c_\lambda^\dagger c_\lambda, \\
\mathcal{H}_B &= \hbar \sum_{k} \omega_k a_k^\dagger a_k, \\
\mathcal{H}_{SB} &= i\hbar \sum_{k} \sum_{\lambda=1}^{N} g_{k\lambda} (a_k e^{ikx_\lambda} - a_k^\dagger e^{-ikx_\lambda})(c_\lambda + c_\lambda^\dagger),
\end{aligned} \tag{B.1}$$

where we assume that the mode c_λ is coupled to the waveguide at the location $x = x_\lambda$. The coupling coefficients $g_{k\lambda}$'s are assumed to be real. Here, $\mathcal{H}_{SB}$ exemplifies a two-body interaction among spatially separated modes with electromagnetic field quantized in a one-dimensional geometry.

B.1 Master equation for the Ensemble

We can adiabatically eliminate the reservoir degrees of freedom to obtain the master equation under the Markov approximation as

$$\dot{\rho}_S(t) = -\frac{i}{\hbar}[\mathcal{H}_S, \rho_S(t)] - \frac{1}{\hbar^2} \int_0^\infty \mathrm{d}\tau \, \mathrm{Tr}_B[\mathcal{H}_{SB}, [\mathcal{H}_{SB}(-\tau), \rho_S(t)\rho_B]] \tag{B.2}$$

where $\mathcal{O}(-\tau) = \exp\big[-\frac{i}{\hbar}(\mathcal{H}_S + \mathcal{H}_B)\tau\big] \mathcal{O} \exp\big[\frac{i}{\hbar}(\mathcal{H}_S + \mathcal{H}_B)\tau\big]$, and ρ_B is the initial state of the bath [56]. Decomposing the interaction Hamiltonian as $\mathcal{H}_{SB} = \sum_\alpha S_\alpha B_\alpha$, where S_α and B_α

denote the system and bath operators respectively, the above expression can be further reduced to

$$\dot{\rho}_S = -\frac{i}{\hbar}[\mathcal{H}_S, \rho_S] - \frac{1}{\hbar^2}\Big\{ \int_0^\infty \mathrm{d}\tau \sum_{\alpha,\beta} C_{\alpha\beta}(-\tau)[S_\alpha S_\beta(-\tau)\rho_S - S_B(-\tau)\rho_S S_\alpha] + \text{h.c.}\Big\} \quad \text{(B.3)}$$

with $C_{\alpha\beta}(-\tau) = \exp\{B_\alpha B_\beta(-\tau)\}$. Idealizing the bath as the electromagnetic vacuum, the reservoir signatures would encoded as $\langle a_k a_{k'}\rangle = \left\langle a_k^\dagger a_{k'}\right\rangle = 0$ and $\left\langle a_k a_{k'}^\dagger\right\rangle = \delta_{k,k'}$. We then find the constituent terms to be

$$\begin{aligned} C_{\alpha\beta}(-\tau) &= \sum_k g_{k\alpha} g_{k\beta} e^{ikx_{\alpha\beta}} e^{-i\omega_k \tau} \\ S_\alpha S_\beta(-\tau)\rho_S &= (b_\alpha + b_\alpha^\dagger)(e^{i\omega_\beta \tau} b_\beta + e^{-i\omega_\beta \tau} b_\beta^\dagger)\rho_S \\ S_\beta(-\tau)\rho_S S_\alpha &= (e^{i\omega_\beta \tau} b_\beta + e^{-i\omega_\beta \tau} b_\beta^\dagger)\rho_S (b_\alpha + b_\alpha^\dagger) \end{aligned} \quad \text{(B.4)}$$

Substituting these expressions into (B.3), we obtain $\tau-$integrals which, for the moment, can be expressed in terms of

$$\mathcal{T}_{k\mu}^{(\pm)} = \int_0^\infty \mathrm{d}\tau e^{i(\omega_\mu \pm \omega_k)\tau} = \pi\delta(\omega_\mu \pm \omega_k) + i\mathrm{P}\frac{1}{(\omega_\mu \pm \omega_k)}, \quad \text{(B.5)}$$

where $\mathrm{P}(1/x)$ denotes the Cauchy Principal Value of its argument. Since ω_k's are all positive, terms of the form $\delta(\omega_\mu + \omega_k)$ can be stamped out. In light of these simplifications, we can compactify (B.3) into the form

$$\dot{\rho}_S = -\frac{i}{\hbar}[\mathcal{H}_S, \rho_S] - \frac{1}{\hbar^2}\sum_{\alpha,\beta=1}^{N} (\mathcal{W}_{\alpha\beta} + \mathcal{W}_{\alpha\beta}^\dagger), \quad \text{(B.6)}$$

where a typical contribution would appear as

$$\mathcal{W}_{\alpha\beta} = \sum_k g_{k\alpha} g_{k\beta} e^{ik(x_\alpha - x_\beta)} \Big[\mathcal{T}_{k\beta}^{(-)}(c_\alpha^\dagger c_\beta \rho_S - c_\beta \rho_S c_\alpha^\dagger) + \mathcal{T}_{k\beta}^{(+)}(c_\alpha c_\beta^\dagger \rho_S - c_\beta^\dagger \rho_S c_\alpha)\Big]. \quad \text{(B.7)}$$

We have dropped the fast-oscillating terms that go as $c_\alpha c_\beta$ or $c_\alpha^\dagger c_\beta^\dagger$ under the purview of the rotating wave approximation. Using a linearized approximation to the reservoir frequencies $\omega_k \approx v_g|k|$, with the $+$ve and the $-$ve values of k representing right-propagating and left-propagating fields respectively, we take the continuum limit $\sum_k \rightarrow \frac{L}{2\pi}\int \mathrm{d}k$ in computing $\mathcal{W}_{\alpha\beta}$ and $\mathcal{W}_{\alpha\beta}^\dagger$. With the identification $\Lambda_\pm = \frac{1}{\pi}\mathrm{P}\int_{-\infty}^{\infty}\mathrm{d}k\frac{e^{ikx_{\alpha\beta}}}{\omega_\beta \pm v_g|k|}$ and the assumption that the coupling to the modes is independent of the field's propagation direction, the cardinal intermediate relations could be codified as

$$\begin{aligned}\int_{-\infty}^{\infty}\mathrm{d}k e^{\pm ikx_{\alpha\beta}}\delta(\omega_\beta - v_g|k|) &= \frac{2}{v_g}\cos(k_\beta x_{\alpha\beta}),\\ \Lambda_+ + \Lambda_- &= \frac{2}{v_g}\sin(k_\beta x_{\alpha\beta}),\end{aligned} \tag{B.8}$$

where $x_{\alpha\beta} = |x_\alpha - x_\beta|$ and $k_\beta = \omega_\beta/v_g$. Terms like $\mathrm{P}\int_{-\infty}^{\infty}\mathrm{d}k\frac{1}{\omega_\beta \pm v_g|k|}$ get reflected as small frequency shifts in ω_1 and ω_2, which can be neglected. Then, collecting the like terms together in (B.7) and exploiting the preceding relations in (B.8), we obtain the full master equation for the dissipative dynamics of S:

$$\dot{\rho}_S = -\frac{i}{\hbar}[\mathcal{H}_S, \rho_S] - \sum_{\alpha,\beta=1}^{N}\gamma_{\alpha\beta}(c_\alpha^\dagger c_\beta \rho_S - 2c_\beta\rho_S c_\alpha^\dagger + \rho_S c_\alpha^\dagger c_\beta) - i\sum_{\alpha\neq\beta}\Omega_{\alpha\beta}[c_\alpha^\dagger c_\beta, \rho_S]. \tag{B.9}$$

The associated coefficients are given by

$$\begin{aligned}\kappa_{\alpha\beta} &= \frac{g_\alpha^2 L}{v_g}\delta_{\alpha\beta} + \Gamma_{\alpha\beta}\cos\phi_{\alpha\beta}(1-\delta_{\alpha\beta}),\\ \Gamma_{\alpha\beta} &= (\kappa_{\alpha\alpha}\kappa_{\beta\beta})^{1/2} = \frac{g_\alpha g_\beta L}{v_g},\\ \Omega_{\alpha\beta} &= \Gamma_{\alpha\beta}\sin\phi_{\alpha\beta},\end{aligned} \tag{B.10}$$

where, in view of the proximity between the transition frequencies, it is assumed that $k_\lambda \approx k_0 = \omega_0/v_g\ \forall\lambda \in \{1, N\}$. $g_{k\alpha} \approx g_\alpha$, and $\{k_0, \omega_0\}$ is the central waveguide mode in the vicinity of which the linear dispersion holds valid. The phases $\phi_{\alpha\beta}$ are defined as $\phi_{\alpha\beta} = k_0 x_{\alpha\beta}$, and $g_{k\lambda}$'s are taken

to be k-independent. Note that the decay parameter $\kappa_{\alpha\alpha} = \dfrac{g_\alpha^2 L}{v_g}$ deduced here accounts only for the waveguide's contribution to the dynamics. When other decohering channels are considered in parallel, additional dissipative effects are tacked onto these terms.

B.2 Dissipative Dynamics of the system

Pursuant to the master equation derived, we find the dynamical equations for the various modes to be encoded as

$$\langle \dot{c}_\alpha \rangle = -i(\omega_\alpha - i\gamma_\alpha) \langle c_\alpha \rangle - \sum_{\beta \neq \alpha} \Gamma_{\alpha\beta} e^{i\phi_{\alpha\beta}} \langle c_\beta \rangle \,, \tag{B.11}$$

Switching to a frame rotating at ω_0, and defining $\omega_\alpha - \omega_0 = \Delta_\alpha$, we can recast this in matrix form as $\dot{X} = -iHX$, where $X = (\langle c_1 \rangle \;\; \langle c_2 \rangle \;\; \langle c_3 \rangle \ldots \langle c_N \rangle)^T$, and

$$H = \begin{bmatrix} \Delta_1 - i\gamma_1 & -i\Gamma_{12} e^{i\phi_{12}} & \ldots \\ \vdots & \ddots & \\ -i\Gamma_{1,N-1} e^{i\phi_{1,N-1}} & \ldots & \Delta_N - i\gamma_N \end{bmatrix}. \tag{B.12}$$

When $\phi_\beta = n\pi$, the couplings are purely dissipative. For a simple two-mode system, under the further assumption that $\Delta_1 = -\Delta_2 = \delta/2$ and $\gamma_1 = \gamma_2 = \gamma$, we obtain an anti-PT symmetric Hamiltonian.

APPENDIX C

ADIABATIC ELIMINATION OF CAVITY MODE IN THE WEAK COUPLING REGIME

In the bad-cavity limit, we can employ an adiabatic model to advance an effective two-mode description for the magnon modes, since the cavity mode relaxes rapidly into its steady state. This treatment reinforces forthwith the emergence of a dissipative interaction between the magnons, can lead to anti-PT symmetry*. In the rotating frame of the cavity mode, the mean field equations of the hybrid cavity magnon system are given by

$$\dot{X} = -i\mathcal{H}X, \tag{C.1}$$

where $\mathcal{H} = \begin{pmatrix} -i\kappa & g_1 & g_2 \\ g_1 & s - i\gamma_1 & 0 \\ g_2 & 0 & -s - i\gamma_2 \end{pmatrix}$ (see Eq. 5.28). In the adiabatic limit, we can eliminate the cavity mode by setting $\dot{a} = 0$, yielding

$$a = \frac{-i(g_1 m_1 + g_2 m_2)}{\kappa}. \tag{C.2}$$

Substituting this into Eq. (C1), we obtain a coupled system of differential equations encompassing the dynamics of the magnon modes,

$$\dot{Y} = -i\tilde{\mathcal{H}}Y, \tag{C.3}$$

*The derivation presented here appears partly in the appendix of our paper *Phys. Rev. B.* ***105****, 214418 (2022)*, published by the American Physical Society.

with Y^T =[m_1 m_2], and

$$\tilde{\mathcal{H}} = \begin{pmatrix} s - i\tilde{\gamma_1} & \dfrac{-ig_1g_2}{\kappa} \\ \dfrac{-ig_1g_2}{\kappa} & -s - i\tilde{\gamma_2} \end{pmatrix}, \tag{C.4}$$

where $\tilde{\gamma_i} = \gamma_i + \dfrac{g_i^2}{\kappa}$. The effective magnon-magnon Hamiltonian clearly features the hallmarks of dissipative coupling. To put it into perspective, the cavity, when weakly coupled to the magnons, merely acts as a common reservoir for the magnon modes in the adiabatic limit. Further, on making the usual choice $\gamma_1 = \gamma_2$, $g_1 = g_2$, it turns anti-PT symmetric.

A quick justification of C.2: From C.1, we have

$$\dot{a}(t) = -\kappa a(t) - i\sum_{j=1}^{2} g_j m_j(t). \tag{C.5}$$

Eq. C.5 can be formally integrated to obtain

$$a(\tau) = e^{-\kappa\tau}a(0) + i\sum_{j=1}^{2} g_j \int_0^\tau e^{-\kappa(\tau-t)} m_j(t)\,\mathrm{d}t\,. \tag{C.6}$$

We are interested in the cavity-dynamics after a timescale of τ such that $1/\kappa \ll \tau \ll 1/g_j, 1/\gamma_j$. Stated differently, after a timespan of τ, the cavity mode has substantially decayed away, and the first term in Eq. C.6 approximates to zero, i.e.,

$$\lim_{\tau \gg 1/\kappa} e^{-\kappa\tau}a(0) \simeq 0. \tag{C.7}$$

Since $\tau \ll 1/g_j$, coherent Rabi oscillations due to the intracavity field have barely had a chance to materialize. In addition, since $\tau \ll 1/\gamma_j$, the magnon modes have hardly experienced any dissipation within this time-frame. Consequently, in this limit, we can treat the magnon variables

as constants and take them out of the integral thus:

$$\begin{aligned}\int_0^\tau e^{-\kappa(\tau-t)} m_j(\tau)\,\mathrm{d}t &\simeq m_j(\tau)\int_0^\tau e^{-\kappa(\tau-t)}\,\mathrm{d}t \\ &\xrightarrow{\tau\gg 1/\kappa} -\frac{m_j}{\kappa}\end{aligned} \tag{C.8}$$

Substituting C.7 and C.8 into C.6, we recover C.2.